

# Important Notice

This copy may be used only for the purposes of research and private study, and any use of the copy for a purpose other than research or private study may require the authorization of the copyright owner of the work in question. Responsibility regarding questions of copyright that may arise in the use of this copy is assumed by the recipient.

UNIVERSITY OF CALGARY

Crustal Structure beneath Hudson Bay from Ambient-Noise Tomography

by

AGNIESZKA PAWLAK

A THESIS

SUBMITTED TO THE FACULTY OF GRADUATE STUDIES  
IN PARTIAL FULFILMENT OF THE REQUIREMENTS FOR THE  
DEGREE OF DOCTOR OF PHILOSOPHY

DEPARTMENT OF GEOSCIENCE

CALGARY, ALBERTA

APRIL, 2012

© AGNIESZKA PAWLAK 2012

UNIVERSITY OF CALGARY  
FACULTY OF GRADUATE STUDIES

The undersigned certify that they have read, and recommend to the Faculty of Graduate Studies for acceptance, a thesis entitled "Crustal Structure Beneath Hudson Bay from Ambient-Noise Tomography" submitted by AGNIESZKA PAWLAK in partial fulfilment of the requirements of the degree of DOCTOR OF PHILOSOPHY.

---

*Supervisor, DAVID EATON, DEPARTMENT OF  
GEOSCIENCE*

---

*ADAM PIDLISECKY, DEPARTMENT OF GEOSCIENCE*

---

*KRIS VASUDEVAN, DEPARTMENT OF GEOSCIENCE*

---

*MARIO COSTA SOUSA, DEPARTMENT OF COMPUTER  
SCIENCE*

---

*External Examiner, ANDREW FREDERIKSEN,  
UNIVERSITY OF MANITOBA*

---

*Date*

## Abstract

Hudson Bay is a shallow inland sea located in north-central Canada. The underlying lithosphere preserves a complex deformational history that dates back to the Archean. The Hudson Bay Lithospheric Experiment, HuBLE, is a collaborative initiative aimed at understanding the lithospheric evolution beneath the Bay.

The recent emergence of a methodology called ambient-noise tomography provides a tool to image the crust and upper mantle beneath the Bay with higher resolution than previously possible. Using ambient-noise generated by the Earth as a source, this technique requires continuous recordings of ground motion. The ambient-noise method is based on the cross-correlations of daily noise signals between station pairs to estimate empirical Green's Functions.

This thesis is made up of three separate studies. The first is an isotropic application of the ambient-noise tomography method to image crustal structure beneath Hudson Bay. Results show crustal thinning beneath the Bay, allowing us to reject a hypothesis for eclogitization and crustal thickening, with support instead for an extensional hypothesis for the formation of the Hudson Bay basin.

The next study focuses on anisotropic variations of velocity within the subsurface. Inversion results show a distinct outline of geologic boundaries in the upper to mid-crust that does not carry through into the lower crust. A significant change in anisotropic fabric is evident across the Trans-Hudson orogen (THO) suture zone, which allows us to establish that tectonic fabrics formed prior to collision.

The third study employs joint inversion of ambient-noise data and teleseismic surface wave data for increasing resolution of the crust and upper mantle. Results show that the THO suture zone dips to the southeast within the crust and becomes vertical in the upper mantle. This feature is interpreted as a zone of weakness that extends through the lithosphere, providing a locus for initiation of localized lithospheric stretching.

## Preface

This thesis investigates the crustal and upper mantle structure beneath Hudson Bay, Canada. The intention is to increase resolution and understand the lithospheric evolution of this region.

This thesis includes one previously published manuscript. Chapter two is a reprint of:

Pawlak, A.P., D.W. Eaton, I.D. Bastow, J.M. Kendall, G. Helffrich, J. Wookey, and D. Snyder (2011), Crustal structure beneath Hudson Bay from ambient-noise tomography: Implications for basin formation, *Geophys. J. Int.*, 184, 65-82, doi:10.1111/j.1365-246X.2010.04828.x

Permission from the publisher and coauthors was obtained prior to including this publication.

Chapter three has been submitted for publication and is currently in review.

## Acknowledgements

First and foremost, I'd like to thank Dr. David Eaton for his supervision and support. Without all his guidance, patience, support and encouragement this thesis would not have been possible.

Next I would like to thank my supervisory committee, Dr. Adam Pidlisecky and Dr. Kris Vasudevan, for all their encouragement and valuable comments and discussions. I would also like to thank all my co-authors for all their contribution and comments that have improved the quality of this work: Ian Bastow, Fiona Darbyshire, George Helfrich, Mike Kendell, Sergei Lebedev, David Snyder, and James Wookey. Also, Geophysical Journal International and co-authors for permission to reprint the published article in this thesis.

We are grateful to Dr. Honn Kao, from the Pacific Geoscience Center in Sydney, B.C., for providing us with initial data and assistance with data processing. Thank you to all the staff and students in the CREWES project at the University of Calgary for all their support. Thank you to C-NGO and the First Nation communities around Hudson Bay for allowing seismometer deployments.

I'd like to thank my friends and colleagues for their support and friendship, especially Catrina Alexandrakis, Maria Gallant, Andy St-Onge and Jackie Randall.

Finally, thank you to my family for all their support and patience. To my parents, Bogdan and Elizabeth. Thank you to my sister Alicja and Niall. Thank you to Brendan and the entire Smith family.

## Table of Contents

|  |     |
|--|-----|
| Approval Page.....   | ii  |
| Abstract.....  | iii |
| Preface.....   | v   |
| Acknowledgements.....  | vi  |
| Table of Contents.....   | vii |
| List of Tables.....  | x   |
| List of Figures and Illustrations.....   | xi  |
| List of Symbols, Abbreviations and Nomenclature.....   | xiv |
| <br>   |     |
| Chapter One: INTRODUCTION AND LITERATURE REVIEW.....   | 1   |
| 1.1 Tectonic Setting.....  | 3   |
| 1.2 Glacial History and Isostatic Rebound.....   | 6   |
| 1.3 Hudson Bay Lithospheric Experiment.....  | 8   |
| 1.4 The Origin of Ambient-Noise Sources.....   | 11  |
| 1.5 Ambient-Noise Method.....  | 12  |
| 1.6 Ambient-Noise Data.....  | 15  |
| 1.7 Rayleigh Waves and Dispersion.....   | 20  |
| 1.8 Surface Wave Tomography.....   | 21  |
| 1.9 Previous Geophysical Constraints.....  | 25  |
| 1.10 Thesis Goals and Organization.....  | 26  |
| 1.11 Published Work and Author Contributions.....  | 27  |
| <br>   |     |
| Chapter Two: CRUSTAL STRUCTURE BENEATH HUDSON BAY FROM AMBIENT-<br>NOISE TOMOGRAPHY: IMPLICATIONS FOR BASIN FORMATION..... | 29  |
| Summary.....   | 29  |
| 2.1 Introduction.....  | 30  |
| 2.2 Tectonic Setting.....  | 34  |
| 2.3 Data and Initial Processing.....   | 38  |
| 2.3.1 Directionality and Seasonality.....  | 41  |
| 2.3.2 Dispersion Analysis.....   | 46  |
| 2.3.3 1D Inversion.....  | 49  |
| 2.4 Tomographic Imaging.....   | 52  |
| 2.5 Results.....   | 56  |
| 2.6 Discussion.....  | 59  |
| 2.6.1 Directionality and seasonality.....  | 59  |
| 2.6.2 Velocity distributions.....  | 62  |
| 2.6.3 Crustal thinning.....  | 64  |
| 2.6.4 Depth Inversion.....   | 66  |
| 2.7 Conclusions.....   | 73  |

|   |     |
|---|-----|
| Chapter Three: CRUSTAL ANISOTROPY BENEATH HUDSON BAY FROM<br>AMBIENT-NOISE TOMOGRAPHY: EVIDENCE FOR POST-OROGENIC<br>LOWER-CRUSTAL FLOW?..... | 76  |
| Summary .....   | 76  |
| 3.1 Introduction.....   | 77  |
| 3.2 Tectonic Setting .....  | 79  |
| 3.3 Data And Processing Methods.....  | 83  |
| 3.4 Inversion .....   | 86  |
| 3.5 Resolution Testing .....  | 95  |
| 3.6 Results.....  | 100 |
| 3.7 Discussion.....   | 101 |
| 3.7.1 Crustal Stresses.....   | 103 |
| 3.7.2 Magnetic Data .....   | 104 |
| 3.7.3 Contrasting crustal profiles across suture.....   | 108 |
| 3.7.4 Tectonic overprint in the lower crust.....  | 110 |
| 3.8 Conclusions.....  | 112 |
| Chapter Four: JOINT INVERSION: AMBIENT-NOISE AND SURFACE WAVES .....  | 114 |
| 4.1 Introduction.....   | 114 |
| 4.2 Tectonic Setting .....  | 116 |
| 4.3 Data.....   | 119 |
| 4.3.1 HuBLE Network.....  | 119 |
| 4.3.2 Ambient-Noise .....   | 121 |
| 4.3.3 Surface Waves .....   | 122 |
| 4.4 Two-Stage Inversion Process.....  | 123 |
| 4.4.1 Tomographic Surface Wave Inversion .....  | 124 |
| 4.4.2 Monte-Carlo Inversion .....   | 125 |
| 4.5 Sensitivity Kernels .....   | 128 |
| 4.5.1 Earth Models .....  | 128 |
| 4.5.2 Partial Derivatives .....   | 131 |
| 4.6 Ambient-Noise Phase Velocity.....   | 135 |
| 4.7 Compatibility of the datasets .....   | 138 |
| 4.8 1D models .....   | 142 |
| 4.8.1 Starting model parameterizations .....  | 142 |
| 4.8.2 1D depth profiles .....   | 145 |
| 4.9 Results.....  | 149 |
| 4.10 Discussion.....  | 152 |
| 4.11 Conclusions.....   | 156 |
| Chapter Five: CONCLUSIONS.....  | 159 |
| 5.1 Summary of Thesis Work .....  | 160 |
| 5.1.1 Isotropic crustal structure and ambient noise sources .....   | 160 |
| 5.1.2 Anisotropic structure .....   | 162 |
| 5.1.3 Joint Inversion of Ambient Noise and Surface Waves.....   | 163 |
| 5.2 General Contributions.....  | 164 |
| 5.3 Future Work .....   | 165 |

|  |     |
|--|-----|
| REFERENCES.....                                      | 168 |
| Appendix A: CHOICE OF REGULARIZATION PARAMETERS..... | 191 |
| Appendix B: BOOTSTRAP ERROR ANALYSIS.....            | 198 |
| Appendix C: SAMPLE CODE .....                        | 204 |

## List of Tables

|   |     |
|---|-----|
| Table 4.1 – Crustal parameterization for SM1 with fixed layer depths. SM2 has the same values, however layer thickness is allowed to vary $\pm 3$ km..... | 144 |
| Table 4.2 – Crustal parameterization for SM3 with fixed layer depths.....   | 144 |
| Table A1 Parameter values. ....   | 197 |

## List of Figures and Illustrations

|   |    |
|---|----|
| Figure 1.1 Geological map of Laurentia. ....  | 2  |
| Figure 1.2 Map of Hudson Bay and location of seismograph stations. ....                 | 4  |
| Figure 1.3 Laurentide Ice-Sheet cover at its maximum to today. ....                     | 7  |
| Figure 1.4 Photo of station INUQ. ....  | 9  |
| Figure 1.5 Photo of seismometer at station INUQ. ....                                   | 10 |
| Figure 1.6 Inter-station cross-correlations sorted by distance. ....                    | 13 |
| Figure 1.7 Example of ambient-noise data ....   | 17 |
| Figure 1.8 Example of frequency and period spectra. ....                                | 18 |
| Figure 1.9 Example of normalized frequency and period spectra. ....                     | 19 |
| Figure 1.10 Illustration of Love wave and Rayleigh wave propagation. ....               | 23 |
| Figure 1.11 Example of group velocity dispersion measurement. ....                      | 24 |
| Figure 2.1 Map of Hudson Bay seismograph stations. ....                                 | 32 |
| Figure 2.2 Schematic of proposed hypotheses. ....                                       | 35 |
| Figure 2.3 Generalized geology map. ....  | 37 |
| Figure 2.4 Cross-correlations. ....   | 39 |
| Figure 2.5 Directionality of noise sources. ....  | 42 |
| Figure 2.6 Seasonality of noise sources. ....   | 46 |
| Figure 2.7 Example of Dispersion Analysis. ....   | 48 |
| Figure 2.8 Conventional versus SNR selection method. ....                               | 51 |
| Figure 2.9 Checkerboard model. ....   | 53 |
| Figure 2.10 Checkerboard reconstruction results. ....                                   | 56 |
| Figure 2.11 Two-sided empirical Green's Function (EGF) tomographic reconstruction. .... | 58 |
| Figure 2.12 One-sided empirical Green's Function EGF tomographic reconstruction. ...    | 61 |

|  |     |
|--|-----|
| Figure 2.13 Pseudo-sections. ....  | 64  |
| Figure 2.14 Velocity distribution.....                                   | 67  |
| Figure 2.15 Comparison with lithospheric stretching factor diagram. .... | 68  |
| Figure 2.16 Crustal thinning model. ....                                 | 70  |
| Figure 2.17 1D depth inversions. ....                                    | 72  |
| Figure 2.18 1D depth inversion showing crustal thinning. ....            | 74  |
| Figure 3.1 Seismograph station map and generalized geology map.....      | 80  |
| Figure 3.2 Example of cross-correlation and noise asymmetry.....         | 82  |
| Figure 3.3 Example time-frequency plot and dispersion analysis. ....     | 84  |
| Figure 3.4 Path density and grid knot maps.....                          | 88  |
| Figure 3.5 Schematic of geologic scenarios. ....                         | 91  |
| Figure 3.6 Data fit to $2\Psi$ and $4\Psi$ variations. ....              | 94  |
| Figure 3.7 Isotropic checkerboard model. ....                            | 96  |
| Figure 3.8 Isotropic checkerboard reconstruction. ....                   | 98  |
| Figure 3.10 Inversion results.....                                       | 103 |
| Figure 3.11 Regional total-field magnetic anomaly data.....              | 107 |
| Figure 3.12 Anisotropic dispersion curves. ....                          | 109 |
| Figure 4.1 Generalized geology map.....                                  | 118 |
| Figure 4.2 Seismograph station map.....                                  | 120 |
| Figure 4.3 Grid node map. ....   | 127 |
| Figure 4.4 Earth models.....   | 130 |
| Figure 4.5 Sensitivity kernel for ak135.....                             | 133 |
| Figure 4.6 Sensitivity kernel for CANSD.....                             | 134 |
| Figure 4.7 Ambient-noise phase velocity .....                            | 137 |
| Figure 4.8 Comparison of group and phase dispersion curves. ....         | 139 |

|  |     |
|--|-----|
| Figure 4.9. Path density maps. ....  | 141 |
| Figure 4.10 1D depth profiles. ....  | 147 |
| Figure 4.11 1D depth profiles for reduced dataset.....                         | 149 |
| Figure 4.12 Depth slices. ....   | 152 |
| Figure 4.13. Regional average curve. ....                                      | 154 |
| Figure 4.14. Cross-sections.....   | 155 |
| Figure 4.15. Schematic cross section showing inferred THO suture geometry..... | 158 |
| Figure A1 Anisotropic model for parameter testing. ....                        | 193 |
| Figure A2 Trade-off curves for synthetic data.....                             | 195 |
| Figure A3 Trade-off curves for real data. ....                                 | 196 |
| Figure B1 Knot point and suture location map.....                              | 200 |
| Figure B2 HUB region amplitude and azimuth histograms.....                     | 201 |
| Figure B3 SUP region amplitude and azimuth histograms.....                     | 202 |
| Figure B4 Error distribution map.....  | 203 |

## List of Symbols, Abbreviations and Nomenclature

| <u>Symbol</u> | <u>Definition</u>                                       |
|---------------|---|
| ak135         | Global velocity model (Kennett et al., 1995)            |
|               | Canadian Shield velocity model (Brune and Dorman, 1963) |
| CANSO         |   |
| CNSN          | Canadian National Seismograph Network                   |
| EGF           | Empirical Green's Function                              |
| HBB           | Hudson Bay basin  |
| HuBLE         | Hudson Bay Lithospheric Experiment                      |
| LAB           | Lithosphere-asthenosphere boundary                      |
| LGM           | Last Glacial Maximum                                    |
| LPO           | Lattice preferred orientation                           |
| NCF           | Noise correlation function                              |
| NERC          | Natural Environmental Research Council                  |
| SNR           | Signal-to-noise ratio                                   |
| SH wave       | Horizontally polarized shear wave                       |
| SV wave       | Vertically polarized shear wave                         |
| THO           | Trans-Hudson orogen                                     |
| $V_p$         | P-wave velocity   |
| $V_s$         | S-wave velocity   |

## Chapter One: **INTRODUCTION AND LITERATURE REVIEW**

Hudson Bay is an enigmatic region within the North American continent. Lying near the centre of the North American plate, it is situated at the core of the continent and has survived a complex tectonic evolution. Although the Bay is presently submerged, it sits atop continental crust that is inaccessible to geologists. The lithosphere beneath the Bay is ~200 km thick (Eaton and Darbyshire, 2010) and straddles the suture between two Archean cratons (regions that have not deformed on a billion-year timescale), which collided and created the Trans-Hudson orogeny (now deeply eroded). This region has been difficult to study in the past because of its submerged state, however, the recent emergence of a new technique, called ambient-noise tomography, provides a method to image the crust and upper mantle without the need for instrumentation in the centre of the Bay. This thesis focuses on elucidating the tectonic evolution and crustal structure concealed by Hudson Bay using ambient-noise tomography.

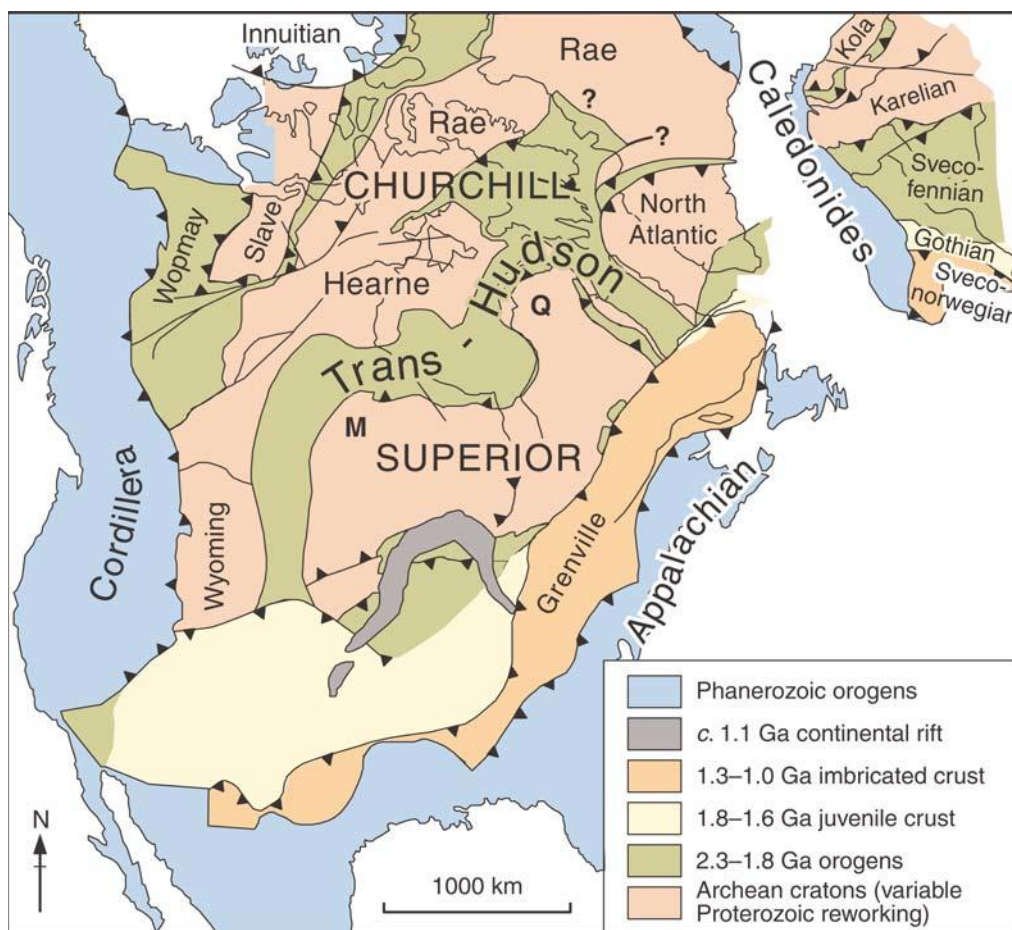


**Figure 1.1 Geological map of Laurentia.**

Geological map of Laurentia (St. Onge et al., 2012, after Hoffman, 1988). Abbreviations:

M, Manitoba promontory; Q, Quebec promontory.

## 1.1 Tectonic Setting

Laurentia is one of the oldest and largest cratons, comprising the majority of the North American continent. Also referred to as the North American craton, it was created by assembly of older blocks via a network of 2.3 – 1.8 Ga (billion year) orogens (Figure 1.1). Some of the orogens are remnants of collision zones between Archean microcontinents, whereas others contain accreted island arcs and oceanic deposits (Hoffman, 1988). Hudson Bay is a large, shallow epeiric sea located near the centre of the North American continent (Figure 1.2). Hidden beneath the surface is a complicated crust preserving tectonic processes that have not been well understood to this day. With a preserved record of the collisional assembly of Laurentia and the subsequent formation of the Hudson Bay basin, many details of the lithospheric evolution remain unclear.

Covering almost the entire extent of the Bay lies a large intracratonic basin (a sedimentary basin forming on a craton) called the Hudson Bay basin. Approximately 2 km in thickness, this is the shallowest but most extensive of a set of generally similar intracratonic basins in North America (Michigan, Williston, Illinois). Subsidence in the Hudson Bay basin initiated at roughly the same time as the Michigan basin (Hamdani et al., 1991). Both basins have a second non-synchronous phase of subsidence, although reduced subsidence occurred within the Hudson Bay basin. It has been suggested that this second phase of subsidence in the Michigan basin was due to the flexural load introduced by eclogitization (Hamdani et al., 1991), a process where lower-crustal materials undergo a phase transformation from basaltic composition to dense eclogite. However, the evolutionary formation of the Hudson Bay basin is currently poorly understood.

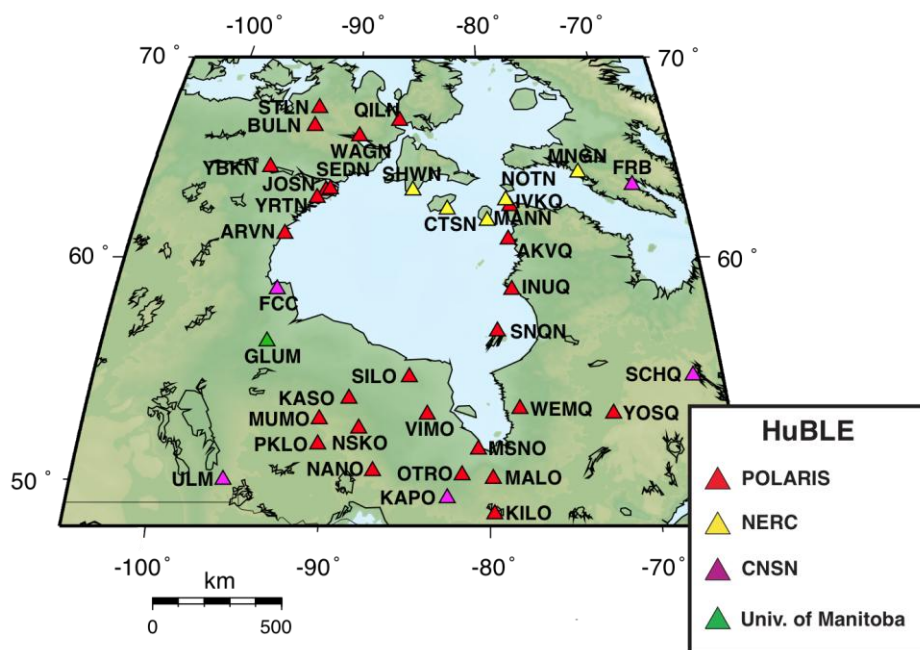


**Figure 1.2 Map of Hudson Bay and location of seismograph stations.**

Map of Hudson Bay showing seismograph stations used in this study.

Covered by the Hudson Bay basin and similar in scale to the modern-day Himalaya-Karakoram orogeny (the process by which mountains are built on continents) (St-Onge et al., 2016), the Trans-Hudson orogen (THO) (Figure 1.1) formed as a result of the collision between the Superior Province, from the south and east, and Churchill Plates, (Rae and Hearne domains) from the north and west. The THO welds together the two Archean cratons (the oldest and most stable part of the continental lithosphere) in the nucleus of the North American continent. Now deeply eroded, the THO cross-cuts diagonally through the centre of the Bay, in a SW-NE direction. Where exposed around Hudson Bay, the THO contains both juvenile supracrustal domains and blocks of pre 1.91 Ga crust. Paleomagnetic evidence suggests that the two Archean cratons were once separated by a Pacific-scale ocean called the Manikewan Ocean (Symons and Harris, 2005), which is now manifested across Hudson Bay as a suture.

The lithosphere is the outermost shell of the Earth comprised of the crust and upper mantle. The lithosphere is a hard and rigid top layer, underlain by the asthenosphere, the weaker a hotter part of the mantle. Divided by tectonic plates and the lithosphere-asthenosphere boundary (LAB), the lithosphere may be considered as the largest class of plate boundary (Eaton et al., 2010). Cratons generally are found in the interior of tectonic plates, and have withstood the merging and rifting of continents. They have a thick crust and deep lithospheric root that extends in the Earth's upper mantle, for several hundred km (Eaton et al., 2009). Since cratons are made up of some of the oldest material, they preserve the evolutionary history of a region. The lithospheric mantle beneath Hudson Bay has a high shear-wave velocity, relative to typical shear-wave velocity of the lithosphere,

and is estimated to be at least 200 km in thickness (Darbyshire and Eaton, 2010). Understanding characteristic of the lithospheric mantle can help with the understanding of the crustal structure as well.

## **1.2 Glacial History and Isostatic Rebound**

At the Last Glacial Maximum (LGM) (18 ka BP) (Clark et al., 2009), the Laurentide Ice Sheet was at its maximum, covering the centre of the Canadian Shield across the Interior Plains. The Laurentide Ice Sheet was the nucleus for the North American Ice Sheet Complex, a conglomerate of smaller ice sheets covering North America (Figure 1.3). Ice sheet thickness reached a maximum up to 3.3 – 4.3 km in the Yellowknife region, and approximately 3 – 3.5 km thick in the Hudson Bay region at the LGM (Tarasov and Peltier, 2004). The main phase of deglaciation in North America occurred between 17 – 8 ka BP (Dyke, 2003). The load of the ice-sheet created a depression on the surface, which is currently experiencing glacial isostatic adjustment (Wu, 1996), at a rate between 5 – 14 mm of rebound per year in the Hudson Bay region (Tarasov and Peltier, 2004).



**Figure 1.3 Laurentide Ice-Sheet cover at its maximum to today.**

The Laurentide Ice-Sheet coverage at its maximum in the Last Glacial maximum (on the left), approximate ice coverage at 10 ka BP (in the centre) and ice coverage today (on the right). (<http://www.thecanadianencyclopedia.com/articles/glaciation> accessed on March 28, 2012).

### **1.3 Hudson Bay Lithospheric Experiment**

This thesis is part of a joint project known as HuBLE, the Hudson Bay Lithospheric Experiment, a collaboration between University of Calgary, University of Manitoba, Université du Québec à Montréal, and University of Western Ontario in Canada and University of Bristol in the UK. In conjunction with the Geological Survey of Canada, broadband seismological stations have been deployed around the periphery of Hudson Bay. The goal of this project is to acquire a better understanding the subsurface beneath Hudson Bay, specifically the formation of the underlying basin and the nature of the tectonic processes that shaped this region. This study provides new insights toward both of these goals using a relatively new methodology for imaging the crust and upper mantle called ambient-noise tomography, which uses noise generated by the Earth as a source.

Other studies being conducted as part of the HuBLE project and using HuBLE data include receiver functions to study various features and depth ranges of crustal structure, including determining crustal thickness (Thompson et al., 2010) and mantle transition zone thickness (Thompson et al., 2010). Also, a SKS-splitting investigation of upper-mantle anisotropy (Bastow et al., 2011) and surface-wave studies of the lithospheric keel (Darbyshire and Eaton, 2010) have been undertaken.



**Figure 1.4 Photo of station INUQ.**

Photo of station INUQ (Figure 1.2) in Inukjuak, Quebec, looking west into Hudson Bay. The silver vault encloses the seismometer. The black case encloses a magnetotelluric station. In the background, a GPS station can be seen.



**Figure 1.5 Photo of seismometer at station INUQ.**

Photo of the inside of the vault enclosing the seismometer at station INUQ (Figure 1.2), in Inukjuak, Quebec.

#### **1.4 The Origin of Ambient-Noise Sources**

Ambient-noise generated by the Earth has interesting and coherent properties and noise studies have been emerging increasingly in recent years. Knowledge of the origin of noise is required to optimize seismic imaging and can also be used for seismic imaging itself. Ambient seismic noise consists mainly of surface waves, as its sources are generated near the surface (Stehly et al., 2006). The main cause of the noise is believed to be loading by pressure perturbations in the atmosphere and ocean; however, the mechanisms generating seismic noise are different depending on period bands. There are two main period bands, the primary (10 – 20 s) and secondary (5 – 10 s) microseismic bands. These two bands are thought to be generated by ocean waves interacting with the coast. The origins of the primary microseisms are poorly understood but have a similar period to the main ocean swell, whereas the secondary is of higher amplitude and is generated by the nonlinear interaction between the direct and reflected swell waves that result in half periods of pressure variations (Longuet-Higgins, 1950). The primary microseism has a seasonal variability similar to long period noise (20-40 s) (Stehly et al., 2006), which is closely correlated to ocean wave height and wave activity in deep water. The long periods are known to be generated by infragravity ocean waves, and this is likely also the mechanism in the primary microseism (Stehly et al., 2006).

## 1.5 Ambient-Noise Method

Active sources such as explosions are expensive and earthquake sources are infrequent and inhomogeneously distributed. Thus, ambient noise tomography can be a more reliable and economical source for seismology as well as a complement to other studies. Commonly Rayleigh and Love waves are used, but P-waves can also be extracted from the correlation function of seismic noise for closely spaced receivers ( $<11\text{km}$ ) (Roux et al., 2005).

Using cross-correlation functions with ambient seismic noise to extract Green's functions is a concept that emerged in the early 2000's. Shapiro and Campillo (2004) and Sabra et al. (2005) first applied the method in southern California. The idea of correlating diffuse field to extract Green's functions, however, has been used widely in physics much earlier in areas such as helioseismology (Duvall et al., 1993; Gilles et al., 1997), acoustics (Weaver and Lobkis, 2001), and oceanography (Roux and Kuperman, 2003). In seismology the method was first used with coda waves. Coda waves are the late part of the seismic signal and result from the scattering from small-scale heterogeneities in the lithosphere (Campillo and Paul, 2003; Snieder, 2004). The multiple scattering of coda waves fits well with the assumption that the field must be uncorrelated and diffuse for this methodology to work (Lobkis and Weaver, 2001). The method is highly applicable to ambient noise because the sources randomize when averaged and moreover, are further scattered from heterogeneities in the Earth (Hennino et al, 2001; Shapiro et al., 2005).

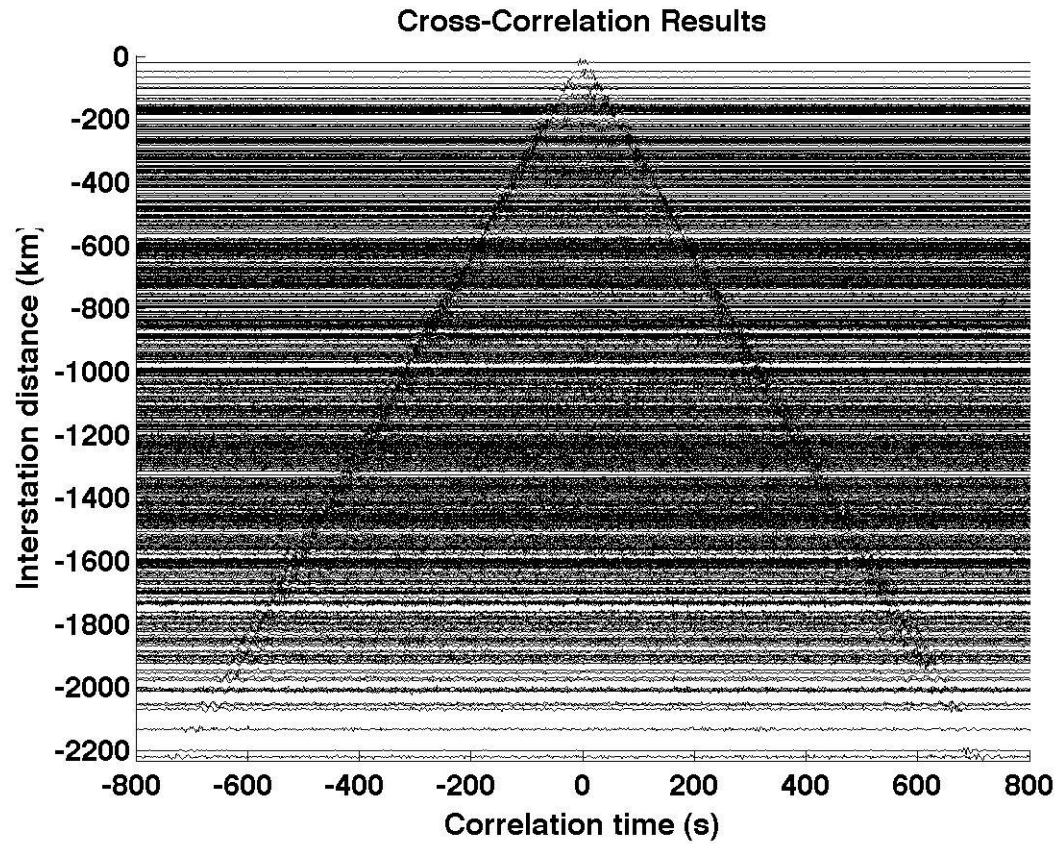


**Figure 1.6 Inter-station cross-correlations sorted by distance.**

Plot of two-sided NCFs for all station pairs against inter-station distance. Signals are apparent out to 2200 km.

Cross-correlations between two stations where coherent noise passes through both receivers emerges an estimate for the Green's Function. The Green's Function is an impulse response of a system, where one receiver acts as a source. The noise correlation function (NCF) is the passive analog to the shot gather made with active sources (a display of seismic traces for a common shot point) and consists of two parts, causal and acausal. An example of NCF from this study is shown in Figure 1.6. If noise sources are distributed evenly with azimuth then the NCF will be symmetric, however in some cases there are dominant noise sources and the correlations will be asymmetric. The Green's Function or Empirical Green's Function (EGF) commonly comes from averaging the two-sided NCF or, if the NCF is one sided, by picking a single side based on various criteria. In this study the largest signal-to-noise ratio is used to construct the EGF, as discussed in Chapter Two.

Ambient-noise studies have been evolving quickly. Early studies focused on local and regional scale observations in the western US as well as analysis of microseisms and the origin of ambient seismic noise. This quickly progressed to large-scale problems with coverage now extending to most of the globe. For example, studies have now been done from the western US progressing to the eastern US with the Transportable array; Australia (Saygin and Kennett, 2010), the Iberian Peninsula (Villasenor et al., 2007), Europe (Yang et al., 2007), New Zealand (Lin et al., 2007), China (Zheng et al., 2008), Africa (Yang et al., 2008) and Tibet (Yao et al., 2006). As the regional scope of ambient-noise studies progresses, so does the science, starting with Rayleigh waves to Love waves, isotropic velocities to radial and azimuthal anisotropy, joint inversions with

earthquake data allowing for crust and mantle imaging, and epicentral locations of seismic events. This is just the beginning of a very interesting and important new branch of seismology.

### **1.6 Ambient-Noise Data**

In this study we use 37 broadband seismograph station located around Hudson Bay (Figure 1.2). These stations are all enclosed in a vault system to protect them from the elements and other disturbances (e.g. Figure 1.4). The systems have a digital recording system and the data is transferred via the internet; however some stations have a flash disk where data is stored and needs to be retrieved periodically. Seismometers used are mainly Guralp CMG-3T (Figure 1.5) or Nanometrics Trillium 240 systems. Both systems record three-components of ground-motion.

The data used in this study comprises continuous recordings of the vertical component ground motion acquired during a 21-month period from September 2006 to May 2008 from 37 broadband seismic stations located around the periphery of Hudson Bay (Figure 1.2). The data needs to be pre-processed prior to cross-correlation in order to isolate the ambient-noise signal. Very briefly, in this process the data are clipped to daily recordings and resampled to 1 sample per second. Next the mean, trend and instrument response are removed. An example of raw data from the vertical component from station FRB (Figure 1.2) at this stage is shown in Figure 1.7 and an example of the frequency spectrum is shown in Figure 1.8. It can be seen that there is strong frequency peak between 0.125 –

0.3 Hz (or 3.33 – 8 s) and fairly consistent flat frequencies between 0.04 – 0.125 Hz (or 8 – 25 s). Looking at the spectrum with respect to period makes it easier to examine the lowest frequencies. In Figure 1.8, we see that the longer periods ( $> 40$  s, or  $< 0.025$  Hz) have a ‘semi-sinusoidal tail’, revealing some sort of coherent signal, possibly longer period ( $> 40$  s) noise known as ‘Earth hum’ (Stehly et al., 2006).

The data example considered here (Figure 1.8 and 1.8) has a clear peak in the secondary microseismic band (3 – 8 s), but lacks strong signals in the primary microseismic band. Studies of ambient Earth noise have been done increasingly since the study of Petersen (1993). Power spectral density models are calculated from broadband seismic stations around the globe taking a large number of one-hour wave-forms from years of data (McNamara and Burland, 2003). Results show dominant noise sources from the instrumentation (usually well below the noise level) and from Earth vibrations. The so-called new low noise model corresponds well with our frequency spectrum (Figure 1.9), with a peak amplitude in the 1 – 10 s band (Petersen, 1993).

At this point the data may still contain earthquake signals, instrument irregularities or other undesirable signals. To remove these we apply a temporal normalization, after which the spectrum is whitened to get the broadest range of frequencies. Frequency spectrum post-temporal normalization and pre-spectral whitening is shown in Figure 1.9. After the signal is normalized, the frequency spectrum (Figure 1.9) is more consistent aside from the peak between 0.125 – 0.3 Hz (or 3.33 – 8 s). This peak is discussed further below. At longer periods ( $> 40$  s, or  $< 0.025$  Hz) the ‘semi-sinusoidal tail’ has now been removed.

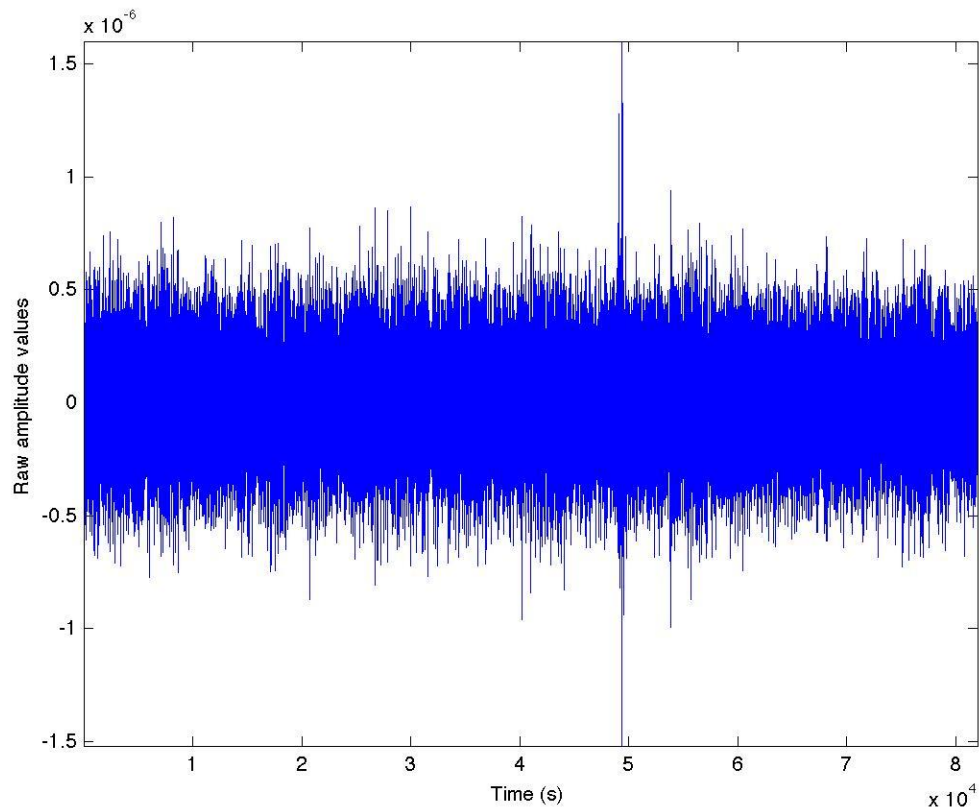


**Figure 1.7 Example of ambient-noise data**

Example of raw noise signal from station FRB recorded on March 24, 2008. The vertical axis is the raw amplitude values which vary with station, due to differences in amplifier settings.

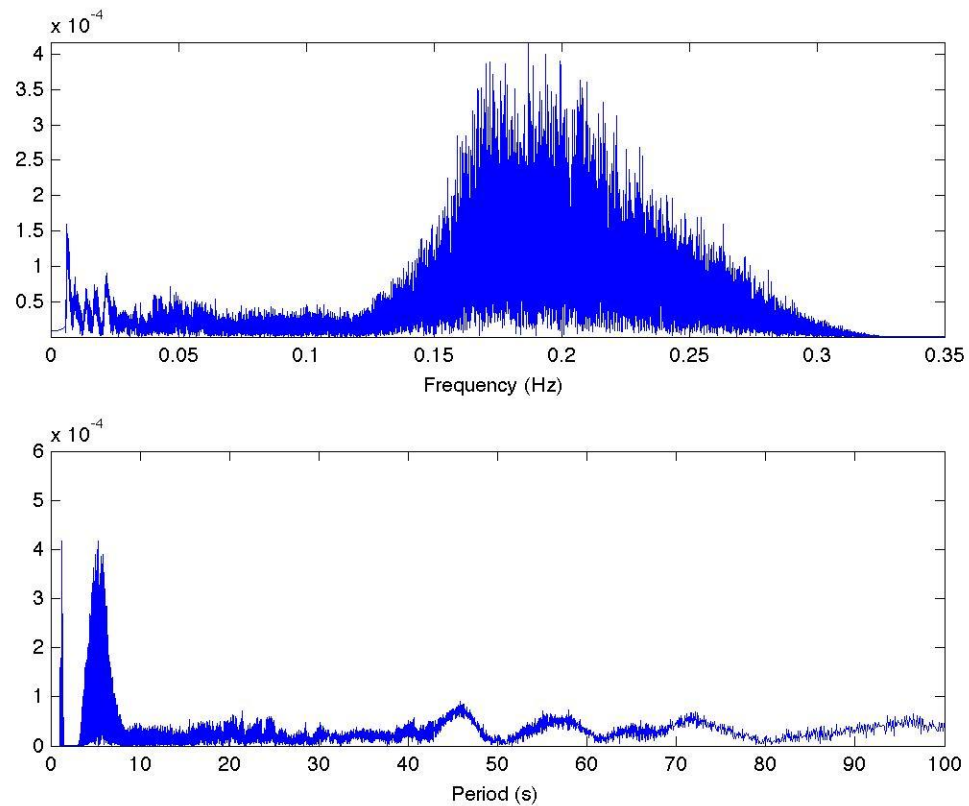


**Figure 1.8 Example of frequency and period spectra.**

Example of Fourier amplitude spectrum for the noise sample shown in Figure 1.6. Top panel shows the frequency spectrum, lower panel shows the same spectrum versus period, which shows some of the key noise features more clearly. The vertical axis is the raw amplitude values, which varies by station, due to differences in amplifier settings.

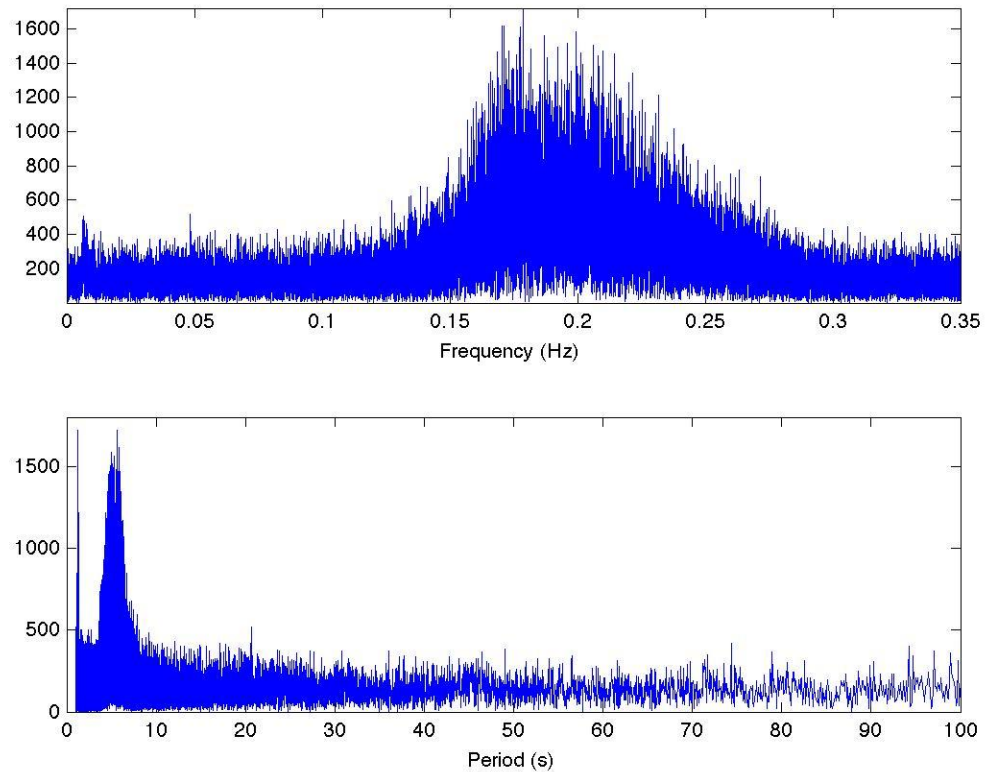


**Figure 1.9 Example of normalized frequency and period spectra.**

Example of Fourier amplitude spectrum for the noise sample shown in Figure 1.6 with temporal normalization applied. Top panel shows frequency spectrum, lower panel shows the same spectrum versus period, which shows some of the key noise features more clearly. The vertical axis is the normalized amplitude values, after instrument response correction.

## 1.7 Rayleigh Waves and Dispersion

This study is mainly focused on Rayleigh wave group-velocities and their dispersive properties. Group velocity is defined as the speed at which a wave packet travels, as compared with phase velocity, which is the speed at which an individual phase of a single frequency component within the packet travels. Noise sources are dominantly composed of surface waves, which are waves that travel along the surface much like waves on a body of water. They are called surface waves because their amplitude diminishes with depth and they occur at a free-surface, where the boundary conditions are traction-free (Stein and Wysession, 2003). In standard active-source surveys, surface waves are the dominant component of the ground roll, a coherent noise that is generally removed. There are two types of surface waves, Love waves and Rayleigh waves. Love waves, usually arrive first and are the result of SH waves (horizontally polarized shear-waves) trapped near the surface (Figure 1.10). Rayleigh waves typically arrive after Love waves and are the result of a combination of P (primary waves) and SV (vertically polarized shear-waves) giving retrograde motion (Figure 1.10). The shaking felt during an earthquake is dominated by surface waves (Stein and Wysession, 2003).

For a depth-dependent velocity structure, both types of surface waves are dispersive, which implies that the different frequencies (or periods) travel at different velocities. Usually lower frequencies (or higher periods) travel at faster velocities, referred to as normal dispersion. Anomalous dispersion can also occur, however, where lower frequencies travel slower than higher frequencies. An example of dispersive Rayleigh-wave group-velocities from ambient-noise data is shown in Figure 1.11. The shorter

periods (15 – 35 s) propagate slower than the longer periods (45 – 65 s). The propagation velocity of long periods reflects conditions at greater depths than shorter periods. It is important to notice the diminishing amplitude of the Rayleigh waves with depth (i.e. longer period).

### 1.8 Surface Wave Tomography

Tomography refers to an imaging methodology used to reconstruct the interior of a medium. The method was first developed in the field of medical X-ray imaging in the 1930s (Stein and Wysession, 2003). In seismology, the method is used to reconstruct the Earth's velocity structure from seismic data. There are two main types of seismic tomography, known as traveltimes tomography and waveform tomography. The more common method, and the method used herein this thesis, is traveltimes tomography. This method of tomography has lower resolution than waveform tomography; however it is more robust, easier to implement and computationally cheaper (Stein and Wysession, 2003). The tomography problem is defined by a radon transform, an integral transform consisting of integral functions,  $f(x)$ , over straight lines,  $p$ ,

$$\int_p f(x) dx . \quad (1.1)$$

Generally the tomography problem is parameterized over the region of interest, commonly using a grid of nodes or blocks. Surface-wave tomography methods are well

developed and algorithms differ from one another based on the parameterization, geometry, scale, and regularization (Barmin et al., 2001).

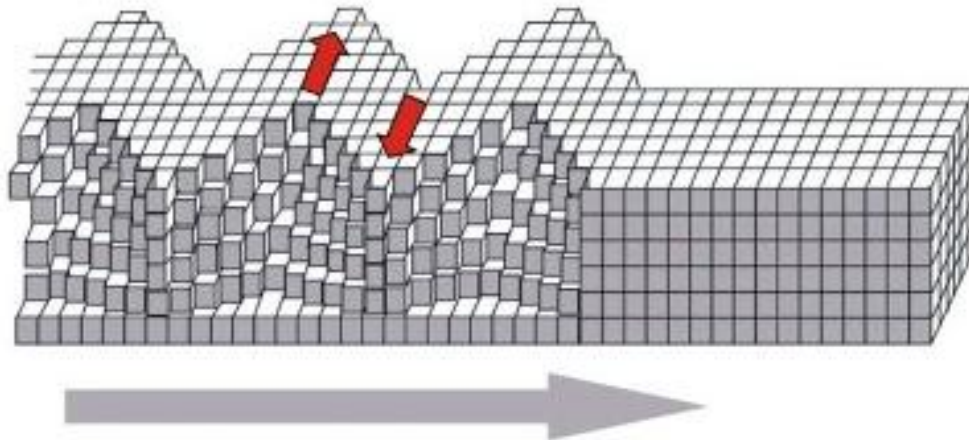
Tomographic methods aim to minimize an objective function, allowing to find an estimate for the model parameter,  $m$  (i.e. velocity structure). An example of an objective or penalty function is

$$(G(\bar{m}) - \bar{d})^T C^{-1} (G(\bar{m}) - \bar{d}) + \sum_{k=0}^n \bar{a}_k^2 \|F_k(\bar{m})\|^2 + \sum_{k=0}^n \bar{b}_k^2 \|H_k(\bar{m})\|^2, \quad (1.2)$$

where  $G$  is a vector of linear functionals,  $G_i$ ,  $d$  is data (i.e. traveltimes or traveltime residuals) and  $C$  is the *a priori* covariance matrix of observational errors (Barmin et al., 2001). The norm of an arbitrary function  $f(r)$  is defined as:  $\|f(r)\|^2 = \int_S f^2(r) dr$ . The first term in Equation 1.2 represents the data misfit. The second term is a regularization term (e.g., spatial smoothing). The third term is a weighting function that depends on path density.

## Surface waves

### Love wave



### Rayleigh wave

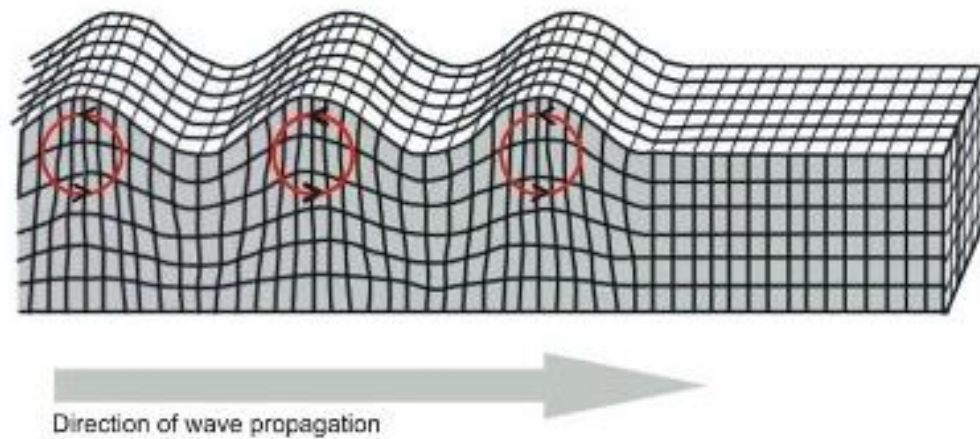


**Figure 1.10 Illustration of Love wave and Rayleigh wave propagation.**

Top image: horizontal particle motion of Love waves. Bottom image: retrograde elliptical particle motion of Rayleigh waves. (<http://www.lamit.ro/earthquake-early-warning-system.htm> accessed on March 27, 2012).

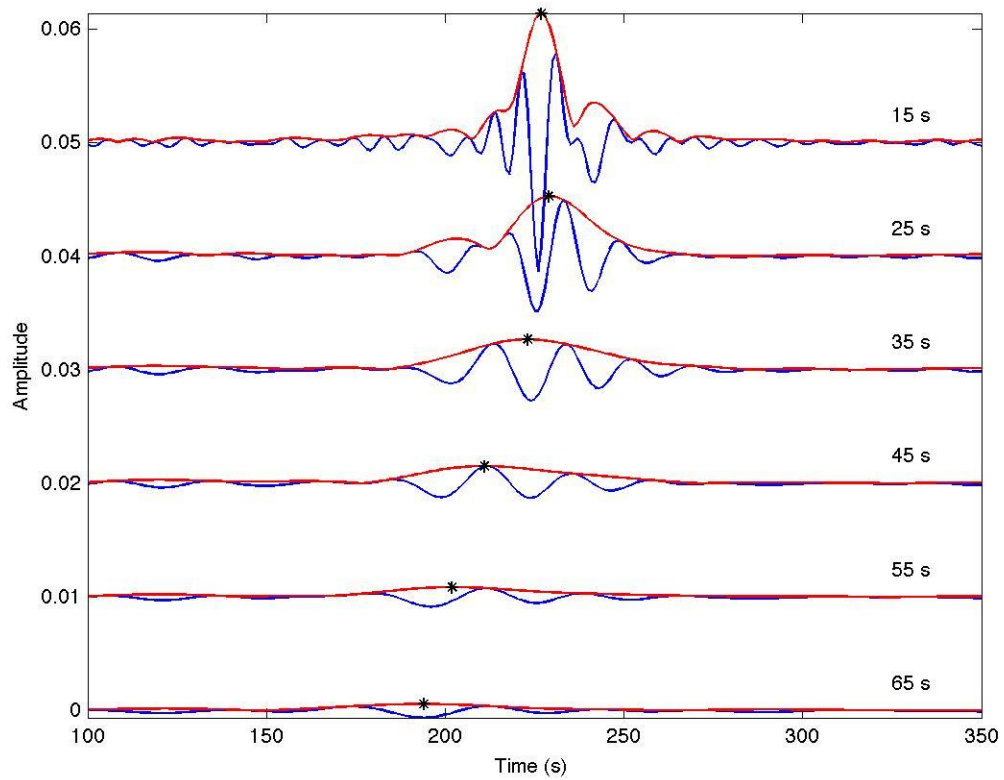


**Figure 1.11 Example of group-velocity dispersion measurement.**

Blue lines represent trace filtered at the given central period, red lines represent the amplitude envelope and the black stars show the maximum amplitude pick. Traces are shifted for illustration.

## 1.9 Previous Geophysical Constraints

Prior to the start of the HuBLE project, various other researchers studied the Hudson Bay region using a range of geophysical methods such as gravity maps, regional magnetics, and controlled-source seismic profiling. There is a strong correlation between regional magnetic and gravity anomaly patterns to major geologic structures in the Hudson Bay region (Eaton and Darbyshire, 2010). Bouguer gravity anomalies closely track the inferred outline of the Superior boundary zone, (along the margin of the Superior craton) almost continuously in Manitoba and as far east as the Ottawa Islands in eastern Hudson Bay. Another Bouguer gravity anomaly appears in the centre of the Hudson Bay basin, the origin of which has been modelled as a high-density block at the base of the crust (Eaton and Darbyshire, 2010). There is a large free-air gravity anomaly in the region of greatest thickness of the Laurentide Ice Sheet. This anomaly led to the hypothesis that the anomaly is caused by incomplete glacial isostatic adjustment (Innes et al., 1968).

Aeromagnetic anomaly maps are complimentary to gravity maps, since gravity anomalies reflect density distributions and magnetic maps reflect variations in magnetic susceptibility, which is mainly controlled by mineral phases (Beck, 1991). Generally magnetic anomalies are sensitive to shallow features in the lithosphere. Magnetic fabrics in the Hudson Bay region follow directions corresponding to the magnetite-rich orogenic belts.

Controlled-source seismic data from multichannel reflection and refraction surveys have been acquired near the Hudson Bay region as part of the LITHOPROBE program

(Clowes et al., 1992). A seismic refraction survey was also acquired in Hudson Bay as part of a major experiment in 1965 (Hobson, 1967). The surveys found large variations in crustal thickness between the Churchill and Superior cratons. Also, older vintage surveys were acquired by oil and gas industry (Roksandic, 1987); however, these profiles are severely contaminated by multiple reverberations caused by seismic energy trapped within the water layer.

### **1.10 Thesis Goals and Organization**

This thesis is organized into three parts consisting of three articles published or submitted to peer-reviewed journals. In the first study, the methodology is discussed in detail and isotropic Rayleigh-wave group-velocity maps are created and interpreted. Noise-sources are analysed for directional and seasonal variability, and point sources are located. Two hypotheses concerning the formation of the Hudson Bay basin are tested and results provide insight that help distinguish between them. In the next study, azimuthal anisotropy is incorporated into the inversion, adding complexity to the inversion process. Parameter and resolution testing is undertaken to understand and optimize the inversion and is included in Appendix A. Anisotropic parameters imaged by this study provide insight into post-collisional deformation in the lower crustal and significant anisotropy variability on either side of the Churchill-Superior suture zone. Lastly, a joint inversion of ambient-noise data and earthquake data was undertaken for isotropic variations. Results show a clear view of the crust and mantle beneath Hudson Bay, including a

prominent low-velocity feature. We interpret this as the THO suture zone manifesting in the mantle as a near-vertical low velocity band. The suture may have formed a zone of weakness that extends through the lithosphere providing a locus for initiation of localized lithospheric stretching.

### **1.11 Published Work and Author Contributions**

Chapter Two consists of previously published material regarding isotropic velocity structure. In Chapter Two (Pawlak et al., 2011) the ambient-noise method is introduced and improvements to account for asymmetric source distribution are made. The processing method described in Chapter Two is used in subsequent chapters throughout this thesis. Chapter Three consists of a manuscript that has been submitted to a peer-reviewed journal and is currently in the review process. In Chapter Three (Pawlak et al., 2012) azimuthal anisotropy is added to the inversion process to further constrain the subsurface structure. Chapter Four consists of a manuscript in preparation for publication. Chapter Four is a collaborative project, adding teleseismic surface wave data, processed by Fiona Darbyshire at the Université du Québec à Montréal, for a joint inversion between ambient-noise data to improve resolution in the crust and upper mantle.

The author's contributions consisted of gathering data, writing the majority of the software required to process the data excluding the inversion processes, the bulk of manuscript writing, preparing figures, editing the manuscript for submission, applying

reviewers' comments and suggestions, and communicating with co-authors' and journal editors.

Chapter Two: **CRUSTAL STRUCTURE BENEATH HUDSON BAY FROM  
AMBIENT-NOISE TOMOGRAPHY: IMPLICATIONS FOR BASIN  
FORMATION**

**Summary**

The Hudson Bay basin is the least studied of four major Phanerozoic intracratonic basins in North America and the mechanism by which it formed remains ambiguous. We investigate the crustal structure of Hudson Bay based on ambient-noise tomography, using 21 months of continuous recordings from 37 broadband seismograph stations that encircle the Bay. Green's functions that emerge from the cross-correlation of these ambient noise recordings are dominated by fundamental-mode Rayleigh waves. In the microseismic period band (5 – 20 s), these signals are most prominently expressed in certain preferred azimuths indicative of stationary coastal source regions in southern Alaska and Labrador. Seasonal variations are subtle but consistent with more energetic noise sources during winter months, when wave heights in the Pacific and north Atlantic are larger than in the summer. Noise emanating from Hudson Bay does not appear to

contribute significantly to the cross-correlograms. Group-velocity dispersion curves are obtained by time-frequency analysis of cross-correlation functions. We test and implement a signal-to-noise ratio (SNR) selection method for producing one-sided cross-correlograms, which yields better-defined dispersion ridges than the standard two-sided averaging approach. Tomographic maps and cross-sections obtained in the 5-40s period range reveal significantly lower crustal velocities beneath Hudson Bay than in the bounding Archean Superior craton. The lowest mid-crustal velocities correspond to a previously determined region of maximum lithospheric stretching near the centre of the basin. Pseudo-sections extracted from the tomographic inversions along profiles across Hudson Bay provide the first compelling direct evidence for crustal thinning beneath the basin. Our results are consistent with a recent estimate of 3 km of crustal thinning, but not consistent with a proposed model for basin subsidence triggered by eclogitisation of a remnant crustal root.

## **2.1 Introduction**

Hudson Bay is a vast region of flooded cratonic lithosphere that conceals several major tectonic elements of the North American continent, including the Paleozoic Hudson Bay basin and its underlying Archean to Proterozoic basement (Eaton and Darbyshire 2010; Corrigan, 2010). In the 1960s, the crustal architecture of Hudson Bay was investigated based on a major seismic refraction program (Hobson, 1967; Hunter and Mereu, 1967, Ruffman and Keen, 1967; Barr, 1967). Subsequently, regional crustal structure was

studied using gravity and magnetic observations (Coles and Haines, 1982; Gibb 1983) as well as industry seismic profiles (Roksandic, 1987). For the last few decades, however, the crustal structure of this region has received scant attention due to lack of new data. Renewed interest has arisen from the Hudson Bay Lithospheric Experiment (HuBLE), an international initiative that is currently operating more than 40 broadband seismograph stations around the periphery of Hudson Bay (Figure 2.1).

Ambient-noise tomography, which uses the cross-correlation of diffuse wavefields (e.g. ambient noise, scattered coda waves) to estimate the Green's function between pairs of seismic stations, is rapidly emerging as a popular tool for crustal studies. The first applications of this method in southern California (Shapiro et al., 2005; Sabra et al., 2005b) showed that regional geological features such as sedimentary basins and large igneous batholiths could be reliably imaged using this approach. Ambient-noise tomography has since been applied to investigate crustal structure in Korea (Cho et al., 2006), New Zealand (Lin et al., 2007), Europe (Yang et al., 2007) and elsewhere in the western U.S. (Moschetti et al., 2007). The method continues to be refined, but standard data-processing algorithms are emerging (e.g., Bensen et al., 2007).

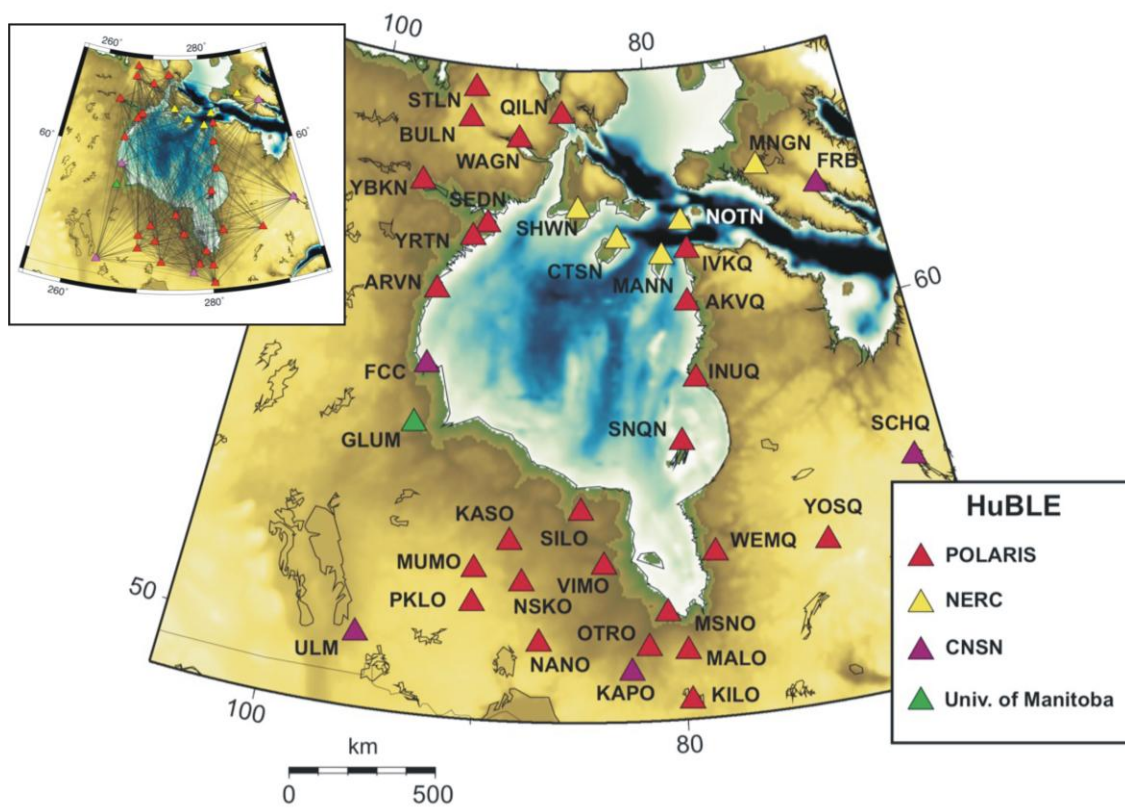


**Figure 2.1 Map of Hudson Bay seismograph stations.**

Map of Hudson Bay showing HuBLE stations used in this study. Inset (upper left) shows all two-station paths.

Ambient-noise tomography is well suited for the investigation of crustal structure beneath Hudson Bay using data from HuBLE, since the stations are deployed peripherally, providing good two-station path coverage in the Bay's interior (Figure 2.1). In contrast, methods such as body wave tomography and receiver function analysis would require stations within the Bay. This chapter presents a tectonic interpretation based on processing and analysis of 21 months of continuous ambient noise sequences recorded at 37 broadband seismograph stations. Our study includes an analysis of signal-to-noise characteristics versus azimuth, from which ambient-noise source regions around Canada are inferred. We use the ambient-noise tomography results to test two competing hypotheses for the origin of the Hudson Bay basin (Figure 2.2). According to one hypothesis, basin subsidence was triggered by eclogite phase transformation within an orogenic crustal root (Fowler and Nesbit, 1985; Eaton and Darbyshire, 2010); according to the second, basin subsidence occurred in response to lithospheric extension that resulted in crustal thinning (Hanne et al., 2004). These hypotheses make different predictions about crustal thickness trends that are potentially testable using this approach.

A third hypothesis, in which subsidence occurred as a result of convective downwelling within the mantle (James, 1992; Peltier et al., 1992), has been suggested to explain the long-wavelength negative gravity anomaly and circular basin beneath Hudson Bay. As described below, our data are sensitive to velocity structure to a maximum depth of about 80 km. With an average crustal thickness of about  $38 \pm 1$  km (Thompson et al., 2010), this depth limit is sufficient to image the Moho but not the base of the lithosphere, which occurs much deeper beneath Hudson Bay (Darbyshire and Eaton, 2010). Since a mantle

downwelling would occur below the lithosphere, our data do not provide a diagnostic test of this third hypothesis.

## **2.2 Tectonic Setting**

Hudson Bay is an epicontinental sea with an average water depth of about 100m. It formed by inundation of the interior of the North American continent via Hudson Strait to form the Tyrell Sea (ancestral Hudson Bay), immediately following Laurentide ice-sheet deglaciation (Lee, 1968). Ongoing uplift, driven by incomplete glacial isostatic adjustment (GIA), has occurred since the last glacial maximum (e.g., Lee et al., 2008) and continues to expose new islands. The present submerged area of Hudson Bay corresponds roughly with the extent of the Paleozoic Hudson Bay basin (Figure 2.3), a saucer-shaped basin within the Canadian Shield with a maximum preserved sediment thickness of about 2 km. Basin subsidence initiated in the Late Ordovician and persisted for about 100 Myr (Hamdami et al., 1991). Although largest by surface area of four roughly synchronous intracratonic basins in North America (Williston, Michigan, and Illinois), the Hudson Bay basin is also the shallowest, possibly due to the presence of thick, cold (and therefore relatively stiff) underlying lithospheric mantle (Eaton and Darbyshire, 2010).

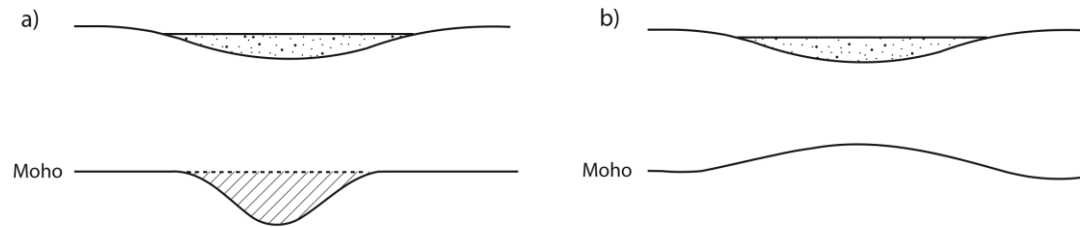


**Figure 2.2 Schematic of proposed hypotheses.**

Two proposed hypotheses (not to scale) for formation of the Hudson Bay basin. a) Basin formation in response to a buried load caused by eclogitisation of a crustal root (Eaton and Darbyshire, 2010). b) Basin formation by lithospheric stretching (Hanne et al., 2004). These models make different predictions, namely crustal thickening and thinning, respectively, beneath the centre of Hudson Bay.

The Hudson Bay basin rests unconformably on crust that formed or was largely reworked during the Paleoproterozoic (ca. 1.9-1.8 Ga) Trans Hudson Orogeny (THO; Eaton and Darbyshire, 2010; Corrigan et al., 2010). The product of double-indentation collision between the Archean Superior and Churchill plates (Gibb, 1983), the THO is considered to be similar in spatial and temporal extent to the modern Himalaya-Karakoram orogeny (St. Onge et al., 2006). Tectonic subdivisions of the Precambrian basement beneath the Hudson Bay basin are inferred mainly from potential-field data, and feature a SW-NE trending suture that forms the boundary between the Archean Superior and Rae-Hearne domains (Figure 2.3; Eaton and Darbyshire, 2010). According to this model, tectonic domains SE of the suture are interpreted as the reworked passive margin of the Archean Superior craton, together with accreted island-arc terranes; tectonic domains NW of the suture are interpreted as either part of the Neoproterozoic Hearne domain (Hanmer et al., 2004) or as a distinct fragment of older continental lithosphere (Roksandik, 1987; Berman et al., 2005).

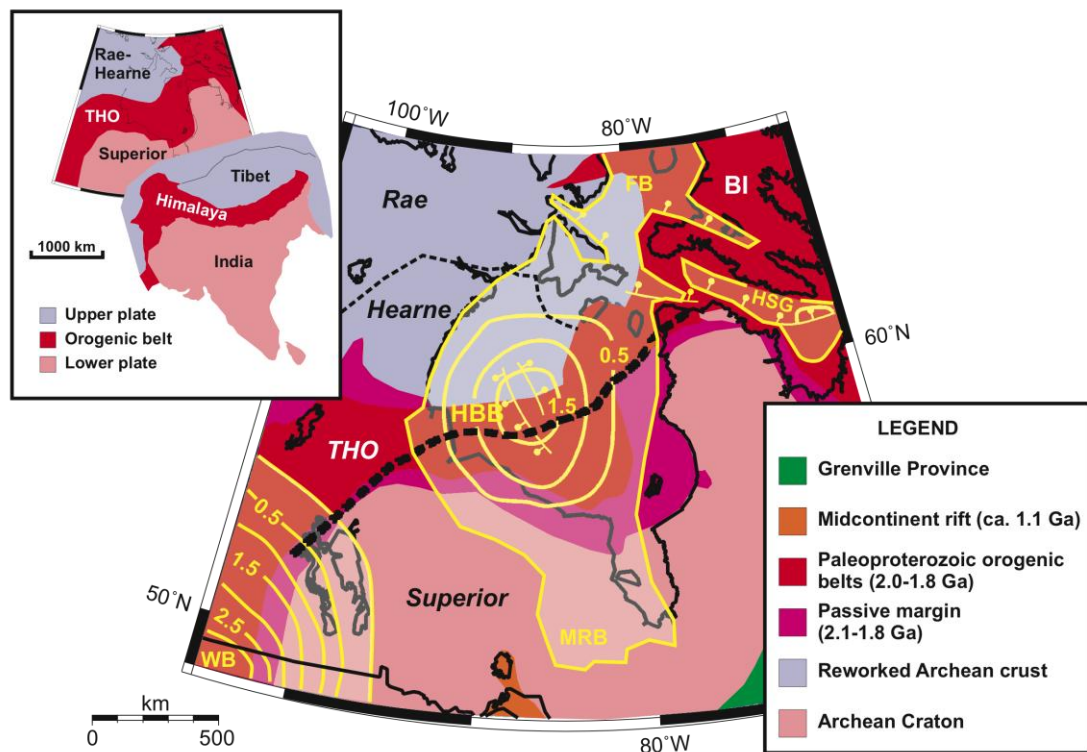


**Figure 2.3 Generalized geology map.**

Generalised geology, showing mapped faults and total sediment isopach contours in km in the Hudson Bay basin (HBB; Sanford, 1990). These are superimposed on major tectonic subdivisions of the Hudson Bay region (Eaton and Darbyshire, 2009); bold dashed line shows inferred principal suture. Upper left inset compares the scale of the Trans-Hudson orogen (THO) with the modern Himalayan orogen (after St. Onge et al., 2006). WB, Williston Basin; MRB, Moose River Basin; HSG, Hudson Strait Graben; FB, Foxe Basin; BI, Baffin Island.

Receiver-function analysis of new data from the HuBLE experiment reveals a remarkably uniform crustal thickness of about  $38 \pm 1$  km around the periphery of Hudson Bay (Thompson et al., 2010). In contrast to this apparent lack of Moho relief, systematic variability in average crustal  $V_p/V_s$  and Moho signature appear to correlate with crustal formation age (Thompson et al., 2010). Within the Bay, significant variations in crustal thickness (26-40 km) have been interpreted based on wide-angle/refraction data, albeit subject to large uncertainties due to inadequacies in the marine navigation equipment available at that time (Ruffman and Keen, 1967). Noting issues arising from the underlying assumptions in the time-term method used to interpret these refraction data, Hanne et al. (2004) suggested that crustal thinning of about 3 km is more consistent with observed basin subsidence curves.

### **2.3 Data and Initial Processing**

We have analyzed continuous data from 37 broadband seismic stations deployed around Hudson Bay as part of the HuBLE experiment. The raw data consists of three-component measurements of ground motion with a sampling rate of 40 samples per second. The time interval considered here spans 21 months, starting from September 2006 and ending May 2008. Of the 37 stations, 5 stations, located in northern Hudson Bay, belong to the HuBLE NERC network (e.g., Bastow et al., 2010) and 1 station, located in northern Manitoba, belongs to the University of Manitoba (Figure 2.1).

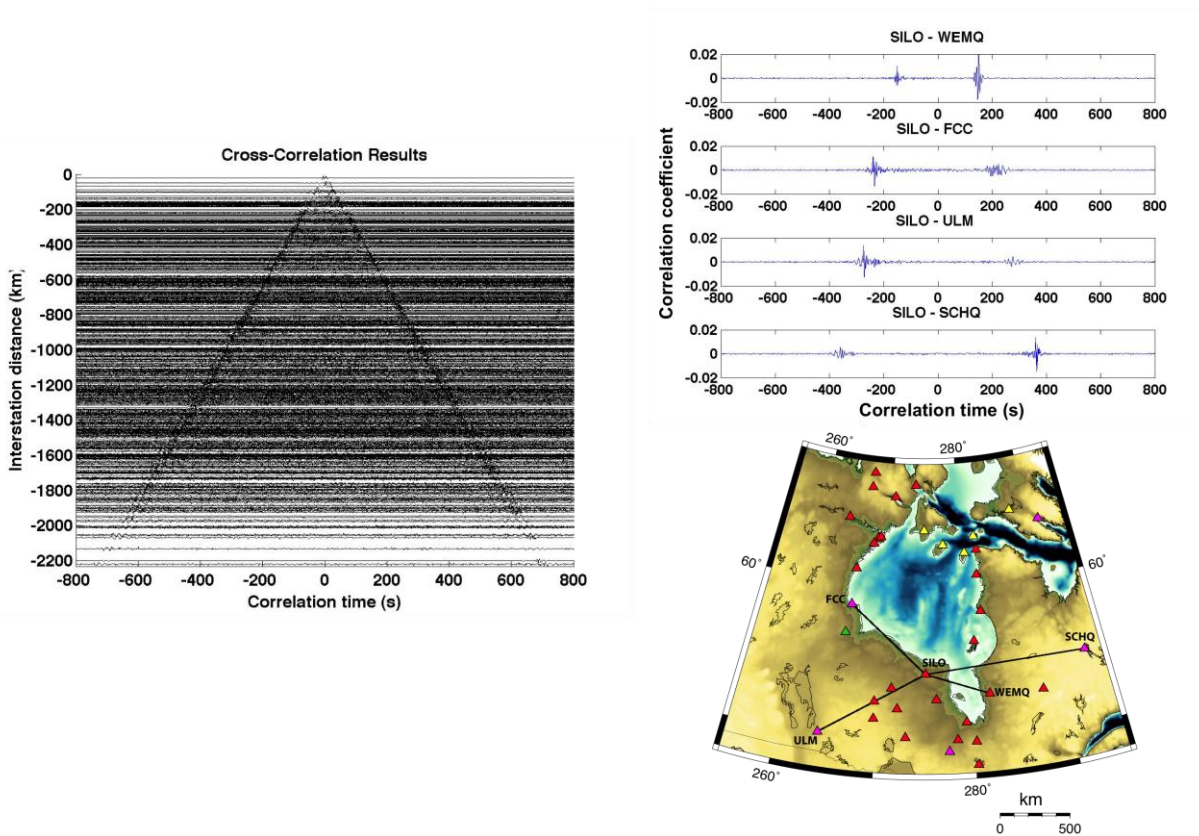


**Figure 2.4 Cross-correlations.**

Stacked cross-correlations versus interstation distance for 591 two-station paths (left). Both positive and negative lags are shown. Examples of five cross-correlations (upper right) illustrates asymmetry of correlograms with respect to signal-to-noise ratio (SNR), typical of this dataset. Corresponding paths are shown in the lower right.

Our data-processing procedure follows Bensen et al. (2007). First, the data were split and decimated by cutting the recordings into individual one-day records and resampling to 1 Hz. Next, we removed the daily trend, mean and instrument response from the raw signals. A one-bit normalisation procedure was then applied to remove unwanted earthquake signals and instrument irregularities, which obstruct the broadband ambient-noise signal. This procedure is accomplished by generating a data stream of 1's and -1's, retaining only the sign and disregarding the amplitude of the signal (Yang et al., 2007). Bensen et al. (2007) referred to this step as temporal normalisation. This is followed by spectral normalisation, which acts to broaden the frequency band of the noise data, and then bandpass filtering between 0.005Hz and 0.3Hz.

After the daily time series are processed, cross-correlations were performed between all possible station pairs and all available daily records. Shapiro et al. (2005) found that coherent empirical Green's functions (EGFs) emerged from their Californian dataset using only one month of data. We found, however, that averaging of cross-correlation signals over long time periods (typically 6 months or more) is generally necessary for emergence of clear signals from the Canadian data. The total number of station pairs is  $n(n-1)/2$ , where  $n$  is the number of stations (Bensen et al., 2007). With 37 stations, 666 station pairs are thus available, of which 591 proved to be usable based on assessment of data quality. Figure 2.4 shows a 21-month stack of  $z$ -component cross-correlation functions plotted against interstation distance. A clear linear trend is evident for both the positive and negative lags of the signal, referred to as causal and acausal signals, respectively (Bensen et al., 2007). Since the vertical component is used in the present

analysis, these signals are dominated by fundamental-mode Rayleigh waves travelling between the two stations in opposite directions (Lin et al., 2007).

### *2.3.1 Directionality and Seasonality*

In principle, the emergence of Green's functions from cross-correlation of a diffuse wavefield assumes that ambient-noise sources are distributed homogeneously in azimuth (Shapiro et al., 2005). Careful inspection of our stacked cross-correlation functions, however, reveals a persistent asymmetry in which one half has significantly higher SNR than the other (Figure 2.4). This type of asymmetry is characteristic of stationary coastal noise sources (Stehly et al., 2006). SNR is defined here as the ratio of the peak amplitude in a signal window to the root-mean-square amplitude in a trailing window, where both windows have a length of 500s (Bensen et al., 2007). Although it is a measurement in the time domain, this can be considered as a 'spectral' SNR, because it is calculated for a grid of central frequencies. Here we use a range between 0.01 Hz to 0.25 Hz (or 4 - 100 s).

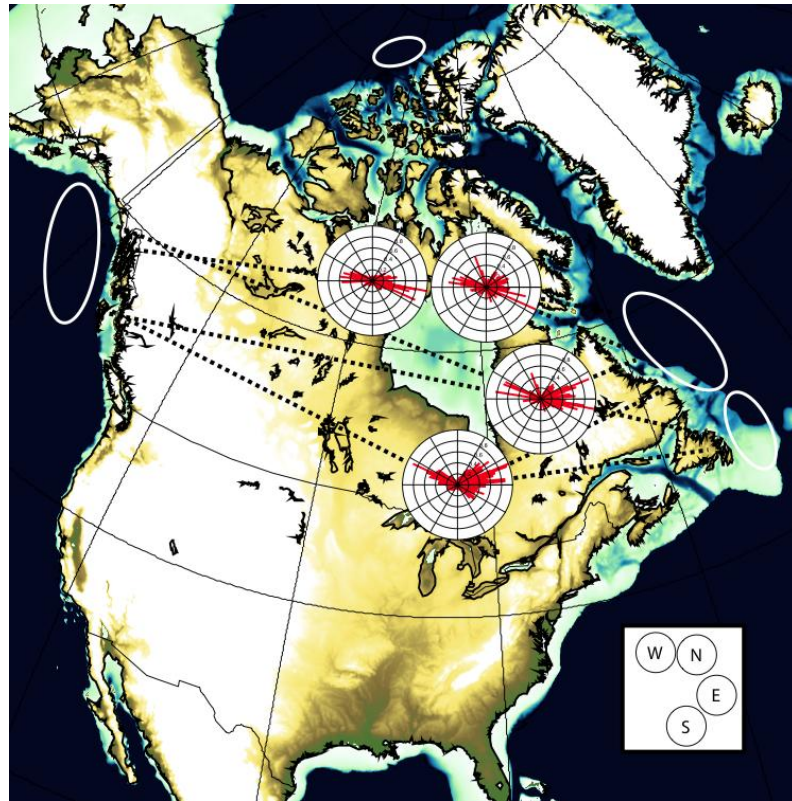


**Figure 2.5 Directionality of noise sources.**

Rose plots showing the dominant directions of noise signals for clusters of stations (W, N, E, and S, as shown in inset) around Hudson Bay. Map is plotted using an azimuthal projection so that directions can be extrapolated in a linear fashion, as indicated by the dashed lines. Possible locations of stationary coastal sources are indicated by white ellipses. SNR values used to compute the rose diagrams are normalised and weighted based on distance between stations.

To look for source directionality in our data, we have computed rose plots of SNR for groups of stations situated in quadrants around Hudson Bay (Figure 2.5). The rose diagrams are computed from both the causal and acausal parts of the cross-correlation functions and reveal the asymmetry of seismic noise sources in the region. In these diagrams, SNR is normalised by the square root of interstation distance, allowing an unbiased representation of noise sources. The rose plots are arranged on an azimuthal map projection so that dominant directions can be extrapolated linearly to the nearest coastal region, rather than along curved great-circle paths.

This study area experiences extreme seasonal variability in coastal conditions. The surface of Hudson Bay is frozen during winter months, the Arctic coast of Canada experiences dramatic seasonal variations in sea ice cover, and wave height in the North Atlantic Ocean and Labrador Sea (Capon, 1973) vary considerably with time of year due to winter storm activity. To investigate the effect of these seasonal variations, we computed rose diagrams based on cross-correlation functions that are confined to different seasonal time windows (Figure 2.6). The cross-correlation functions are separated into 5-month stacks representing the northern summer and northern winter months. The northern summer stack is centred on July, encompassing May, June, August and September, while the northern winter stack is centred on January, encompassing November, December, February and March. Generally the summer months show more azimuthally distributed noise sources with higher SNR, compared to the winter months. These SNR calculations are made for different period bands that represent the primary and secondary microseism bands, as well as Earth ‘hum’ for the longer periods. The short

periods ( $< 20$  s) are referred to as microseisms composed of the primary (10 – 20 s) and secondary (5 – 10 s) microseism bands (Stehly et al., 2006). The primary band is believed to be associated with low-pressure atmospheric disturbances near coastlines (Capon 1973) and represents the interaction between ocean swells and the shallow seafloor (Hasselmann, 1963; Yang and Ritzwoller, 2008), while the secondary band is believed to represent the nonlinear interaction of primary waves travelling in opposite directions with the same frequency (Longuet-Higgins, 1950; Stehly et al., 2006).

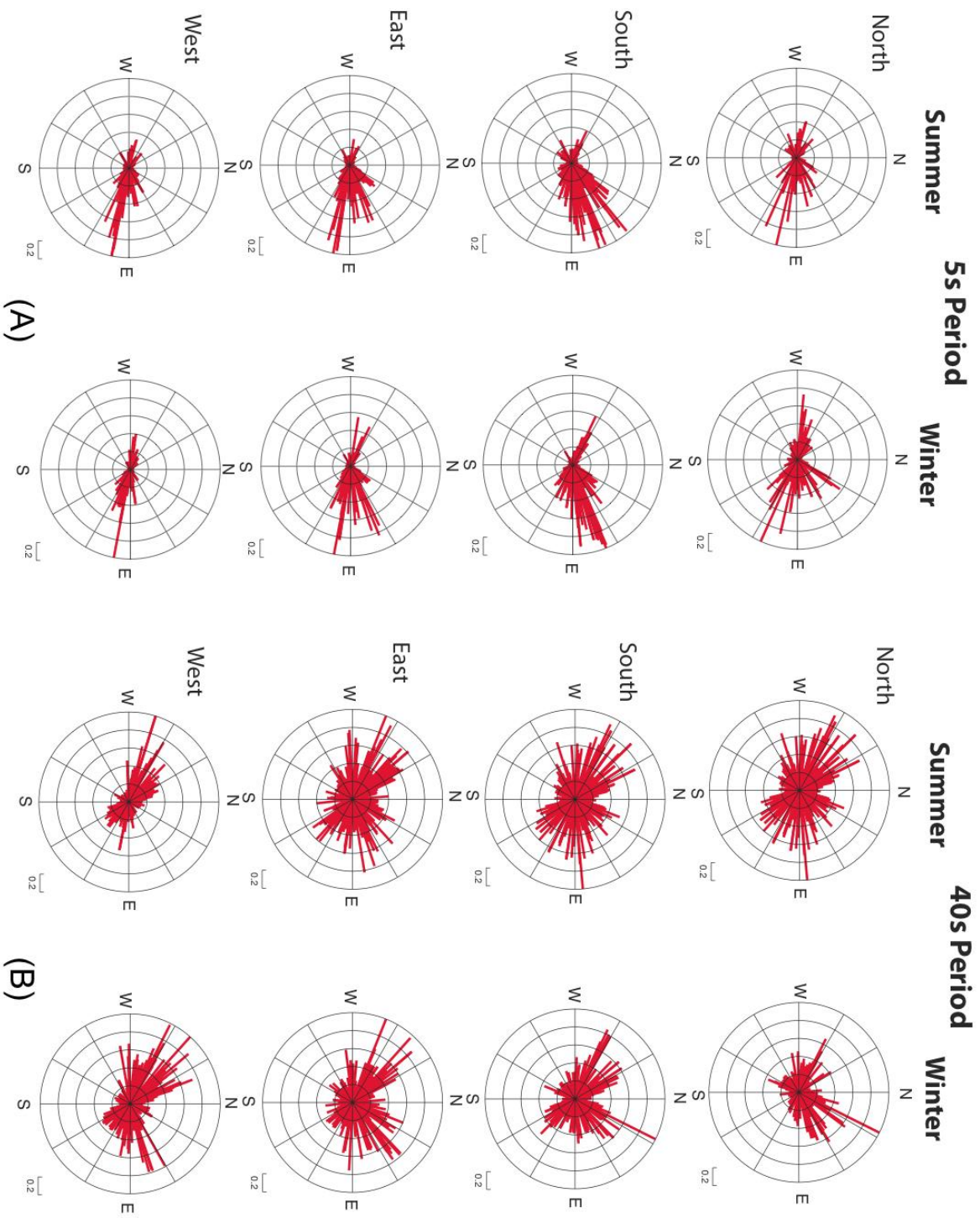


**Figure 2.6 Seasonality of noise sources.**

Rose diagrams subdivided by 5-month seasons, for 5s (a) and 40s (b) periods representing distinct modes of noise generation (see text). Each row represents a cluster of stations in N, S, E and W quadrants around Hudson Bay (see Figure 2.5). For each subplot, the left column represents summer months (May-September) and the right column represents winter months (November – March).

---

### 2.3.2 Dispersion Analysis

The next step in the analysis is to estimate group-velocity dispersion curves from the EGFs using frequency-time analysis (Bensen et al., 2007). For each EGF, a time window is selected that is centred on the fundamental-mode Rayleigh waveform. The windowed data is filtered using a set of narrow-frequency bands, and the amplitude envelope for each filtered trace is computed using its analytic signal (White, 1991). Filtering is done using a Gaussian filter centred at frequencies ranging from 0.01 – 0.25Hz. The envelope traces are sorted by mean period and arranged column-wise into a matrix. The trend of the maximum amplitude in each column (Figure 2.7) usually forms a prominent dispersion ridge that is tracked to obtain a frequency-dependent travel-time, from which group velocity can be determined based on inter-station distance. The group velocity picks were visually inspected for consistency, and noisy or invalid measurements were discarded. For each period of interest, this resulted in a set of valid two-station path measurements of group velocity for further analysis.

In previous studies, causal and time-reversed acausal halves of individual stacked cross-correlations are summed prior to further analysis of the EGFs. This stacking procedure is expected to increase the SNR by a factor of  $\sqrt{2}$  (Sheriff and Geldart, 1995) assuming Gaussian random noise and identical signal components. In virtually every case examined in this study, however, the signal amplitude of each half is sufficiently different that the assumptions underlying this approach to stacking are clearly not satisfied. As an alternative to summing both halves of the stacked cross-correlation function, we have adopted an approach in which either the causal or (time-reversed) acausal half is selected based on which has the highest SNR. Both conventional (i.e., two-sided summation of the correlation functions) and our one-sided SNR selection approach for determining the EGFs were tested. Figure 2.8 shows a comparison of the time-frequency plots obtained using the two different methods. We found that, while the differences are minor, SNR-based selection ultimately yields better-defined dispersion ridges.

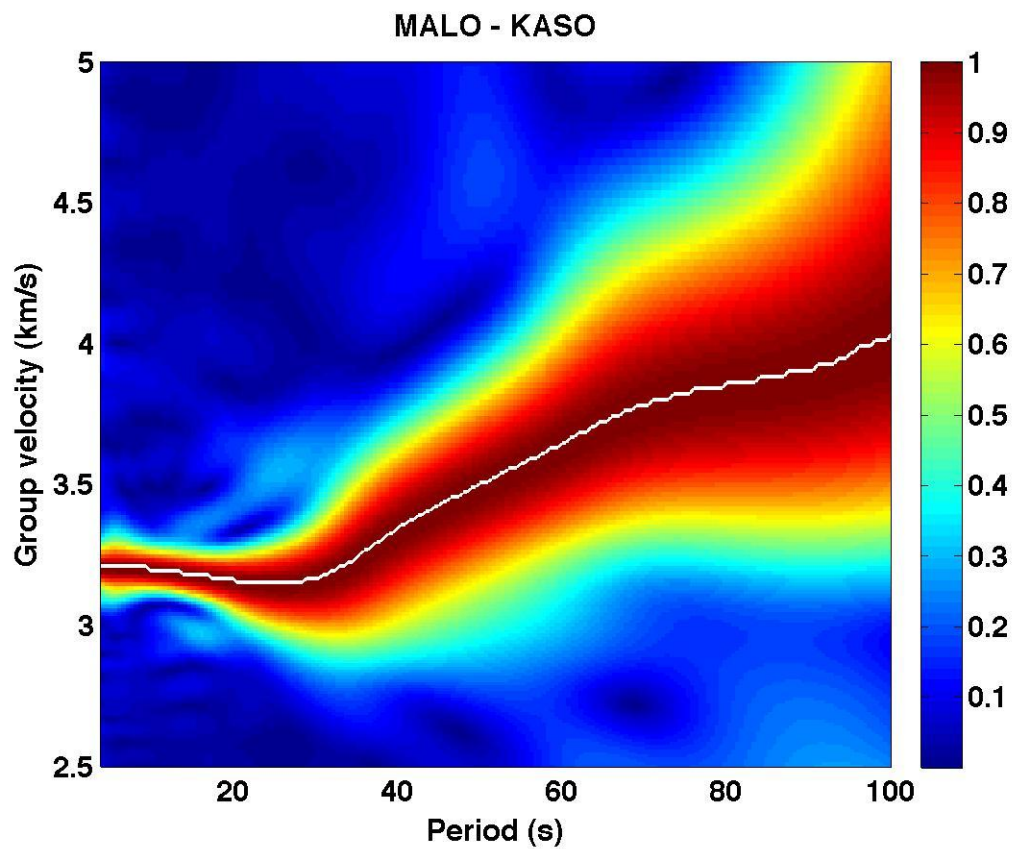


**Figure 2.7 Example of Dispersion Analysis.**

Example time-frequency plot and dispersion analysis. The colour scale shows the amplitude envelope, normalised for each period value. The white line shows the measured group-velocity dispersion curve.

### 2.3.3 1D Inversion

Group-velocity dispersion measurements can be used to estimate a 1D model of shear-wave velocity. Although the resulting uncertainties are large, this approach is useful for determining depth sensitivity as an aid for interpreting the tomographic reconstructions. Here we use a two-stage inversion procedure, as described by Shapiro and Ritzwoller (2002). The first stage involves linearised least-squares inversion using the method of Herrman and Ammon (2002), starting from an *a priori* initial model. The second stage uses a Monte-Carlo scheme to perturb the model, to seek other models that fit the observed dispersion data to within uncertainty. The initial model is derived from Darbyshire and Eaton (2010) and consists of two uniform layers, representing the crust ( $V_p = 6.48$  km/s,  $V_s = 3.6$  km/s and  $2.76$  gm/cm<sup>3</sup>) and upper mantle ( $V_p = 8.04$  km/s,  $V_s = 4.48$  km/s and  $3.34$  gm/cm<sup>3</sup>). The Moho is initially assigned a depth of 38km, consistent with average crustal thickness around Hudson Bay (Thompson et al. 2010). The velocity model is parameterised using layers that are 2 km thick, in order to accommodate velocity gradients and variations in crustal thickness. The inversion step is performed until a stable result is achieved.

Constraints are imposed on the models to ensure realistic final models. In particular, velocity variations from the initial model are limited to  $\pm 5\%$  and  $\pm 10\%$  for the crust and mantle, respectively. The Moho depth is permitted to vary between 36 and 40 km and the  $V_p/V_s$  ratio is set to 1.73, based on receiver-function analysis (Thompson et al., 2010). During each iteration in the second stage, a new starting model is obtained by adding random perturbations to the previous model following the constraints listed above. A

synthetic dispersion curve is calculated and compared with original dispersion curve from the data. If the synthetic dispersion curve fits the observed data to within a user-defined error bound based on data error estimates, then the model is retained. This model is now used as the starting model for the next set of random perturbations. This procedure is run for a subset of dispersion curves. Inversion results obtained using this procedure are described below in section 2.4.

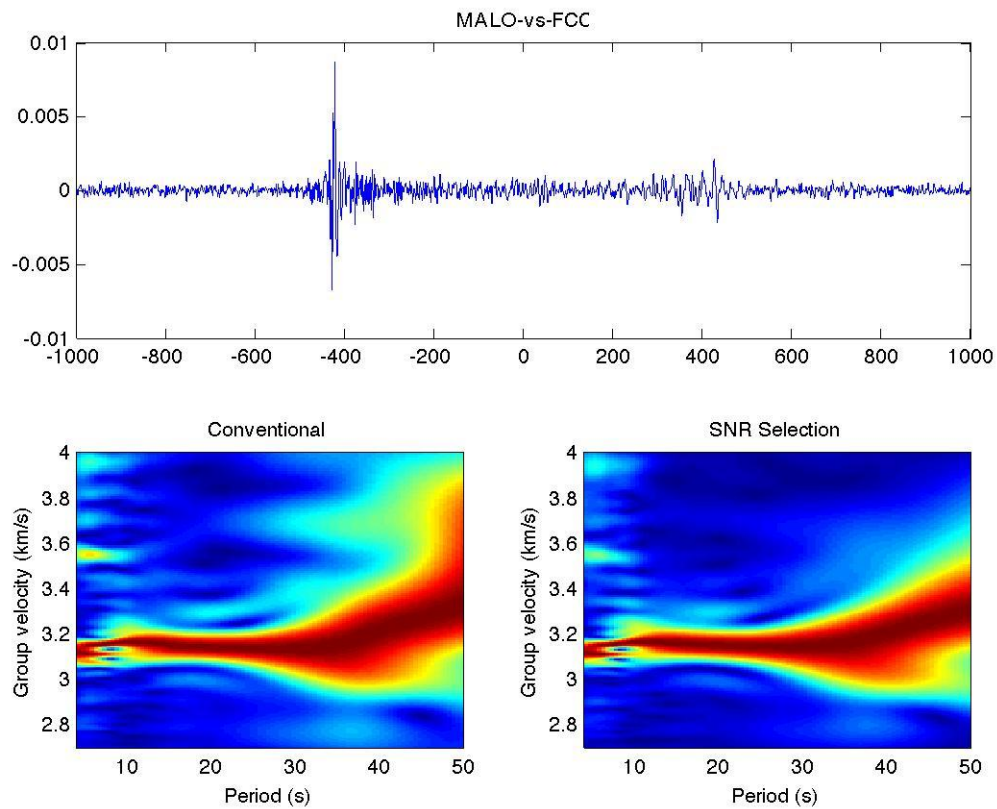


**Figure 2.8 Conventional versus SNR selection method.**

Example cross-correlogram (top) and dispersion analyses (bottom) for the conventional two-sided averaging approach (left) and the one-sided SNR selection approach used here (right). The dispersion results are generally very similar, but our preferred method is the SNR selection approach since the dispersion curve is better defined.

## 2.4 Tomographic Imaging

Rayleigh-wave group-velocity dispersion measurements in the period range of 5-40 s are used here to construct tomographic images of Hudson Bay based on the method of Barmin et al. (2001). This method inverts surface-wave group (or phase) velocity dispersion measurements to estimate 2D models of the distribution and amplitude of the velocity variations on a spherical grid. The resulting tomographic maps represent a local spatial average of group velocity in each area on the map. Although the method has an option for handling azimuthal anisotropy, the present study assumes isotropic velocities. The inversion method of Barmin et al. (2001) is one of many inversion procedures for inverting surface-wave data. Since the input required for this method is Rayleigh wave dispersion measurements, it also allows inverting ambient-noise data, creating robust and reliable dispersion maps (Barmin et al., 2001) on a  $1^\circ \times 1^\circ$  grid across Hudson Bay. The method is based on minimising a penalty function composed of a linear combination of data misfit, model smoothness, and the perturbation to a reference model (Yang et al., 2007). For regions of poor data coverage the estimated model blends with the reference model. In this case no external reference model was used, so average measurements at each period are used as the reference model (Lin et al., 2007).

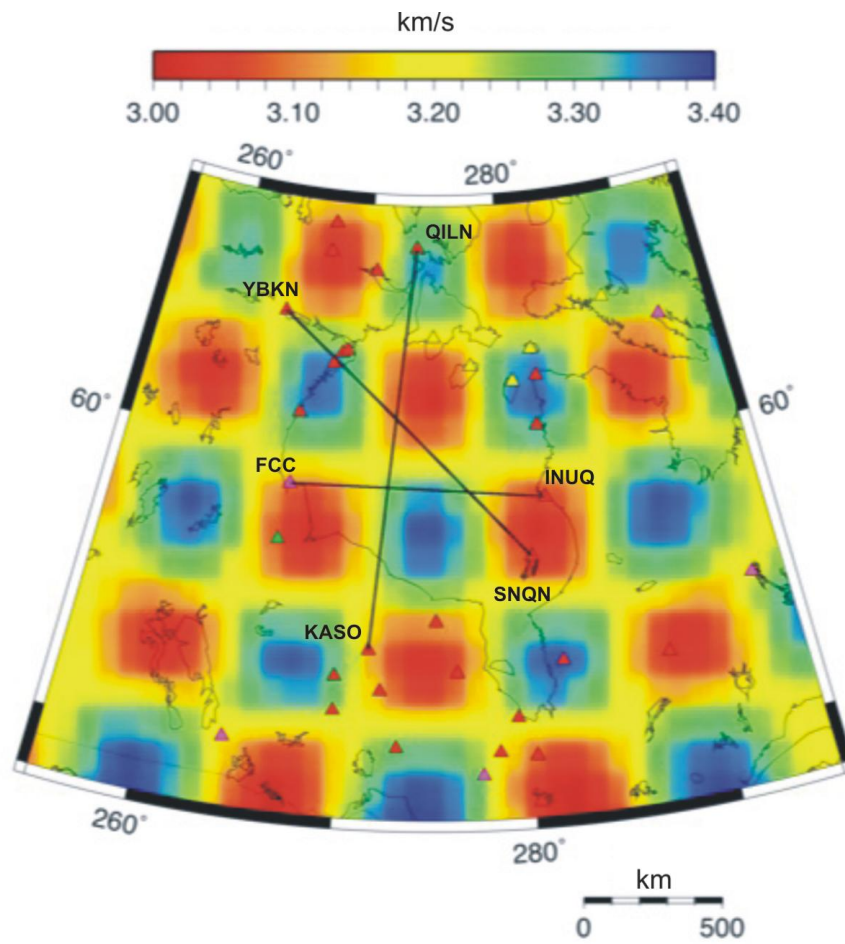


**Figure 2.9 Checkerboard model.**

Checkerboard model used for resolution testing. Black lines indicate pseudo-section locations (Figure 2.13).

Resolution analysis was performed using a checkerboard model to evaluate limitations of the recovered tomographic images under ideal conditions. The checkerboard model has a background velocity of 3.21 km/s, with superimposed alternating circular high and low velocity anomalies (Figure 2.9). The anomalies are 200 km in radius, are separated by a gap of 400 km between their centres, and have uniform velocities of 3.4 km/s and 3.0 km/s, respectively. The tomographic inversion procedure was carried out for periods between 5 – 40 s periods, which spans the two main microseismic noise bands as well as part of the period range for Earth ‘hum’ (e.g., Rhie and Romanowicz, 2004). In this analysis, the determining factor for model reconstruction is the available two-station path distribution, which depends upon the number of valid group-velocity measurements available for each period. Resolution of the reconstructed images (Figure 2.10) is poor at short- and long-period limits of 5 s and 40 s, as a result of sparse path coverage. For some of the longer periods (25 – 35 s), a smearing effect is apparent in the northwest corner; this has been taken into consideration when interpreting the results.

In general, very good resolution is observed across most of the Hudson Bay region. Within this region, the amplitudes and shapes of velocity anomalies have been recovered reasonably well, providing confidence for the interpretation of the data.

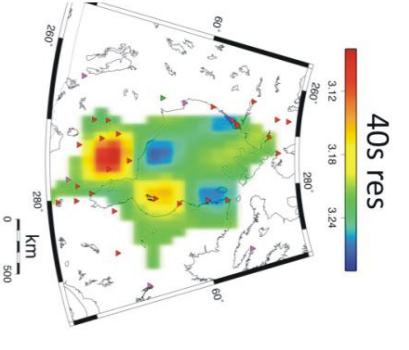
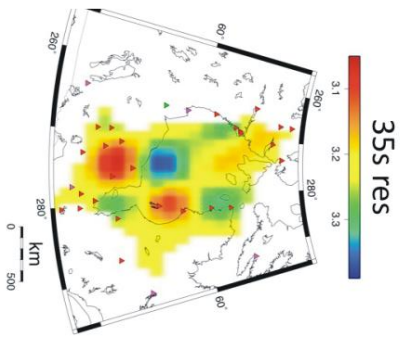
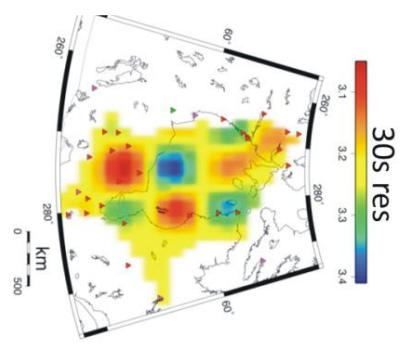
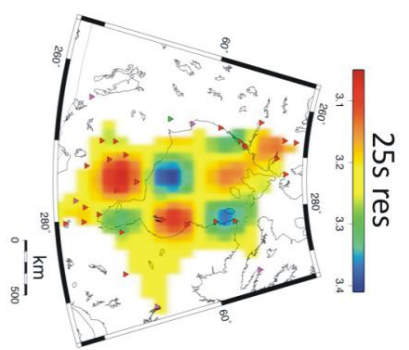
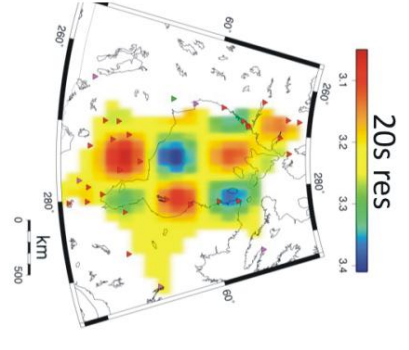
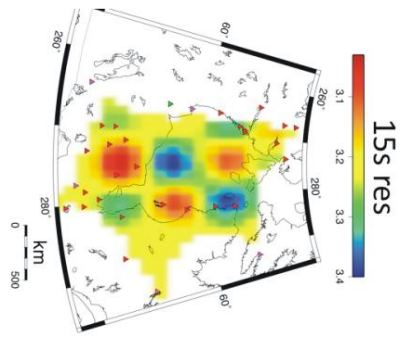
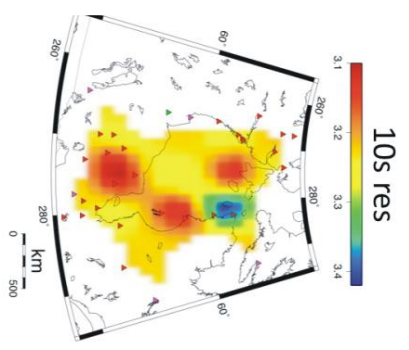
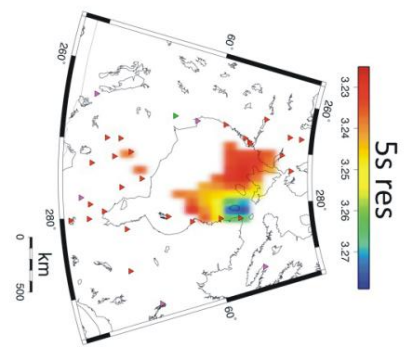


**Figure 2.10 Checkerboard reconstruction results.**

Areas with low path coverage have been masked (shown as white regions). Poor resolution due to inadequate path coverage is seen for 5 s and 40 s periods, whereas good resolution is evident for other periods. The best resolution is seen in the centre of Hudson Bay, where there is the highest density of path coverage.

---

**2.5 Results**

Tomographic reconstructions for the two EGF calculation methods are shown in Figure 2.11 and 2.12, respectively. Both methods yield similar results; we prefer the SNR selection method for EGF calculation (Figure 2.13) because the time-frequency plots have better-defined dispersion ridges. We remark that the period of fundamental-mode Rayleigh group velocity in units of seconds corresponds approximately with the depth range of sensitivity in km (Lin et al., 2007). Given the available information on average crustal thickness around Hudson Bay ( $38 \pm 1$  km; Thompson et al., 2010), the 5-40 s period range used here are thus mainly sensitive to depths from the upper crust to the uppermost mantle. Hudson Bay has an average water depth of about 100 m, which is well above our shallowest depth sensitivity of 5 km. The water in the Bay thus has negligible effect on our data.

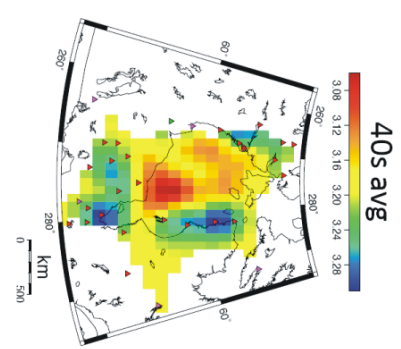
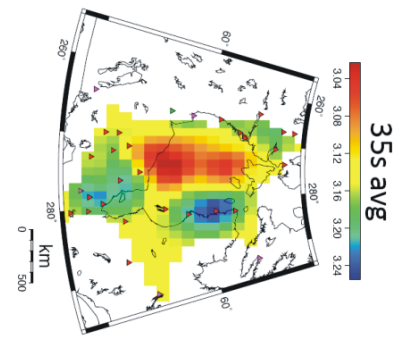
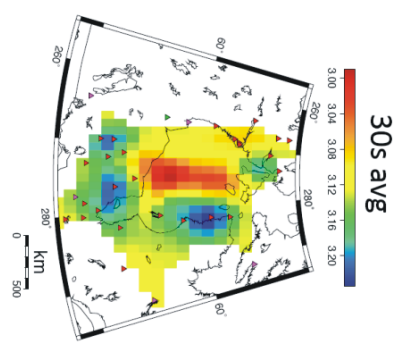
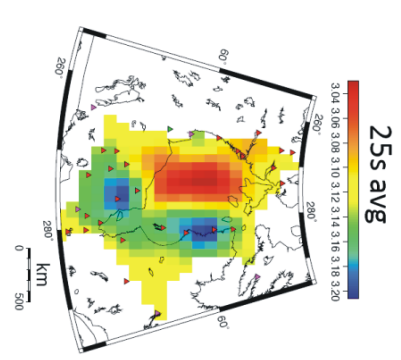
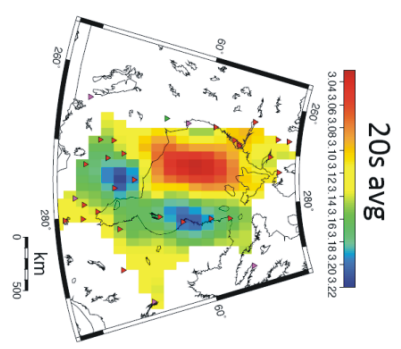
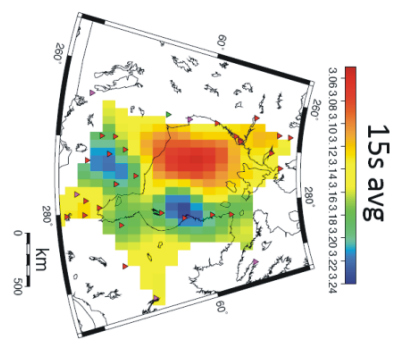
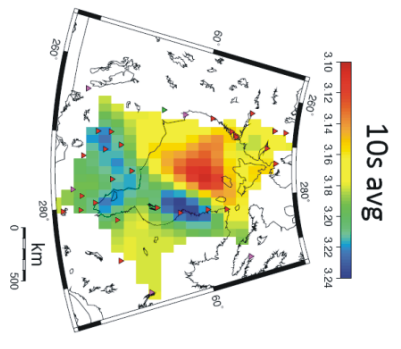
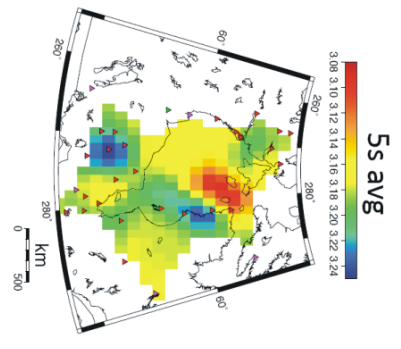


**Figure 2.11 Two-sided empirical Green's Function (EGF) tomographic reconstruction.**

Tomographic reconstruction maps using the conventional two-sided summation method for EGF calculation. Areas with low path coverage have been masked.

---

For periods that are most sensitive to the upper crust ( $\leq 15$  s), the region within Hudson Bay appears as a conspicuous, low-velocity element of the tomographic reconstructions (Figure 2.11 and 2.12). In contrast, the Archean Superior craton, which has a horseshoe-like geometry that encloses the embayment in southeastern Hudson Bay (Figure 2.3), appears as a prominent high-velocity feature. The checkerboard reconstructions (Figure 2.10) confirm that these general features of the model are robust. For increasing periods above 15 s, the low-velocity anomaly within Hudson Bay increases in size, reaching a maximum area at 25 s, then shrinks in size but persists to a period up to about 35 s. This anomaly appears to take on an elongate shape with a generally north-south strike, although we observe that this apparent elongate shape may simply be an artefact of the path coverage in our data.

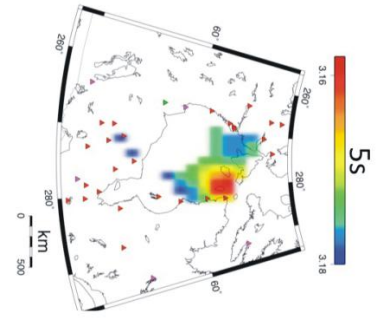
Figure 2.13 shows three pseudo-sections taken through the reconstructed tomographic model in Figure 2.12, corresponding to two-station paths across Hudson Bay. The first is east-west section from station FCC to INUQ; the second is a north-south cross-section from station QILN to KASO; and the third is a northwest-southeast profile from station YBKN to SNQN, passing through the centre of the Hudson Bay basin. Based on 1D

inversion results discussed below, the increase in velocity at the base of the pseudo-sections can be viewed as consistent with receiver-function derived crustal-thickness measurements around Hudson Bay (Thompson et al. 2010). This presentation of the tomographic model emphasizes the contrast between low-velocity crustal domains beneath Hudson Bay and the high-velocity Superior craton in the south. An interesting feature near the base of the QILN-KASO pseudo-section is an apparent uplift in high-velocity contours near the centre of Hudson Bay. This feature is considered in more detail below.

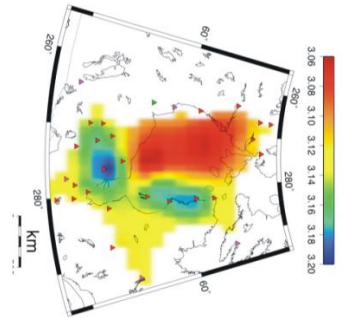
## **2.6 Discussion**

### *2.6.1 Directionality and seasonality*

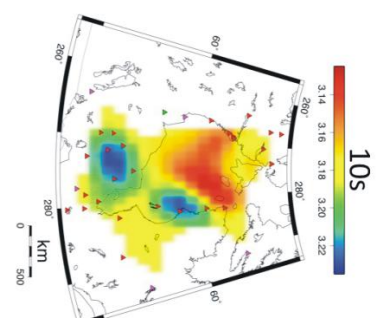
Rose diagrams showing azimuthal directions of ambient noise sources (Figure 2.5) indicate a strong influence from both the west coast (near southern Alaska) and the east coast (near the Labrador Sea). From quadrant to quadrant, a significant feature is a systematic change in direction consistent with a localised stationary noise source along both coasts. A less prominent northern noise source from the Arctic coast is evident in rose diagrams from the north and east quadrants of Hudson Bay. The diagrams show no apparent influence from Hudson Bay. This is particularly evident for quadrants on the north and south sides, which lack inward-pointing vectors (Figure 2.5), despite interstation paths for which both stations are on the same side of the Bay (e.g. stations STLN-SEDN north of the bay or KAPO-SILO on the south side).



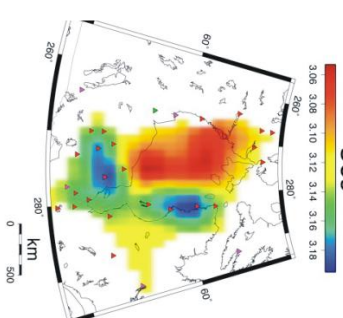
5S



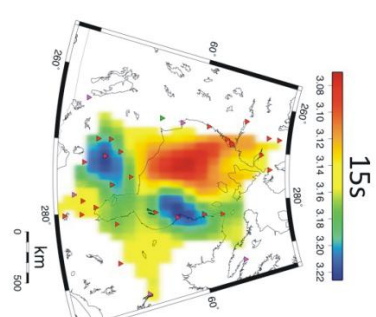
25S



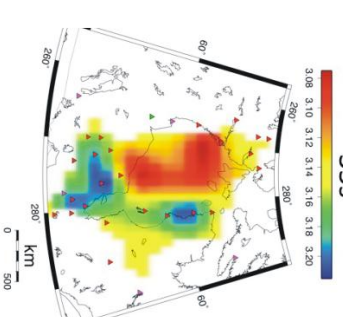
10S



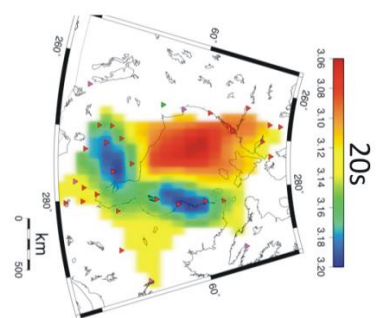
30S



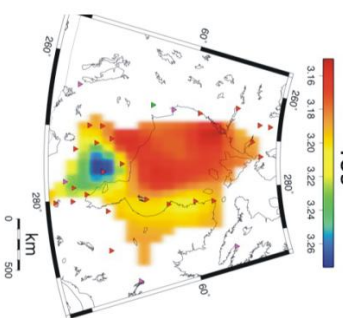
15S



35S



20S



40S

**Figure 2.12 One-sided empirical Green's Function EGF tomographic reconstruction.**

Same as in Figure 2.11, but for the one-sided SNR selection method for EGF calculation.

---

The disaggregation of rose plots by season and period (Figure 2.6) shows only a slight variation between summer and winter, but significant dependence on period. For example, the short-period (5 s) rose diagrams are characterised by dominant noise-source directions within narrow azimuthal apertures, mainly from the east coast, whereas the long-period (40 s) plots show a more diffuse pattern, with little azimuthal variability and seemingly stronger signals from the west coast. These characteristics are consistent with the interpretation that primary (10-20 s) and secondary (5-10 s) microseismic bands reflect acoustic-elastic coupling of ocean swells with the continental shelf. Although evidence for seasonal variability is subtle, several of the rose plots in Figure 2.6 show a slightly narrower azimuthal distribution of noise sources during the winter than in the summer, especially for the 5-s period.

Cornett and Zhang (2008) show that the mean wave power of coastal British Columbia is highest in the winter months (highest in December) and lowest in the summer months (namely, June and July). This study was done mainly for western Vancouver Island, near Ucluelet and Tofino, in an offshore study over a five-year period from October 2002 to September 2007. Similar data for the north Atlantic (Lozano and Swail, 2002) and Labrador Sea (Capon, 1973) are also consistent with the apparent slightly increased

influence of particular coastal regions (i.e., southern Alaska and Labrador) during the winter.

### *2.6.2 Velocity distributions*

Figure 2.14 shows velocity histograms at 20-s period for sub-regions encompassing the Archean Superior craton and the interior of Hudson Bay, respectively. Areas of low path coverage that are masked-off in Figures 2.10-2.12 have been excluded. For purposes of this calculation the circum-Superior belt (Eaton and Darbyshire, 2010), a Paleoproterozoic passive margin (Figure 2.3), is incorporated here as part of the Superior domain. The distributions show a significant separation; the mean and standard deviations are  $3.10 \pm 0.03$  km/s (Hudson Bay interior) and  $3.18 \pm 0.03$  km/s (Superior), respectively. This difference indicates that significant differences exist between these two regions of the Canadian Shield in terms of seismic velocity structure, likely to at least mid-crustal depth.

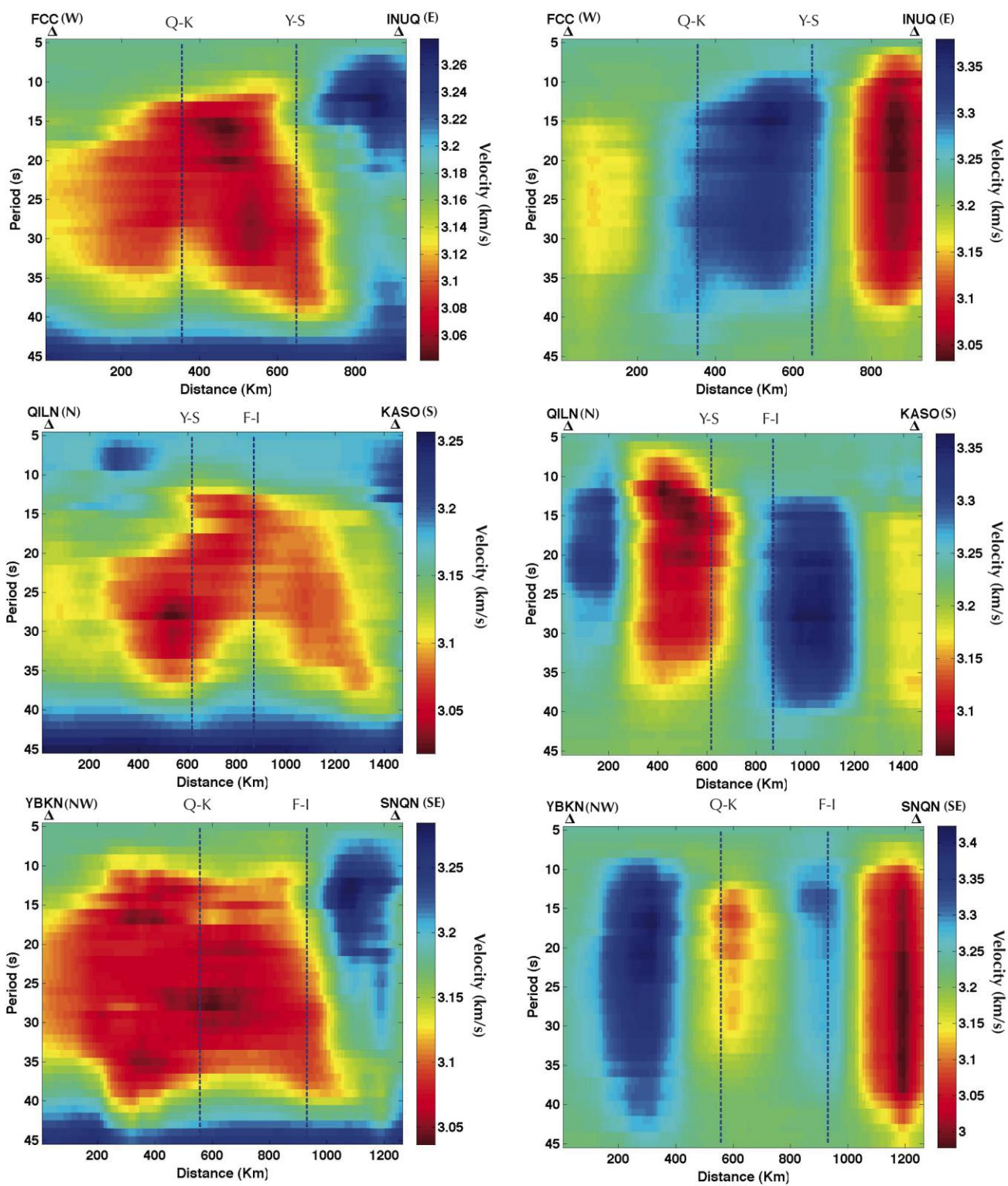


**Figure 2.13 Pseudo-sections.**

Pseudo-sections through the tomographic model (left column), compared with the checkerboard reconstruction (right column). Perfectly resolved features in the checkerboard reconstruction should appear as vertical columns. Vertical dashed lines indicate pseudo-section intercrossing location, where F-I means FCC-INUQ, Q-K means QILN-KASO and Y-S means YBKN-SNQN. Note apparent crustal thinning beneath the centre of Hudson Bay, best seen on QILN-KASO pseudo-section where it crosses with FCC-INUQ.

---

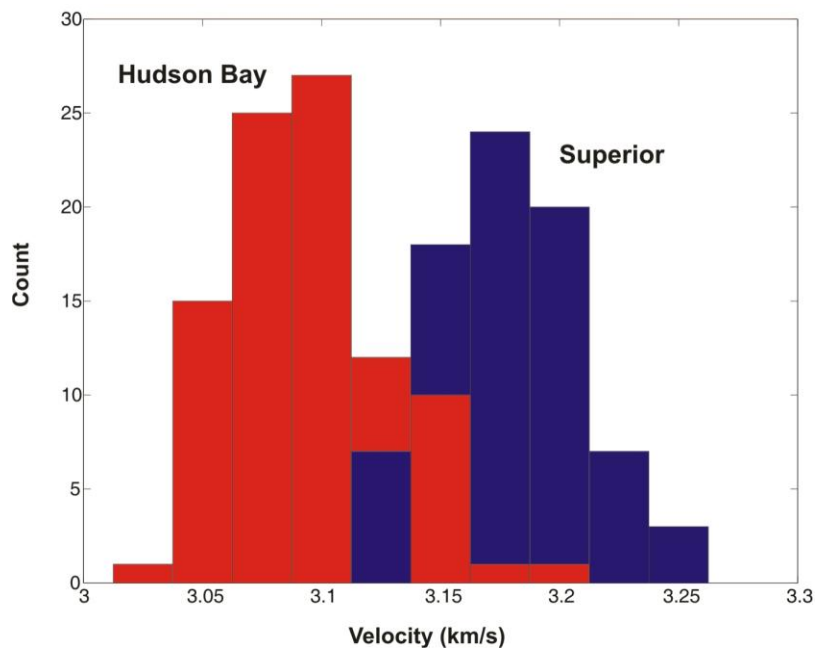
*2.6.3 Crustal thinning*

Figure 2.15 compares the tomographic inversion for 15s period with a map of lithospheric stretching factor ( $\beta$ ) obtained by Hanne et al. (2004), based on subsidence modelling of the Hudson Bay basin. Using a variant of the model of McKenzie (1978), in which thermal subsidence is initiated by lithospheric thinning, Hanne et al. (2004) matched the basin subsidence history using a relatively modest, laterally varying stretching factor. The spatial correlation between the region of maximum stretching and the lowest velocities beneath Hudson Bay is remarkable, whereas the outline of the low-velocity region cuts across several Precambrian tectonic domain boundaries (Figure 2.3). This suggests that the reduced mid-crustal velocities beneath Hudson Bay may be an expression of the early Paleozoic extension that occurred during basin formation, long after termination of the THO.

Based on their inferred lithospheric stretching model, Hanne et al. (2004) estimated crustal thinning by about 3 km beneath Hudson Bay. To examine how this degree of crustal thinning could be expressed in terms of fundamental-mode Rayleigh group velocity, we computed theoretical dispersion curves for two simple 1D crustal models (Figure 2.16). Each two-layer model comprises a uniform crust with  $V_p = 6.0$  km/s,  $V_s = 3.5$  km/s and  $\rho = 2.8$  Mg/m<sup>3</sup>, underlain by a mantle layer with  $V_p = 8.0$  km/s,  $V_s = 4.7$  km/s and  $\rho = 3.3$  Mg/m<sup>3</sup>. The models differ only in crustal thickness, which are 38 km and 35 km, respectively. With the exception of a more prominent local minimum, the overall shape of the computed dispersion curves resembles observed dispersion trends (e.g., Figure 2.7). The computed difference between the thin- and average-crustal model (Figure 2.16, right) reaches a maximum of about 0.15 km/s at a period of about 34s. Given the smoothing that is inherent to the tomographic inversion process, this is consistent with our tomographic results (Figure 2.13), which reveal a similar (but slightly reduced) velocity difference between the centre of Hudson Bay and the periphery. Although not unique, our inversion results are consistent with crustal thinning by about 3 km as suggested by Hanne et al. (2004) beneath Hudson Bay. On the other hand, the hypothesis that basin formation was triggered by eclogitisation of a thick crustal root (Fowler and Nisbet, 1985) is not easily reconciled with our results. Since eclogitisation rarely transforms all of the lower-crustal material (Bjornerud et al., 2002), this scenario predicts preservation of a relict crustal root, which would have an expression opposite to the inferred crustal thinning suggested by our tomographic images.

#### *2.6.4 Depth Inversion*

Results of 1D inversions are shown in Figure 2.17, for four station pairs. MALO-KASO is located entirely south of Hudson Bay and does not cross Hudson Bay; SILO-SEDN crosses Hudson Bay with a north-south path; INUQ-FCC crosses the Bay with an east-west path (a pseudo-section for INUQ-FCC is shown in Figure 2.13), and FRB-FCC crosses Hudson Bay with a northeast-southwest path (refer to Figure 2.1 for station locations). The inversion results can be viewed as representative of models that fit the path-averaged dispersion data between pairs of stations.



**Figure 2.14 Velocity distribution.**

Velocity histograms at 20-s period for well-sampled sub-regions within Hudson Bay and the Archean Superior province, including the adjacent circum-Superior belt (a Paleoproterozoic passive margin). The bars are arranged so that the smaller one is in the foreground.

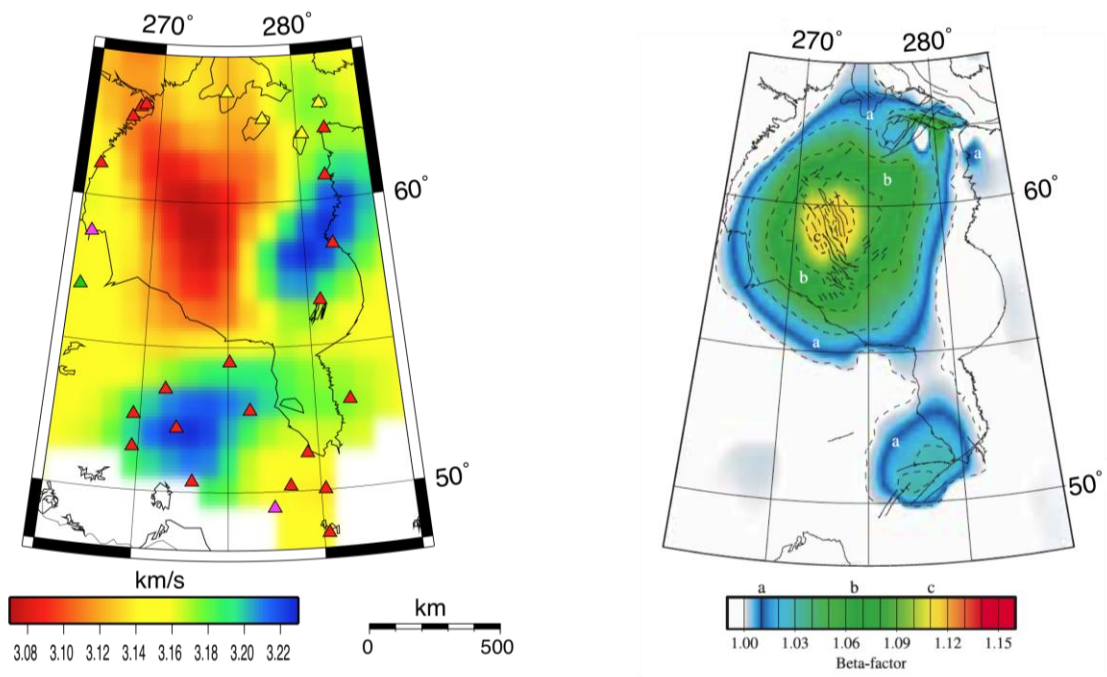


**Figure 2.15 Comparison with lithospheric stretching factor diagram.**

A comparison of tomographic inversion result for 15s period (left), representative of the mid-crust, with the lithospheric stretching factor ( $\beta$ ) for the Hudson Bay basin (Hanne et al. 2004).

In each subplot of Figure 2.17, the dashed line shows the linearised inversion result from stage 1. Light gray curves show acceptable models derived from this in stage two, where a Monte Carlo scheme is employed to perturb the model. The solid black curve is an average of these perturbed models. Although details of the 1D inversion models vary, all confirm that the ambient-noise dispersion data are generally consistent with independent constraints on crustal thickness and velocity structure (Darbyshire and Eaton, 2010; Thompson et al., 2010). Though the interstation paths used to construct the 1D profiles in Figure 2.17 are too long to yield detailed constraints on the crustal structure beneath Hudson Bay, it is reassuring to note that the data can be fit using plausible crustal structures obtained via receiver function analysis (Thompson et al., 2010) and Rayleigh wave dispersion (Darbyshire and Eaton, 2010).

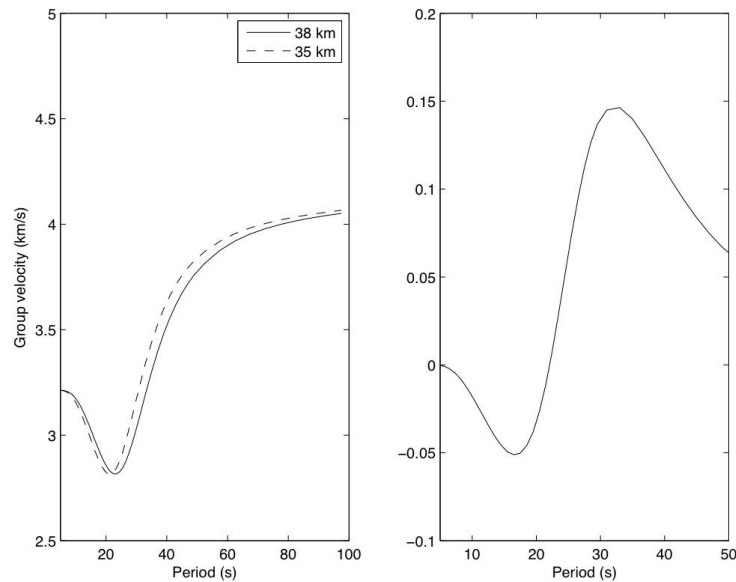


**Figure 2.16 Crustal thinning model.**

Theoretical group-velocity dispersion curves for a simple two-layer model with crustal velocities  $V_p = 6.0$  km/s and  $V_s = 3.5$  km/s, underlain by a mantle with velocities  $V_p = 8.0$  km/s and  $V_s = 4.7$  km/s. The density of the crust is  $2.8$  g/cm<sup>3</sup> and the mantle is  $3.3$  g/cm<sup>3</sup>. The graph on the left compares theoretical group velocity curves for crustal thickness of 35 and 38 km. The graph on the right shows the difference (thin – thick crust), showing a maximum group velocity difference of 0.15 km/s between 35 s and 40 s period. Compare with Figure 2.14.

In order to further assess the implications of our tomographic results for crustal thickness, we considered apparent dispersion curves extracted from our tomographic model at the locations labelled Y-S and F-I from the QILN-KASO pseudo-section in Figure 2.13. Location F-I is situated in the centre of Hudson Bay where the crust appears to thin based on the tomographic results (Figure 2.13), whereas location Y-S is situated in the northwest part of our study area where the Moho appears to be deeper. Differences between the two apparent dispersion curves are most pronounced in the period band from 25-35 s. Using the inversion approach described in section 3.3, we obtained average 1D shear-wave velocity profiles (Figure 2.18). Clear velocity differences are evident between depths of 30 and 40 km, whereas for other depths the profiles are relatively similar. Using the point where  $V_s$  exceeds 4.0 km/s as a proxy for crustal thickness in these inverted models, the inferred Moho depth changes from  $\sim 40$  km at location F-I to  $\sim 43$  km at location Y-S. While a full 3-D inversion is required to obtain well-constrained absolute depth estimates, these results imply that differences in the tomographic results between these locations can be reasonably explained by a crustal thickness difference of about 3 km.

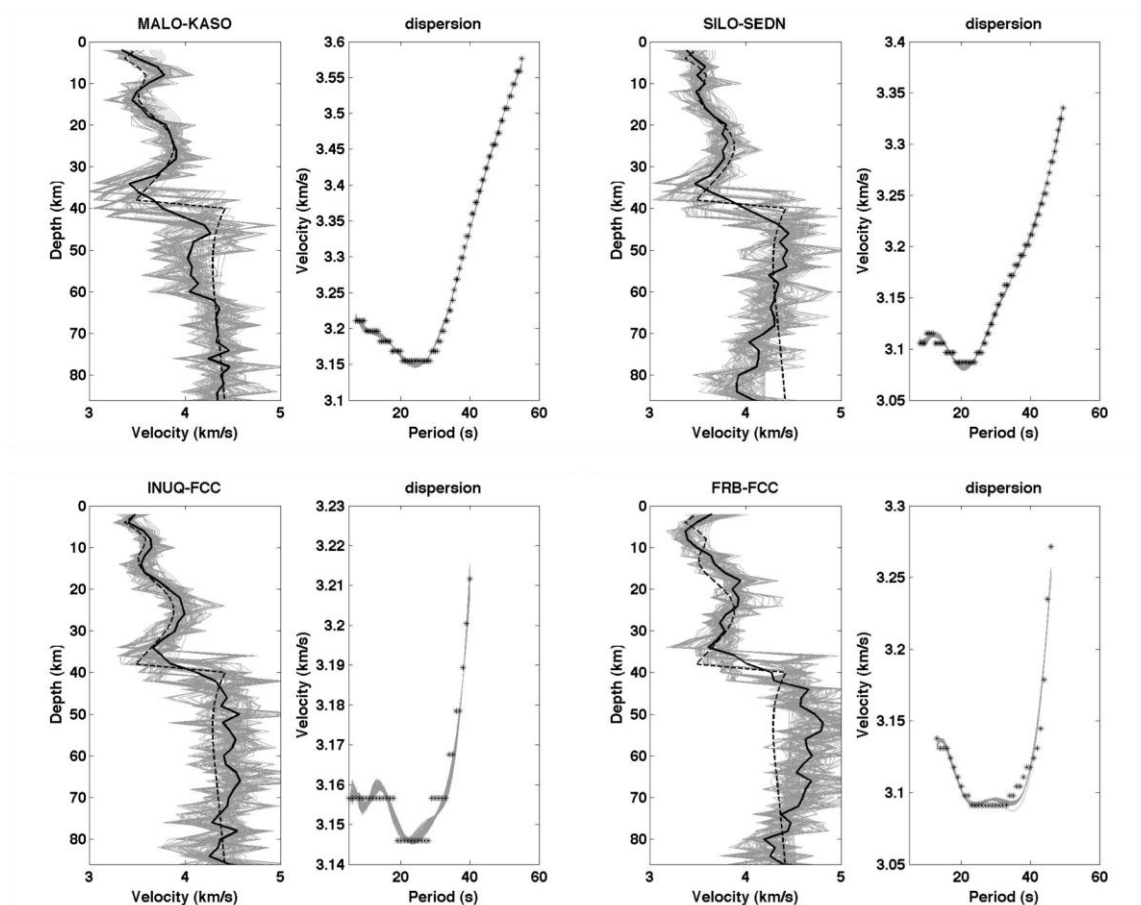


**Figure 2.17 1D depth inversions.**

Shear-wave velocity profiles from 1D depth inversion for 4 different station pairs, crossing the bay in various directions (MALO-KASO, SILO-SEDN, INUQ-FCC, and FRB-FCC, see Figure 2.1 for station locations). Dashed line indicates starting model, gray lines indicate individual acceptable model solutions and the black line is an average of the acceptable models.

## 2.7 Conclusions

Ambient-noise processing applied to 21 months of continuous recording at 37 stations around Hudson Bay has yields 591 cross-correlograms with coherent signals to a distance of  $> 2200$  km. The signals extracted are dominated by fundamental-mode Rayleigh waves, which are most prominently expressed within certain preferred azimuths indicative of stationary coastal noise sources near southern Alaska and Labrador. In contrast to the expected symmetry of cross-correlation functions that should emerge from a diffuse velocity field, virtually all of the cross-correlograms obtained in this study are conspicuously asymmetric. We have tested and implemented a one-sided approach to group-velocity dispersion analysis that is based on signal-to-noise (SNR) selection of the optimum side (causal or acausal) of the cross-correlogram. We prefer this approach to standard two-sided averaging because it tends to produce better-defined dispersion ridges in time-frequency plots.

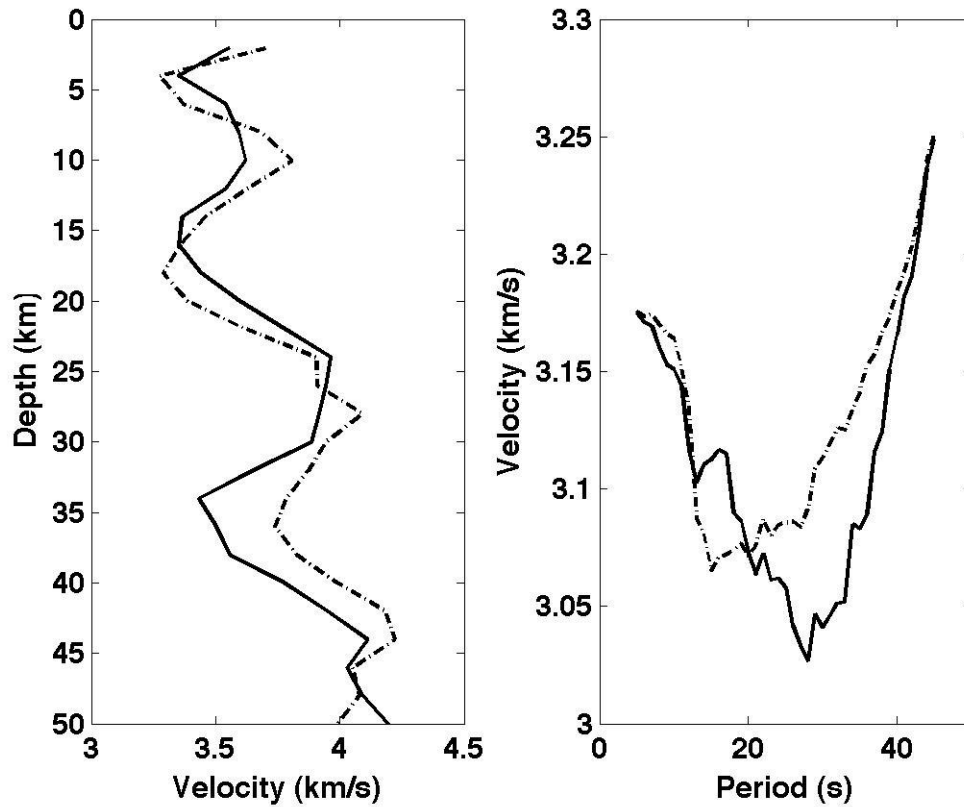


**Figure 2.18 1D depth inversion showing crustal thinning.**

Shear-wave velocity profiles from 1D depth inversion (left panel) for apparent dispersion curves (right panel) taken from QILN-KASO pseudo-section in Figure 2.13. Solid lines correspond to the dispersion curve at Y-S intersection and dashed line corresponds to dispersion curve at F-I intersection.

In the period range 5-40 s, which is sensitive to the entire crust, our tomographic inversion results feature a prominent low-velocity region beneath Hudson Bay. This region is bounded to the south and east by a region of high crustal velocities within the Archean Superior craton and its contiguous Paleoproterozoic passive margin. At 20s period, at which the tomographic images have the best path coverage based on SNR analysis of the cross-correlograms, velocities in these two regions differ significantly ( $3.10 \pm 0.03$  km/s within Hudson Bay versus  $3.18 \pm 0.03$  km/s in the Superior). The region of lowest velocity cross-cuts Precambrian tectonic boundaries but corresponds remarkably well with the areal pattern of lithospheric stretching inferred by Hanne et al. (2004). Our tomographic results are consistent with the amount of crustal thinning (about 3 km) inferred by Hanne et al. (2004) on the basis of subsidence modelling, but are not consistent with the hypothesis that subsidence of Hudson Bay was triggered by eclogitisation of a crustal root that formed during the Trans-Hudson orogeny (Eaton and Darbyshire, 2010).

Chapter Three: **CRUSTAL ANISOTROPY BENEATH HUDSON BAY FROM  
AMBIENT-NOISE TOMOGRAPHY: EVIDENCE FOR POST-OROGENIC  
LOWER-CRUSTAL FLOW?**

**Summary**

The crust underlying Hudson Bay, Canada records a long and complex tectonic history. In this study, we investigate this region using tomographic inversion based on continuous ambient-noise recordings from 37 broadband seismograph stations that encircle Hudson Bay. The ambient-noise data were processed to obtain group-velocity dispersion measurements from 10 – 35s period, which were inverted using an algorithm that incorporates the effects of anisotropy. This work is among the first in which ambient-noise data have been used to investigate azimuthal anisotropy. The inversion method uses smoothing and damping to regularize the solution; due to the significantly increased number of model parameters relative to the isotropic case, we performed a careful analysis for parameter selection to determine whether "leakage" occurs between isotropic and anisotropic model parameters. We observe a robust pattern of anisotropic fast

directions in the mid-crust that are consistent with large-scale tectonic trends based on magnetic-anomaly patterns. In particular, a distinctive double-indentor shape for the Superior craton is clearly expressed in both datasets. This pattern breaks down deeper in the crust, suggesting that some degree of lithospheric decoupling in the lower crust, such as channel flow, occurred during orogenesis. Given regional evidence for vertically coherent deformation in the crust and underlying mantle, we interpret this pattern in the lower crust as a tectonic overprint that post-dates the main phase of Trans-Hudson deformation. At most levels in the crust, we observe a profound change in direction of anisotropic fast direction across an inferred suture beneath Hudson Bay.

### **3.1 Introduction**

Hudson Bay is a shallow inland sea that overlies the Paleozoic Hudson Bay basin, an intracratonic basin with stratigraphic record similar to the hydrocarbon-rich Williston, Illinois and Michigan basins (Figure 3.1). The Precambrian basement underlying the Hudson Bay basin was assembled by continental collisions culminating in the ca. 1.8 Ga Trans-Hudson Orogen (THO; Hoffman, 1990; Bickford et al., 1990; Corrigan et al., 2005; Eaton and Darbyshire, 2010). Teleseismic studies of mantle anisotropy have shown that upper-mantle anisotropic fabrics delineate many of the geologically inferred lithospheric sub-divisions to the north of Hudson Bay (e.g., Bastow et al., 2011). Similar analysis farther south beneath the Bay has not been possible to date, however, because of the absence of ocean-bottom seismometers to record body-wave phases such as SKS. Therefore, whether the THO and/or earlier collisional events are preserved as fossil fabrics beneath the Bay remains unclear. Furthermore, loading by the Laurentide ice-

sheet, subsequent on-going postglacial rebound and regional stresses induced by other sources may also manifest as measurable seismic anisotropic fabrics beneath the Bay. To address these issues, we investigate crustal anisotropy and seismic-velocity structure using ambient-noise tomography (or seismic interferometry), using 21 months of continuous data acquired at 37 broadband seismograph stations located around the periphery of Hudson Bay (Figure 3.1a). This study builds on earlier work (Pawlak et al., 2011) in which the isotropic seismic structure of the crust and upper mantle beneath Hudson Bay was imaged using the method of Bensen et al. (2007). Although ambient-noise tomography has been widely used in recent years (e.g., Shapiro et al., 2005; Curtis et al., 2006; Yao et al., 2006; Yang et al., 2007; Moschetti et al., 2007; Lin et al., 2007, 2011), incorporating azimuthal anisotropy has only recently started to emerge (Yao and van der Hilst, 2009; Fry et al., 2010; Gallego et al., 2011; Lin et al., 2011).

Our investigation uses continuous recordings of ground motion from broadband seismograph stations deployed as part of the Hudson Bay Lithospheric Experiment (HuBLE), an international initiative with the broad aim of elucidating the lithospheric architecture beneath the Bay. To date, HuBLE data have been used to study various features and depth ranges, including receiver-function analysis of crustal structure (Thompson et al., 2010) and mantle transition zone thickness (Thompson et al., 2011), isotropic ambient-noise tomography to investigate basin structure (Pawlak et al., 2011), SKS-splitting investigation of upper-mantle anisotropy (Bastow et al., 2011) and surface-wave studies of the lithospheric keel (Darbyshire and Eaton, 2010).

After providing an overview of the isotropic ambient-noise processing procedure, we introduce an anisotropic tomography method that has been previously applied for the inversion of teleseismic surface-wave measurements and for array tomography using earthquake signals (Lebedev and van der Hilst, 2008; Deschamps et al., 2008; Darbyshire and Lebedev, 2009). Following this, we present the results of anisotropic tomography together with a comprehensive analysis of parameter selection for the inversion process. Finally, we interpret the inferred anisotropic fabric by comparing our results with stress data, plate-motion directions and regional total-field magnetic anomaly data. Our results indicate that contrasting mid-crustal anisotropic fabrics are juxtaposed across the principal lithospheric suture within the THO, suggesting that these fabrics were formed prior to terminal collision.

### **3.2 Tectonic Setting**

Hudson Bay is a shallow (~100 m deep) epeiric sea, approximately 1000 km in diameter that formed by marine inundation of the continental interior following Laurentide ice-sheet deglaciation (Lee, 1968). The Bay is located near the center of the North American continent (Figure 3.1b), and the underlying crust preserves a record of Paleoproterozoic collisional assembly of Laurentia and subsequent formation of the Hudson Bay basin, with minor intraplate deformation coeval with the Cretaceous opening of Baffin Bay (Burden and Langille, 1990; Eaton and Darbyshire, 2010). With an area of ~833,000 km<sup>2</sup> and a maximum preserved stratigraphic thickness of ~2 km, the Hudson Bay basin is slightly more extensive but shallower than comparable intracratonic basins in North America (Michigan, Williston, Illinois).

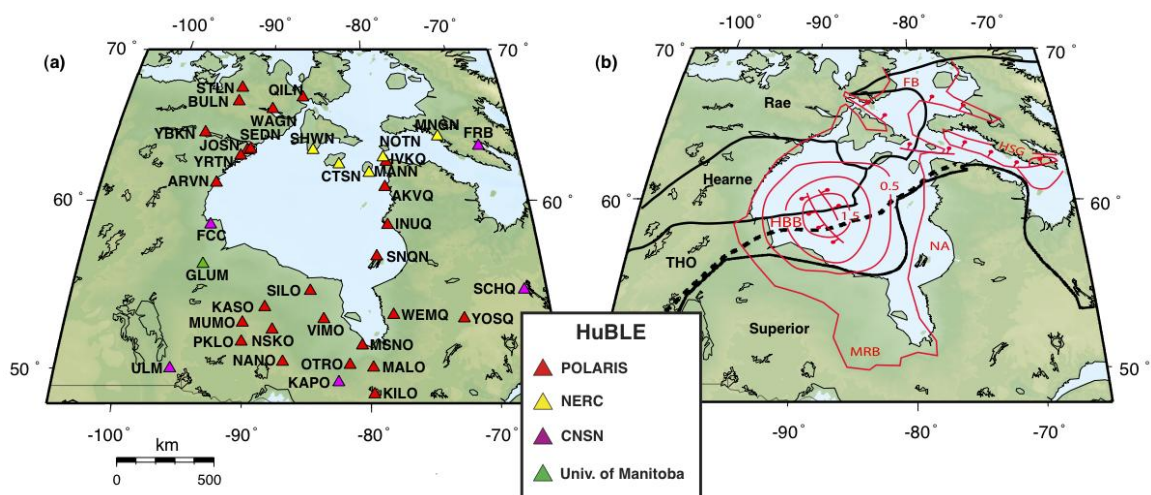


**Figure 3.1 Seismograph station map and generalized geology map**

(a) Map of Hudson Bay showing all HuBLE stations used in this study. (b) Tectonic map of Hudson Bay. Solid black lines are approximate locations of tectonic boundaries and the dashed black line represents the suture zone. The red lines outline the location of the Hudson Bay basin, mapped faults and total sediment isopach contours in kilometers. Abbreviations are as follows: THO, Trans-Hudson orogen; FB, Foxe basin; HSG, Hudson Strait graben; HBB, Hudson Bay basin; NA, Nastapoka Arc; MRB, Moose River basin (After Eaton and Darbyshire, 2010).

Beneath the Hudson Bay basin, the Precambrian basement is comprised mainly of the ca. 1.91-1.81 Ga THO and bounding Archean cratons (Figure 3.1b), including the Superior Province to the south and east and the Churchill Plates (Hearne and Rae Domains) to the north and west. Similar in spatial and temporal scales to the modern Himalayan-Karakoram-Tibetan orogeny (St-Onge et al., 2006), the THO formed as a result of collision between the Superior and Churchill protocontinents (Eaton and Darbyshire, 2010). Paleomagnetic evidence suggests that these two large Archean cratons were once separated by a Pacific-scale ocean (Manikewan Ocean; Symons and Harris, 2005), the closure of which is manifested by a suture that extends across Hudson Bay (Figure 3.1b – Eaton and Darbyshire, 2010). Continental arc formation due to pre-collision convergence and ocean-basin closure is represented by the giant Wathamun-Chipewyan batholith. Where exposed adjacent to Hudson Bay, the THO contains both juvenile supracrustal domains as well as blocks of pre 1.91 Ga crust, such as the Archean Sask craton (Hajnal et al., 2005). The lithospheric mantle beneath Hudson Bay has high shear velocity and is estimated to be at least 200 km in thickness, characteristics that are typical of Archean mantle keels (Darbyshire and Eaton, 2010). It has been suggested that the broad, shallow character of the Hudson Bay basin relative to other intracratonic basins may be due to the relatively stiff flexural rigidity of the lithospheric keel at the time of basin formation (Eaton and Darbyshire, 2010).

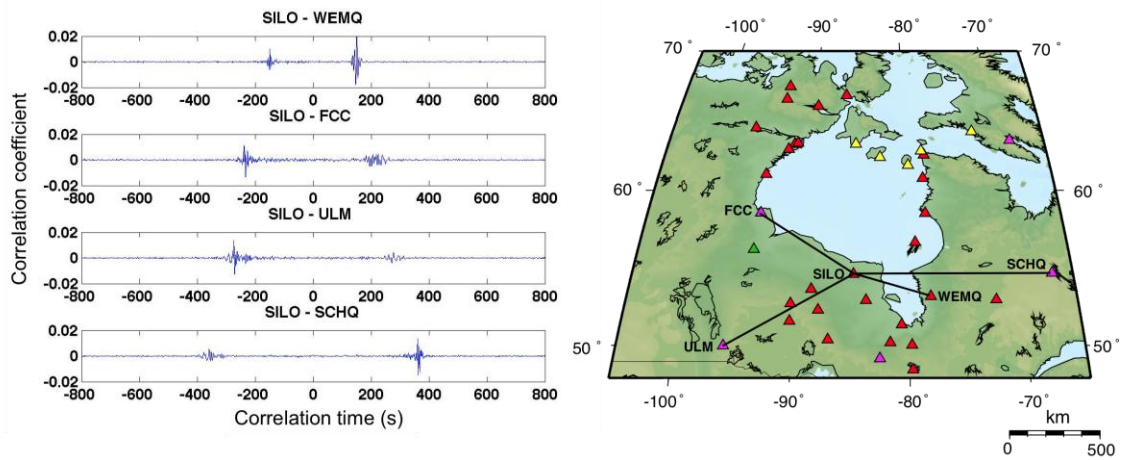


**Figure 3.2 Example of cross-correlation and noise asymmetry.**

Examples of four cross-correlations (left) illustrating asymmetry in correlograms with respect to signal-to-noise ratio (SNR), typical of this dataset. Corresponding paths are shown on the right. Station order represents direction of wave propagation, i.e. for SILO – WEMQ, the negative lag represents wave propagation from SILO to WEMQ and the positive lag represents wave propagation from WEMQ to SILO.

### 3.3 Data And Processing Methods

The data used for the present study were recorded at a sampling rate of 40 Hz over 21 months, from September 2006 to May 2008. Initial data-processing procedures follow the method of Bensen et al. (2007). First, the continuous vertical-component recordings were cut into individual one-day records and resampled to 1Hz. Next, daily trends, means and instrument-response functions were removed. Earthquake signals and instrument irregularities that could obstruct the signals of interest were suppressed using a one-bit time-normalization procedure. Finally, spectral whitening and bandpass filtering between 0.005 Hz and 0.3 Hz (200 s to 3.33 s period) were applied. Initial data-processing procedures are detailed further by Pawlak et al. (2011).

After completion of initial processing, correlograms were computed for all possible station pairs using available daily records. For each station pair, stacking of the daily cross-correlated signals yields a band-limited estimate of the inter-station Green's function (Bensen et al., 2007) containing both causal and acausal components (Figure 3.2). For the vertical-component data in this study, emergent signals are dominated by fundamental-mode Rayleigh waves with periods of ~10-30 s that originate at coastal areas around North America (Pawlak et al., 2011). Based on visual inspection of the stacked correlograms, of 666 available station pairs, 591 were found to be usable.

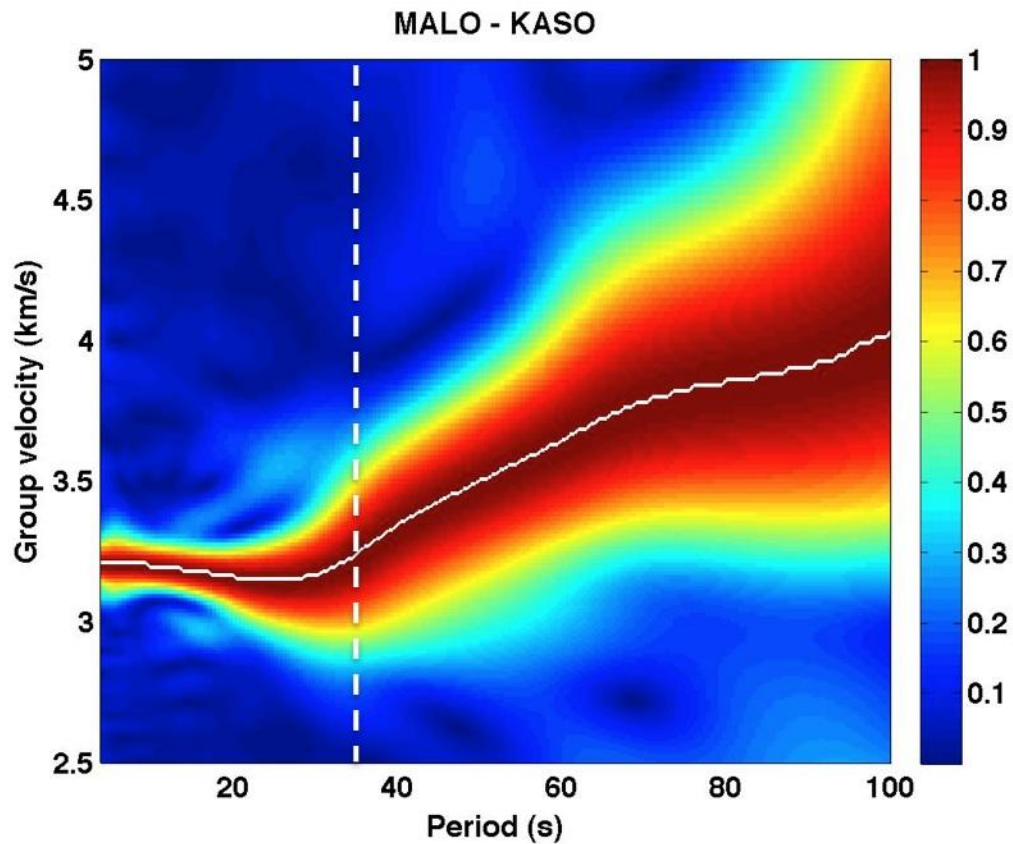


**Figure 3.3 Example time-frequency plot and dispersion analysis.**

The color scale shows the amplitude envelope, normalized for each period value. The solid white line represents the group-velocity dispersion curve used as input for the inversion procedure. The dashed white line shows an approximate boundary between periods at which group-velocities are sensitive primarily to the crust (left of the line) and primarily to the mantle (right of the line).

Figure 3.2 shows a representative example of a stacked correlogram showing both causal and acausal components of the Green's function. This example exhibits a pronounced asymmetry in which one half of the Green's function is characterized by a conspicuously higher signal-to-noise ratio (SNR) than the other half. This asymmetry originates from an inferred non-uniform distribution of coastal source locations (Pawlak et al., 2011). Since this asymmetry characterizes most of our data, instead of the typical approach (e.g. Bensen et al., 2007) of averaging both sides to obtain a one-sided empirical Green's function (EGF), here we select for further processing the side of the correlogram having higher SNR (Pawlak et al., 2011). Choosing the higher SNR yields better dispersion ridges in our data compared with the averaging method (Pawlak et al., 2011). We remark that determination of group velocity in this manner is compatible with anisotropic models for the crust that are considered below, since all models exhibit identical wavespeed in opposite directions (i.e. periodicity of  $\pi$  radians).

The EGFs derived in this fashion were then used for estimating group velocities based on time-frequency analysis (Figure 3.3). In our implementation of this procedure, the time-frequency plot is constructed for a given central frequency by applying a narrow-band filter to the EGF and then computing the amplitude envelope (Pawlak et al., 2011). Group velocity is obtained as a function of period by tracking the maximum amplitude such that a continuous dispersion curve is obtained. The shape of the dispersion curve is strongly influenced by the thickness of the crust and shows a clear transition from low velocity in the crust to high velocity in the underlying mantle (Figure 3.3). The group-velocity estimates are used as the basis for tomographic inversions that solve for period-specific

models of the fundamental-mode Rayleigh-wave group velocity and azimuthal anisotropy beneath Hudson Bay.

### 3.4 Inversion

We use a tomographic inversion scheme that has been used in analysis of interstation phase-velocity measurements made with teleseismic surface waves (Deschamps et al., 2008; Darbyshire and Lebedev, 2009; Endrun et al., 2011). We remark that, within the usable bandwidth of the data (generally  $\sim 10\text{--}35$  s period for most EGFs in our dataset), the raypath coverage afforded by ambient-noise measurements (Figure 3.4a) is well suited to anisotropic analysis because it contains nearly the full range of two-station azimuths possible for any given station distribution. The first step is to subtract the mean value of group velocity from all measurements, at each period. For the  $i$ th station pair, this yields a residual inter-station average group velocity,  $\delta U_i(\omega) \pm \Delta U_i(\omega)$ , where  $\Delta U_i$  is the measurement uncertainty (estimated here to be 0.1 km/s). Working at Earth's surface within a spherical co-ordinate system defined by  $\theta$ ,  $\phi$  (Figure 4.3b),  $\delta U_i(\omega)$  can be expressed in terms of the group-velocity model perturbations  $\delta U(\omega, \theta, \phi)$  as

$$\int_{q} \int_{f} K_i(q, f) dU(\omega, q, f) df dq = \delta U_i(\omega) \quad , \quad (3.1)$$

where  $\omega$  is angular frequency and  $K_i$  defines a sensitivity function for the  $i$ th station pair. Following Darbyshire and Lebedev (2009), the sensitivity function is defined here by rays along inter-station great-circle paths (finite-width rays can also be easily accommodated within this formalism). To account for the effects of weak Rayleigh-wave

anisotropy, the group-velocity perturbations  $\delta U(\omega, \theta, \phi)$  are parameterized using 5 unknowns (Smith and Dahlen, 1973):

$$dU(\omega) = dU_{iso}(\omega) + A_1(\omega)\cos(2\Psi) + A_2(\omega)\sin(2\Psi) + A_3(\omega)\cos(4\Psi) + A_4(\omega)\sin(4\Psi) \quad , \quad (3.2)$$

where  $\delta U_{iso}$  is the isotropic group-velocity perturbation and  $\Psi$  denotes the wave-propagation azimuth with respect to geographic north. Terms that depend on  $2\Psi$  and  $4\Psi$  in Equation 3.2 account for azimuthal variations of group velocity that exhibit a periodicity of  $\pi$  and  $\pi/2$  radians, respectively.

The 5 model parameters in Equation 3.2 are computed on a coarse (200 km) triangular model grid (Figure 3.4b), where the knot-point locations are determined using the method of Wang and Dahlen (1995). The integration used to construct Equation 3.1 is performed using a dense (40 km) integration grid of knot points (Figure 3.4b). For every integration knot, a hexagonal region centered on the knot point is considered, whose vertices are made up of the six nearest points. The integration weight is first calculated at each of the integration-grid knot points located within one inter-knot distance from the interstation great-circle path and is proportional to the area of the hexagon around it. The weights  $K$  for the model parameters at model grid knots are then computed as integrals over the neighboring integration-grid knots (Lebedev and van der Hilst, 2008).

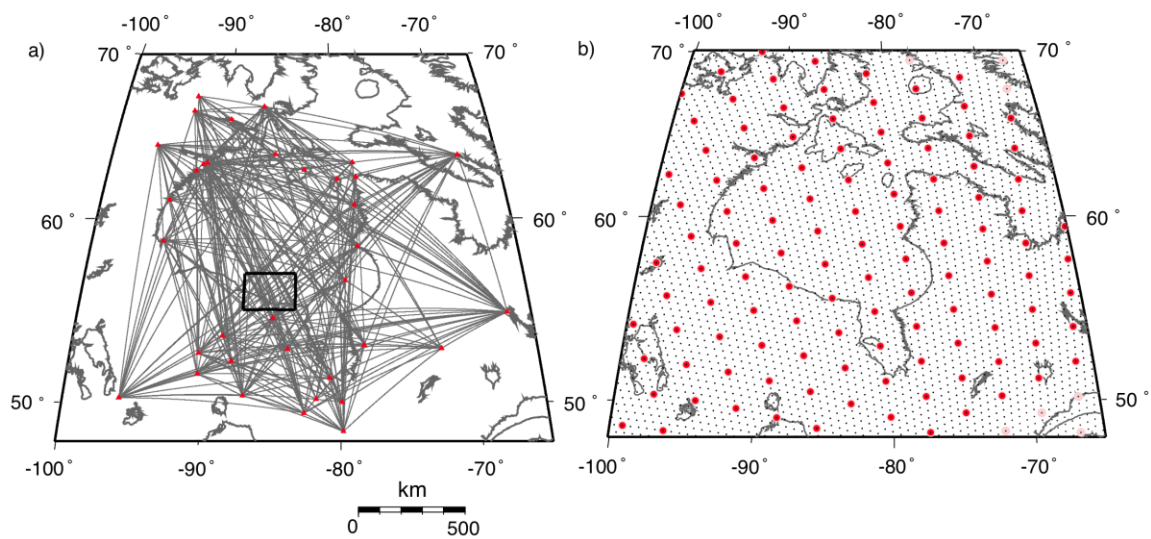


**Figure 3.4 Path density and grid knot maps.**

(a) Path density diagram. Black box shows paths used in Figure 3.6. (b) Map showing model-grid (red circles) and integration-grid (black circles) knots.

At each of the 6 selected periods (10, 15, 20, 25, 30, 35 s), a sparse system of linear equations was constructed using Equations 3.1 and 3.2 for all available paths. The resulting system was then solved iteratively using LSQR (Paige and Saunders, 1982), with smoothing and gradient damping. Gradient damping is a type of regularization that penalizes the difference between anomalies at each pair of neighboring knot points. This is similar to damping the first spatial derivative of the distributions of seismic velocity and anisotropy. Model smoothing is based on the difference between the anomaly at a grid knot and an average over anomalies at this and all neighboring knots. This second kind of smoothing is similar to damping the second spatial derivatives. The smoothing and damping parameters are assigned independently for  $\delta U_{iso}$  and the 4 anisotropic parameters, and their selection plays a critical role in the inversion. Testing and selection of the smoothing and damping parameters is described in detail in Appendix A.

At this stage, we consider a number of simple scenarios to illustrate how  $2\Psi$  and  $4\Psi$  symmetry might relate to fracture systems and/or alignment of intrinsically anisotropic minerals in the continental crust. In evaluating these scenarios, we invoke Neumann's principle (Winterstein, 1990) to relate the symmetry properties of the medium to the corresponding symmetry of wave propagation in the medium. For example, a single set of vertical cracks or sheet-like intrusions (dykes) in an otherwise isotropic medium would give rise to an azimuthally anisotropic system that exhibits  $2\Psi$  symmetry for horizontally propagating Rayleigh waves (Figure 3.5a). In this scenario, the plane of the cracks (dykes) is expected to be perpendicular to the minimum principal stress direction at the

time of formation (Crampin, 1994). Crampin (1987) has proposed a more general crustal model, referred to as extensive-dilatancy anisotropy, in which pore spaces deform in response to the ambient stress field in a manner that would exhibit the same symmetry behavior as this crack model. Alternatively, azimuthal anisotropy could result from a pervasive metamorphic fabric that produces a strong crystallographic preferred orientation (Figure 3.5b). This could occur for a single dominant, near-vertical foliation or near-horizontal lineation fabric that is expressed by strongly anisotropic minerals such as mica and amphibole (Meltzer and Christensen, 2001; Mahan, 2006). Such rock fabrics are commonly observed in metamorphic terranes around Hudson Bay (Lee, 1968). Moreover, laboratory studies of metamorphic rocks (Brocher and Christensen, 1990) and seismological observations of the continental crust (e.g., Paulssen, 2004; Shapiro et al., 2004; Moschetti et al., 2010; Endrun et al., 2011; Lin et al., 2011) have documented strong azimuthal and radial anisotropy in various tectonic settings.

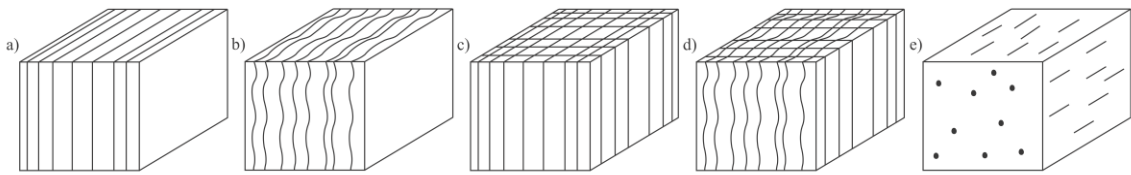


**Figure 3.5 Schematic of geologic scenarios.**

Schematic representation of: a) vertical cracks; b) metamorphic foliation; c) mutually perpendicular vertical cracks; d) metamorphic foliation with perpendicular vertical cracks; e) lattice preferred orientation (LPO) of orthorhombic minerals.

Similarly, a  $90^\circ$  periodicity in Rayleigh-wave group velocity implied by the  $4\Psi$  symmetry could be produced by several common geologic scenarios. For example, two sets of mutually perpendicular vertical cracks (Figure 3.5c) would yield an orthorhombic anisotropic system (Winterstein, 1992) with  $4\Psi$  symmetry. Perpendicular crack systems (or pairsets as termed by Gay (1973)) are commonly observed in crustal rocks. The pairsets are believed to have formed simultaneously due to vertical motion or vertically directed forces and are perpetuated through cycles of regional metamorphism (Gay, 1973). A second possibility is a single set of vertical cracks within a transversely isotropic medium, such as crustal rocks with a strong crystallographic preferred orientation as described above (Figure 3.5d). Finally, a well-developed crystallographic preferred orientation caused by alignment of minerals that exhibit orthorhombic seismic anisotropy (Figure 3.5e) (Barruol and Mainprice, 1993; Mandeville, 2010), could give rise to  $4\Psi$  symmetry. Such a scenario is commonly invoked to explain seismic anisotropy of the upper mantle due to crystallographic preferred orientation of olivine (Zhang and Karato, 1995; Smith et al., 2004).

Given the possible geologic scenarios commonly seen in the crust, our dataset was analyzed to evaluate the relative contribution of  $2\Psi$  and/or  $4\Psi$  variations. A selection of data taken from an area of dense path coverage (this region is shown by the black box in Figure 3.4a) at the 20 s period is shown in Figure 3.6. The 20 s period is used here because it has the most data and densest path coverage. An L1 norm was used to find a best fit to our data points, as an L1 norm is robust to outliers unlike the L2 norm (Drulea et al., 2010). The solid black line represents the L1 norm best fit for  $2\Psi$  variations and the

dashed black line is the L1 norm best fit for  $4\Psi$  variation. The red line is the L1 best fit to the data, and the sum of the  $2\Psi$  and  $4\Psi$  variations. This dataset (Figure 3.6), which is representative of data where path coverage exhibits a good azimuthal distribution (Figure 4.3a), shows a clear dominance of the  $2\Psi$  signal; henceforth, for simplicity, we limit our interpretations to the  $2\Psi$  case. However, this does not necessarily mean that  $4\Psi$  anisotropy does not exist in the crust here, but that it perhaps simply may not be resolved by our data. Invoking Neumann's principle, we omit from further consideration models defined by a  $4\Psi$  symmetry system (i.e. Figures 3.5c, d, and e). We envision that there could be a "pseudo  $2\Psi$ " model, similar to scenarios seen in Figure 3.5 c and d, where one of the fracture or foliation systems is dominant over the other.

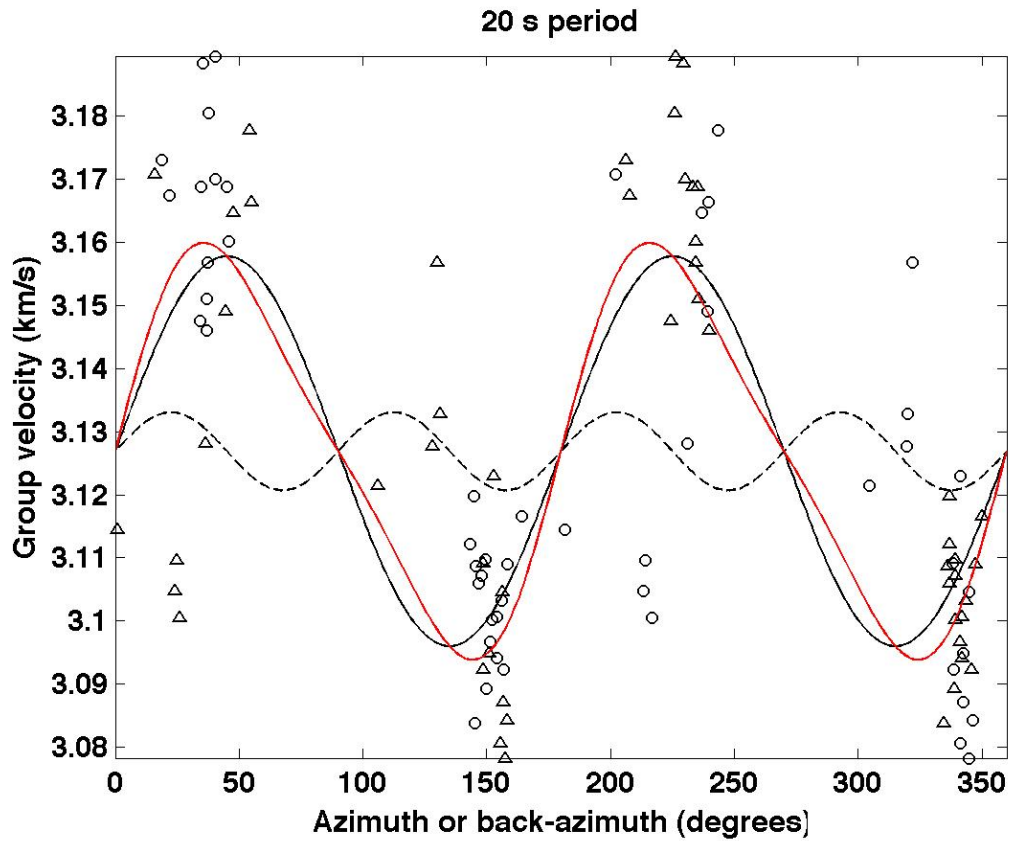


**Figure 3.6 Data fit to  $2\Psi$  and  $4\Psi$  variations.**

A selection of data taken from an area of dense path coverage at 20s period path locations are shown with the black box in Figure 3.4a. Solid black line represents the L1 norm best fit for  $2\Psi$  variations; the dashed black line is the L1 norm best fit for  $4\Psi$  variations. The red line is the L1 best fit to the data, and the sum of the  $2\Psi$  and  $4\Psi$  variations. The circles represent velocity values plotted with respect to azimuth and the triangles are plotted with respect to back-azimuth.

### 3.5 Resolution Testing

In order to test the robustness of the isotropic and anisotropic results, two resolution tests were performed. First, a purely isotropic “checkerboard” model was created (Figure 3.7), consisting of alternating high-velocity and low-velocity regions. For simplicity, no noise was added to the model. After forward modeling to create synthetic group velocity dispersion curves and inverting them using the same approach described in section 4, the checkerboard model was reconstructed. Figure 3.8 shows these results for 20 s and 30 s periods. An important element of this test is ‘leakage’ of the  $2\Psi$  anisotropy into the model. As mentioned above, although the input model was purely isotropic, the inversion results exhibit spurious anisotropy directions. The spurious anisotropy is relatively weak, meaning it is approximately  $< 1\%$ , but it does contain potentially misleading artifacts in regions of low path coverage. This can be seen, for example in the northeast corner of both the 20 s and 30 s maps, where there are northwest-southeast trending anisotropy directions, similar to the path directions in this area (Figure 3.4a). Anisotropy results in areas of low path coverage are therefore disregarded in our interpretations below. In addition, it needs to be stated that this test provides a lower bound on the isotropic bias.

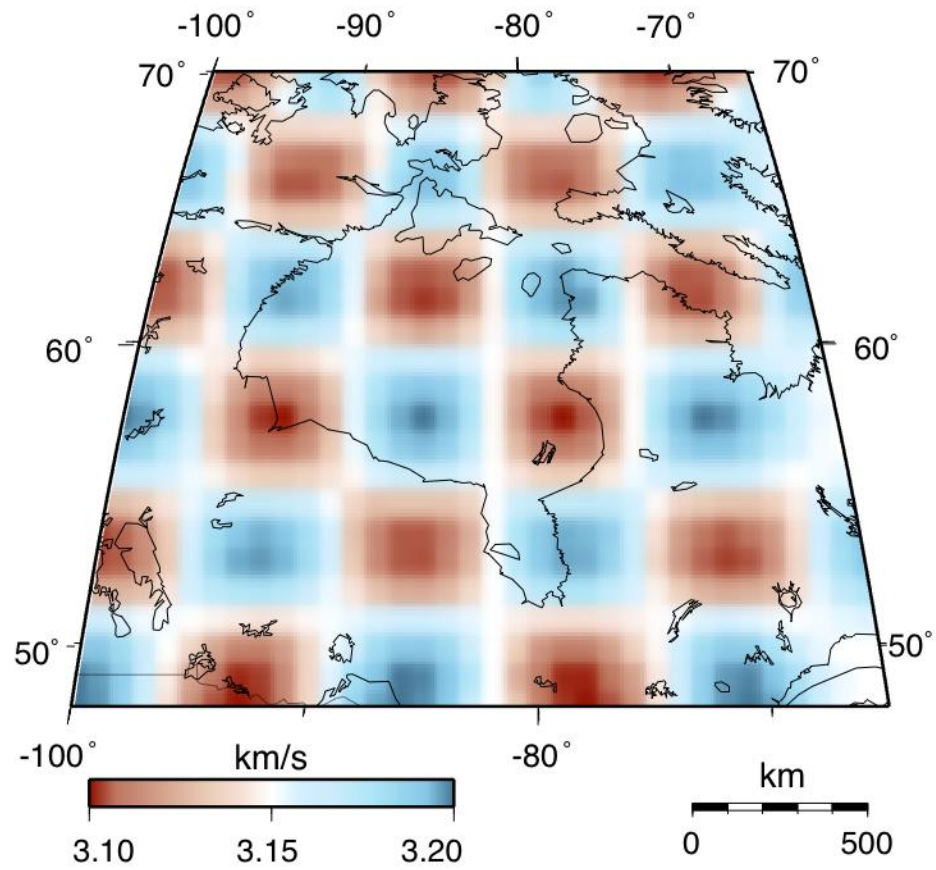


**Figure 3.7 Isotropic checkerboard model.**

Isotropic checkerboard model used for resolution testing.

To examine the robustness of the models and any possible artificial anisotropy in our results, we performed a second resolution test. This test consists of an input model created using isotropic velocities found in our results and anisotropic directions rotated 90 degrees (from a southwest-northeast direction to a northwest-southeast direction) (Figure 3.9a and b). Again, no noise was added to the input model. Reconstruction results (Figures 3.9c and d) for 20 s and 30 s periods recover the input pattern accurately, and in fact appear as a smooth version of the input models. This means that anisotropic directions are generally not biased by path directions or other possible artifacts in the inversion including choice of smoothing and damping parameters (Appendix A).

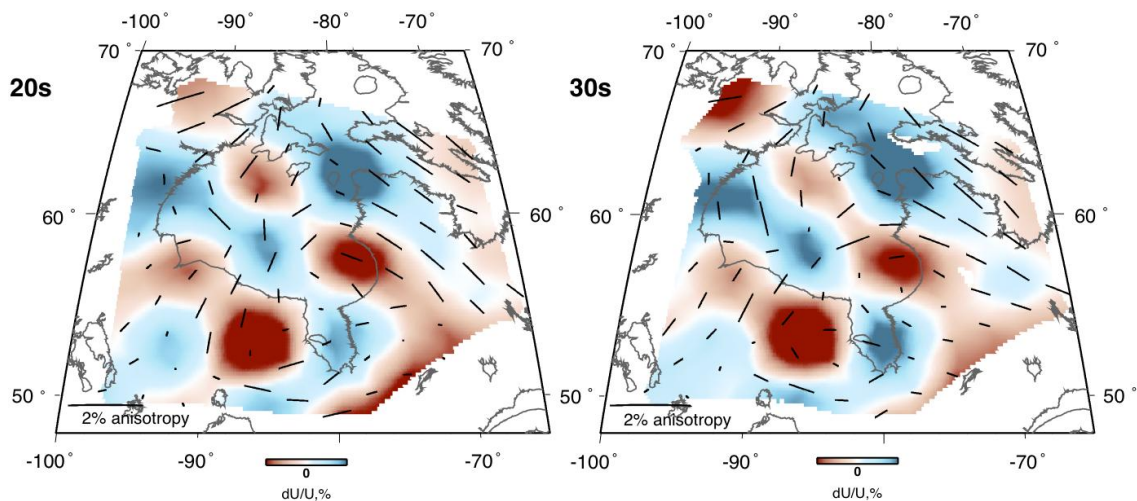


**Figure 3.8 Isotropic checkerboard reconstruction.**

Isotropic checkerboard reconstruction results for 20 s and 30 s periods. Isotropic velocities are well resolved, but with some anisotropy ‘leaking’ through, for example in the northeast corner.

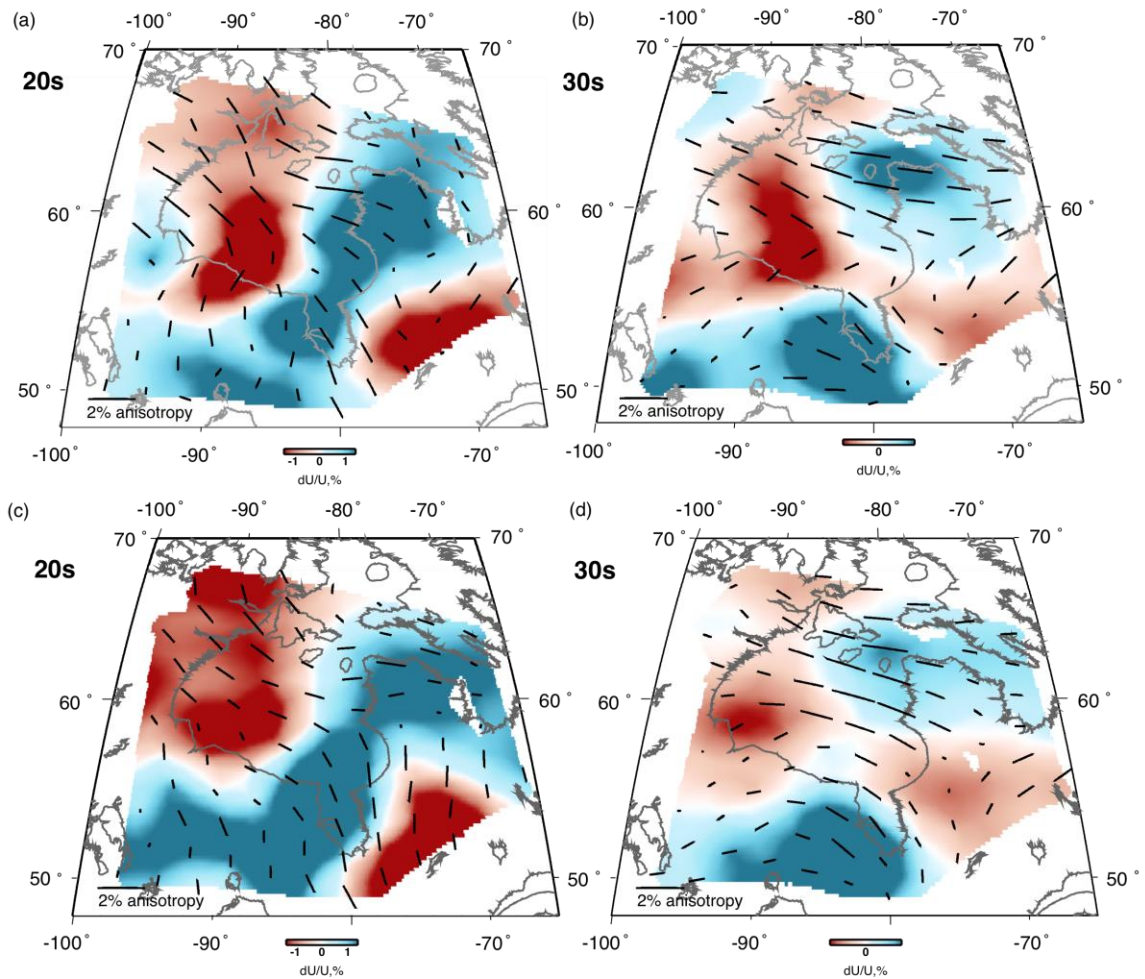


**Figure 3.9 Anisotropic resolution test.**

Inversion of anisotropy resolution reconstruction results for 20s and 30s periods. (a) The input model used for the inversion is the results (Figure 3.13) with the anisotropic fast direction rotated by 90 degrees at 20 s period; (b) same as (a) for 30 s period. (c) and (d) Reconstructions of model shown in (a) and (b). This tests for artefacts in the anisotropic patterns due to the unevenness of the path coverage.

### 3.6 Results

Results of the inversion using our preferred parameters are shown in Figure 3.10. As a rough guideline, the period value in s provides a proxy for the approximate depth of peak sensitivity in km (Lin et al., 2007). Thus, results for periods of 10-20 s are broadly representative of mid-crustal velocity structure, whereas results for 25-35 s are broadly representative of the lower crust. Red denotes lower isotropic velocities and blue denotes higher isotropic velocities with respect to the regional average for a given period. Through most of the crust there is a relatively low-velocity region near the center of Hudson Bay, as compared with the higher velocities that form a horseshoe shaped region that coincides with the Archean Superior craton (Figure 3.1b). This regional pattern of isotropic velocity variations is consistent with isotropic tomography results obtained by Pawlak et al. (2011), which are based on a different tomographic reconstruction method.

Black bars in Figure 3.10 show the  $2\Psi$  anisotropy fast directions. A predominant SW-NE fast direction characterizes the mid-crust (10s – 20s period maps), defining an anisotropic fabric that corresponds well with the surface tectonics of the region, namely, where we observe the horseshoe-shaped Superior craton (Figure 3.1b) (“double indenter”, Gibb, 1983; St Onge et al., 2006) as defined by relatively fast isotropic velocities. Furthermore, to the south and east of Hudson Bay anisotropic fast directions deviate from the dominant SW-NE direction to wrap around in accordance with the ‘horseshoe’ shaped pattern. This feature is most prominent in the 20s period map. At 25s period there is a significant transition in anisotropic fast direction to an almost N-S pattern. This pattern persists for

longer periods (30s period), although it is locally rotated (approximately 90 degrees) in the central region in the vicinity of the Nastapoka Arc (Figure 3.1b).

### **3.7 Discussion**

Seismological studies of crustal anisotropy typically make use of shear-wave splitting (e.g. Audoin et al., 2004) and/or surface-wave tomography methods (e.g. Gaherty, 2004). As noted above, various explanations for observed crustal anisotropy have been suggested. Proposed models for anisotropy include alignment of microcracks (Crampin et al., 1984; Kaneshima et al., 1988), preferred mineral alignment (Christensen and Mooney, 1995), fossil anisotropy due to the last tectonic event (Wüstefeld et al., 2010; Bastow et al., 2011), plate motion (Bokermann and Wüstefeld, 2009), stress direction (Crampin, 1981) and fabrics defined by geologic structures (Lin et al., 2011). In this section, we explore some of these models to help determine the origin of the anisotropic fabric in our data.

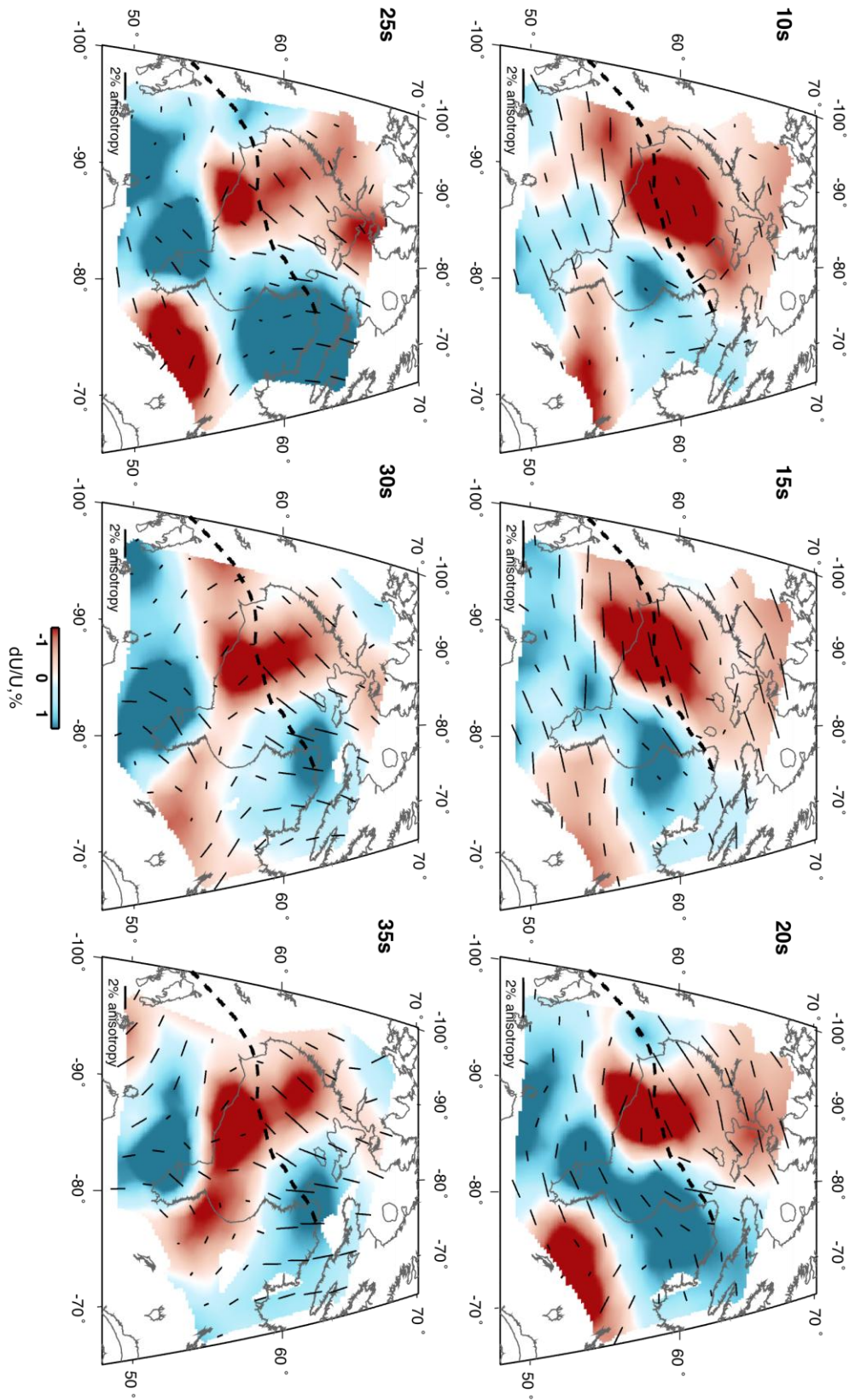


**Figure 3.10 Inversion results.**

Inversion results for periods 10 s, 15 s, 20 s, 25 s, 30 s, and 35 s. Through most of the crust there is a lower velocity region within the center of Hudson Bay, as compared with the higher velocities that form a horseshoe shaped region that coincides with the Archean Superior craton (Figure 3.1b). Anisotropic fast directions are predominantly SW-NE in the upper crust (10-20 s). There is a significant transition in the pattern at 25 s, carrying through the lower crust (30-35 s). Throughout the crust there is a difference in anisotropic fabric on either side of the inferred THO suture zone shown with a black dashed line (Figure 3.1b).

---

*3.7.1 Crustal Stresses*

Seismic anisotropy in the crust could be affected by stress direction as a result of preferred opening of microcracks (Crampin, 1981). Currently, there are sparse data constraining crustal stress directions in Hudson Bay (Heidbak et al., 2008). At a large scale, the orientation of maximum compressive stress in the shallow crust can be approximated by absolute plate motion (APM) directions (Wu, 1997). The inferred direction of plate motion in the study area, however, depends on the reference frame used (e.g. Bastow et al., 2011), making continent-scale inferences less conclusive. Within the Bay the maximum stress direction is generally NE-SW, although stress-field directions have changed in the last 9000 years due to glacial rebound stress following the last ice age (Wu, 1996). More recent studies based on moment-tensor inversion from local

earthquakes have confirmed the overall orientation of the stress field (Steffen et al., 2012). Using data from five earthquakes in northern Hudson Bay, Steffen et al. (2012) show a NNW-SSE directed maximum horizontal stress direction, not generally consistent with our principal anisotropic fast directions from this study.

In general, the crustal stress directions support the anisotropic fast directions seen in our data, but are characterized by longer length scales or variations. This alignment with crustal stresses is apparent mainly in the upper to mid crust. This could mean that the aligned microcracks or single direction foliation are dominating the background anisotropy, but smaller wavelength features such as those near the center of the Bay require a different explanation. In the following sections, we consider the possible role of frozen crustal deformation that occurred at the time of collision in creating these shorter wavelength features.

### *3.7.2 Magnetic Data*

Magnetic data have been used in recent years to help interpret observations of seismic anisotropy (Bokelmann and Wüstefeld, 2009; Wüstefeld et al., 2010). Due to the limiting temperature for ferromagnetic behavior and the depth decay for dipole fields ( $1/r^3$ ), magnetic data are well suited for studies of the uppermost lithospheric fabrics (Wüstefeld et al., 2010). Previous studies (Bokelmann and Wüstefeld, 2009) have found a relation between seismic anisotropy in the mantle from shear-wave splitting results compared with crustal magnetics. This relation is consistent with vertically coherent deformation, in which the crust and mantle deform as a unit (Silver and Chan, 1988). Since ambient-noise

studies are generally confined to the crust and uppermost mantle, comparing crustal magnetic features is appropriate.

Magnetic data are available from the Geological Survey of Canada (Figure 3.11; GSC, 2010). This assemblage of aeromagnetic and marine data is presented on a 400 m grid. Comparing the magnetic data and the 20 s period anisotropic results (Figure 3.10), there is a very similar pattern in the center of the Bay, showing possible influence of tectonic boundaries. This comparison suggests that the mid-crust has preserved an anisotropic signature similar to that predicted by the magnetic data, indicating that the crust at these depths is likely to have retained an anisotropic structure that dates back to the time of crustal formation in the Precambrian. The 30 s period anisotropy (Figure 3.10), however, appears to have little correlation to the magnetic data, suggesting that anisotropic fabrics in the lower crust may be characterized by an overprint that is not evident at shallower and deeper levels of the lithosphere. Such a depth dependence of deformation patterns and anisotropy has been documented in regions that are undergoing present-day deformation (e.g. Endrun et al., 2011). In the case of Hudson Bay, while the anisotropy of the brittle shallow crust may have retained an anisotropic signature since formation, the ductile lower crust/upper mantle anisotropic observations appear to be more sensitive to major mountain building events such as the THO, as is observed in the SKS studies of mantle anisotropy (Bastow et al. 2011).

We find that the 20 s period results (Figure 3.10) are primarily sensitive to the mid crust, whereas the 30 s period results (Figure 3.10) are sensitive to the lower crust. Knowing this and the decay rate of magnetic data with depth, a similarity between mid crustal

patterns of anisotropy and the magnetic anomaly in contrast to the lower crust is physically reasonable. An important feature of all the datasets is a conspicuous change in anisotropy direction across the suture zone (shown with the red arrows on the magnetic data in Figure 3.11). This juxtaposition suggests that anisotropic fabrics on either side of the suture formed prior to the termination (ca. 1.86 Ga) of the collision between the Superior craton and the Churchill Province. This observation supports our interpretation that the upper crustal anisotropy patterns preserve a primary tectonic imprint, and also provide a constraint on a minimum age of formation.

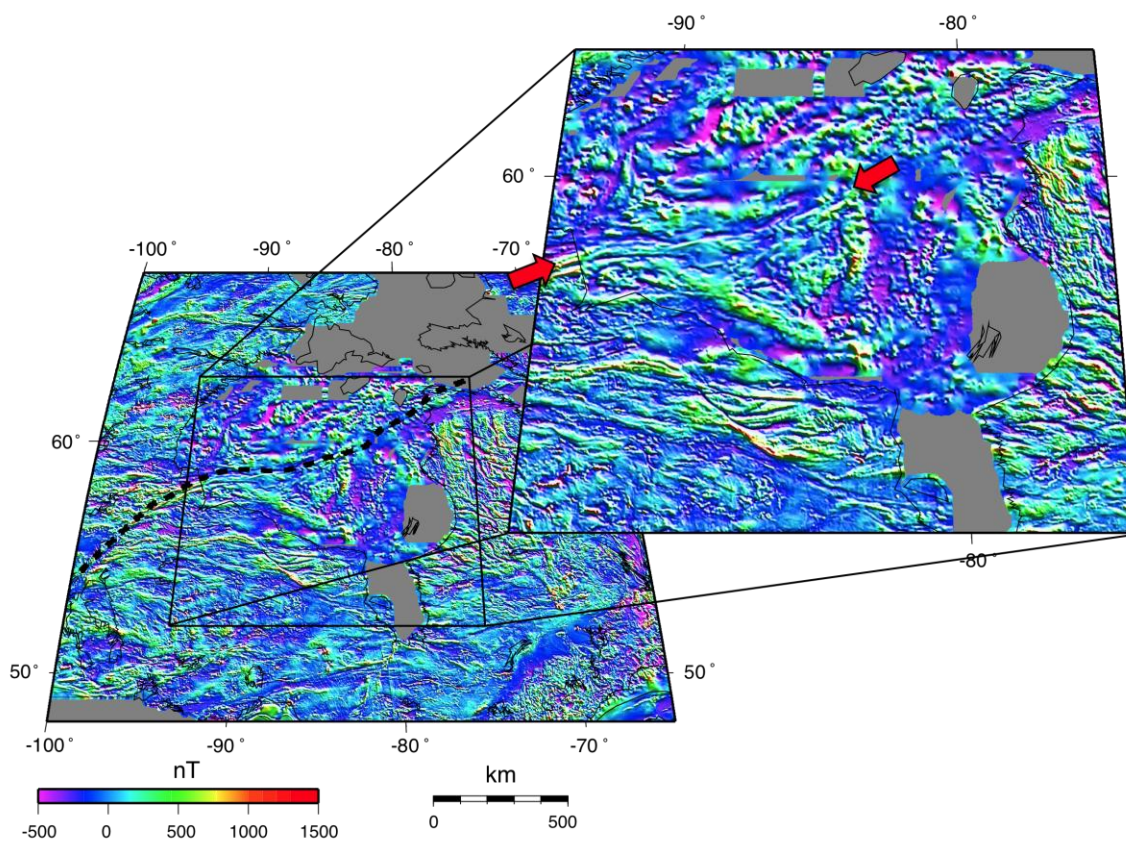


**Figure 3.11 Regional total-field magnetic anomaly data.**

Shaded relief image of regional total-field magnetic anomaly data (left) where the black dashed line represents the inferred suture. An enlargement of Hudson Bay highlights the magnetic response along the THO suture zone, indicated by the red arrows.

### 3.7.3 *Contrasting crustal profiles across suture*

The THO suture extends across Hudson Bay, separating the Churchill and Superior Provinces (Figure 3.1b – Eaton and Darbyshire, 2010) and it clearly manifests in regional magnetic anomaly data (Figure 3.11). To further explore how our anisotropic data varies on either side of the suture we show anisotropic dispersion curves (Figure 3.12) at two representative regions on either side of the suture. Figure 3.12 shows percent anisotropic amplitude versus period (Figure 3.12a and c) and fast direction azimuth versus period (Figure 3.12b and d) for locations HUB and SUP (Figure 3.12e). In each region, data from four knot points falling within the chosen region were extracted. The grey lines (Figure 3.12a and c) and grey stars (Figure 3.12b and d) are extracted data and black lines are averages.

There is a marked contrast in the upper crustal anisotropy (10 – 20 s). At HUB there is an increase of 0.7 – 1 % amplitude and azimuth around  $55 - 60^\circ \pm 10^\circ$ . However, at SUP the amplitude is nearly constant at 0.7 % and azimuth around  $20 - 40^\circ \pm 10^\circ$ . In the lower crust (30 – 40 s), both show more similar characteristics. At HUB the amplitude is  $\geq 1\%$  and azimuth is more constant at around  $35^\circ \pm 5^\circ$ . At SUP the amplitude is again more constant at 1 % and the azimuth at around  $20^\circ \pm 5^\circ$ . The upper crust shows definite differences in anisotropy across the suture, and is less defined in the lower crust.

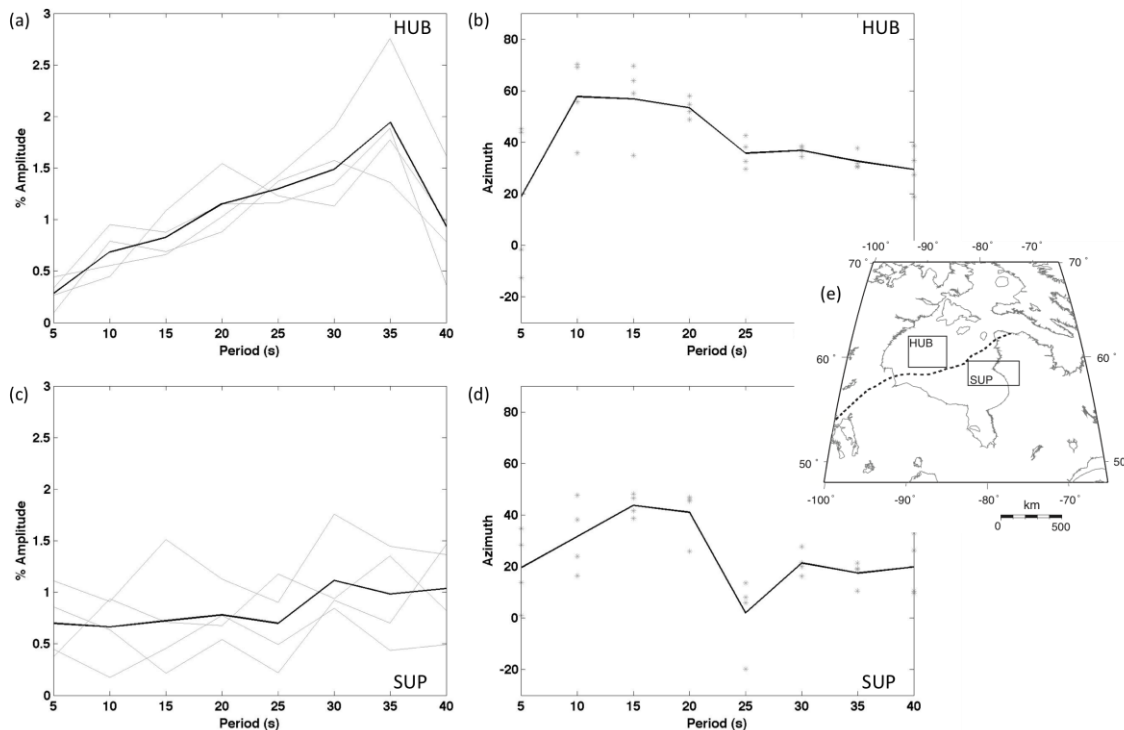


**Figure 3.12 Anisotropic dispersion curves.**

Anisotropic dispersion curves on either side of the suture. (a) Grey lines represent percent amplitude perturbation to the regional average for data located at HUB shown in (e) on the north side of the suture. Black line represents an average of the data in from the HUB region. (b) Grey stars show anisotropic fast azimuth distribution for a given period and the black line is an average fast direction azimuth for data in the HUB data. (c) Same as (a) for SUP. (d) Same as (b) for SUP. (e) Location of data for the anisotropic dispersion curves. The black dashed line represents the inferred THO suture zone.

### *3.7.4 Tectonic overprint in the lower crust*

In the preceding sections, our analysis of regional tectonic fabrics derived from seismic anisotropy indicates depth-dependent behaviour within the crust. In particular, at upper- and mid-crustal levels, based on ambient-noise recordings with periods of 20 s and less, we observe a good correspondence between fast seismic directions and tectonic fabrics evident from aeromagnetic maps, which are inferred to be representative of tectonometamorphic fabrics. Although robust and spatially coherent, anisotropic fabrics observed at 30 s period (corresponding approximately with lower-crustal depths) are dominated by a generally N-S orientation that crosscuts these tectonic trends in the shallow crust. This inferred depth variation builds on previous work in this area, based on SKS-splitting measurements in an overlapping study region centered immediately north of Hudson Bay (Bastow et al., 2011). Shear-wave splitting in SKS phases yields delay times ( $\Delta t$ ) of  $> 1.5$  s in much of northern Hudson Bay, where the observations are attributed to plate-scale deformation during the Trans-Hudson Orogen and earlier stages of craton assembly (Bastow et al., 2011) and to deeper asthenospheric fabrics associated with motion of the North American plate (e.g., Snyder et al., 2012). Towards the SW coast of Hudson Bay, no splitting was observed by Kay et al., (1999), who noted moderate-to-large (up to  $\sim 2$  s) splitting elsewhere. No shear-wave splitting studies have been performed using local events in the Hudson Bay region, so it is not clear to what extent the anisotropic fabrics we identify contribute to the SKS observations. However, estimates of the amount of splitting that can be accrued in the crust vary from 0.1–0.3 s (Silver, 1996) to 0.1–0.5 s (e.g., Barruol and Mainprice, 1993) with the implication that

crustal anisotropy does not contribute greatly to the SKS observations. In fact, since a vertically propagating S-wave takes  $\sim 11$  s to travel through a 40 km thick crust, this would, assuming an average 2% anisotropy, only result in 0.2 s of shear wave splitting, which is within the noise of the SKS study (Silver and Chan, 1988).

Here, we consider the possibility that observed seismic anisotropy of the lower crust reflects a younger tectonic overprint that is present at neither shallower levels of the crust, nor in the underlying mantle lithosphere. Such a scenario has been described in similar tectonic settings elsewhere. For example, based on geochronology of lower-crustal xenoliths in the southern Superior craton south of Hudson Bay, Moser and Heaman (1997) document an episode of zircon growth interpreted to be caused by intrusion of magma into the lower crust during Proterozoic rifting of the craton. Like Hudson Bay, this part of the Superior craton is characterized by SKS splitting results that generally align with regional tectonic trends (e.g., Frederiksen et al., 2007). Elsewhere, preferential reworking of the lower crust has also been attributed to magmatic underplating within a large igneous province in the Baltic Shield (Kempton et al., 2001), mafic magmatism associated with dike swarms in the Slave craton (Davis, 1997), and granulite-facies metamorphism in the North China craton (Liu et al., 2004).

Very low heat flow values documented in nearby regions of the Canadian Shield [e.g., *Rolandone et al.*, 2003] imply that the thermal regime of the entire crust is most likely in the brittle regime. Moreover, modeling of glacial isostatic adjustment [*Wu*, 2002; 2005] treats the entire lithosphere as an elastic plate and models the viscoelastic response within the underlying mantle. We therefore consider that it is very unlikely that the observed

lower-crustal anisotropy reflects channel flow in response to GIA within the past 15,000 years. Modern orogenic analogs imply that the channel flow direction follows the gradient from areas of high gravitational potential energy to areas of low potential energy (i.e. roughly perpendicular to topographic relief built up during orogenesis).

The apparent similarity of spatial and temporal characteristics for the Trans-Hudson and Himalayan orogens (St. Onge et al., 2006) suggests that processes in the lower crust may also be comparable in both cases. A model of gravitationally-driven channel flow in the lower crust beneath Tibet is now well established (Royden et al., 1997; Clark and Royden, 2000; Beaumont et al., 2001). The flow propagates through a channel zone in a weak lower crust at a rate driven by temperature, viscosity and horizontal pressure gradient (Beaumont et al., 2001; Clark et al., 2005). The stresses accumulated are then applied to the elastic upper crust, creating the dynamic topography in Tibet (Clark et al., 2005). We remark that modeling of Bouguer gravity data within Hudson Bay (Eaton and Darbyshire, 2010) and previous isotropic studies of ambient-noise tomography (Pawlak et al., 2011) suggest that lateral variations in density and crustal thickness are preserved in this region. In this context, it is interesting to note that numerical modeling (Bott, 1999) indicates that topographic relief and preservation of Moho topography due to local isostasy are both enhanced in the presence of lower-crustal channel flow.

### **3.8 Conclusions**

This study is among the first to use ambient-noise data to investigate azimuthal anisotropy. Our inversion method uses smoothing and damping parameters to regularize

the solution; due to the significantly increased number of model parameters relative to the isotropic case, considerable attention has been given to investigating whether “leakage” occurs between the isotropic and anisotropic parameters in the inversion. Isotropic velocity patterns found in this study are consistent with results found by Pawlak et al. (2011). Based on analysis of raw data in areas of high path coverage,  $4\Psi$  anisotropy appears to be negligible for the periods of main interest, allowing us to focus on  $2\Psi$  results. This is consistent with certain forms of anisotropy, such as azimuthal anisotropy in hexagonal symmetry systems caused by a single set of aligned cracks or metamorphic fabrics associated with LPO of certain minerals.

The anisotropic fast directions in the mid-crust (20 s period) are consistent with both regional magnetic anomalies and regional tectonic trends. Specifically, our ambient-noise inversions and magnetic anomaly maps both reveal a characteristic pattern impacted by a distinctive double-indenter geometry of the Superior craton. Our results also show a significant change in anisotropic direction across an inferred suture beneath Hudson Bay. Previous evidence from SKS-splitting measurements show vertically coherent deformation in the lithosphere; however, in this study the observed anisotropic patterns fade in the lower crust (30 s period). This pattern suggests that a post-orogenic phase of deformation in the lower crust, possibly as a result of channel flow, formed an overprint that was confined to the lower crust.

## Chapter Four: **JOINT INVERSION: AMBIENT-NOISE AND SURFACE WAVES**

### **4.1 Introduction**

Ambient-noise tomography (Shapiro and Campilo, 2004) has emerged in the past 8 years as a versatile and robust technique for passive imaging of the velocity structure of Earth's crust and upper mantle to maximum depths of  $\sim 60$  km. The popularity of the method is due, in part, to the widespread availability of data recorded by broadband seismograph networks installed around the world. Similarly, surface-waveform inversion techniques using earthquake recordings have been extensively used for imaging the Earth's subsurface (e.g., Romanowicz, 2003) from the lower crust ( $\sim 20 - 40$  km) to the top of the mantle transition zone ( $\sim 400$  km). While both of these methods employ ground-motion data recorded by broadband seismograph stations, surface-wave inversion is confined to occasional strong signals generated by earthquakes, whereas ambient-noise tomography uses much weaker but nearly continuous vibrations arising from interaction between ocean waves and continental margins (Stehly et al., 2006). The differences in depth sensitivity between these methods arises from inherent differences in frequency content;

ambient-noise recordings have maximum amplitudes predominantly in the period range of 5-20 s whereas, depending on the instrumentation used, surface waveforms often contain usable signals to periods as short as 20 s and as long as 300 s (Lebedev et al., 2009).

Given the complementary nature of the depth sensitivity for these two methods, there is a clear motivation to apply a joint-inversion approach, in which a simultaneous fit is sought to both types of data. In principle, a joint inversion of ambient-noise and teleseismic surface waves is expected to result in improved velocity imaging corresponding to frequency bands where the two methods both have strong signals (i.e.,  $\sim 20$ s period), together with extended depth resolution compared to either method taken individually. Several recent studies highlight the advantages of such a joint-inversion approach (Yao et al., 2006; Yang et al., 2008; 2011; Zhou et al., 2012).

This study extends the work described in previous chapters of this thesis by considering a joint isotropic inversion of data recorded using seismograph stations that encircle Hudson Bay. This work represents a component of the Hudson Bay Lithospheric Experiment (HuBLE), a collaborative international project aimed at investigating the lithosphere beneath Hudson Bay. In the next section below, we briefly review the tectonic setting of Hudson Bay. Next, we discuss both the ambient-noise and surface-wave datasets that are used in the joint inversion. Following this, we discuss the compatibility of the two datasets including an analysis of inversion ‘sensitivity kernels’ (i.e., partial derivatives of Rayleigh wave phase- and group-velocity functions with respect to subsurface shear-wave velocity). A Monte Carlo inversion process is used to perform the joint inversion

based on three different *a priori* velocity models. The resulting tomographic models are approximately converted from period (or frequency) into depth by performing a 1D inversion at each grid node. Compared to the tomographic results presented in Chapter Two using only the ambient-noise data, the resulting velocity maps exhibit improved resolution of the lower crust and upper mantle and highlight a near-vertical low-velocity band beneath Hudson Bay.

## **4.2 Tectonic Setting**

Hudson Bay is a shallow inland sea located near the centre of North America within the Laurentian craton, the ancient Precambrian core of the continent. The Bay is approximately 1000 m in diameter but only ~100 m deep, on average. It formed by marine inundation of the continental interior following the last Ice Age (Lee, 1968). Beneath most of the Bay lies the Hudson Bay basin, a saucer-shaped crustal depression containing rocks of Paleozoic age (Figure 4.1). The Hudson Bay basin is shallower (~ 2 km) but slightly more extensive than similar intracratonic basins elsewhere in North America (Michigan, Illinois, Williston). It has been suggested that these differences may be due to the presence of a relatively thick and stiff lithospheric keel at the time of basin formation (Eaton and Darbyshire, 2010). Several models have been proposed to explain the formation of the basin, with one theory postulating eclogitization in the lower crust (Fowler and Nisbet, 1985) similar to the Michigan basin (Hamdani et al, 1991) and supported by gravity data (Eaton and Darbyshire, 2010). A second model suggests that

the basin formed by crustal thinning driven by lithospheric extension (Hanne et al., 2004; Pawlak et al., 2011).

The crust that forms the basement beneath the Hudson Bay basin is comprised primarily of the ca. 1.91-1.81 Ga Trans-Hudson Orogen (THO), which is bounded by Archean cratons, represented by the Superior and Churchill Provinces of the Canadian Shield (Figure 4.1). The THO formed as a result of a collision between the Superior and Churchill protocontinents (Eaton and Darbyshire, 2010); it is considered to be similar in shape and size to the modern day Himalayan-Karakoram-Tibetan orogeny (St-Onge et al., 2006). A suture, i.e., a boundary between two tectonic domains that were previously separated by an ocean, extends across the centre of the Bay (Figure 4.1). Paleomagnetic evidence suggests that this suture manifested due to the closure of a Pacific-scale ocean (Manikewan; Symon and Harris, 2005) that once separated the Superior and Churchill cratons.

Although the lithosphere-asthenosphere boundary (LAB) remains difficult to characterize (Eaton et al., 2009), the lithospheric mantle keel beneath Hudson Bay is estimated to be at least 200 km in thickness, typical of Archean mantle keels (Darbyshire and Eaton, 2010). The subcratonic lithosphere beneath Hudson Bay is characterized by a high-velocity 'lid', also typical of cratonic regions and clearly seen in tomographic images (Darbyshire and Eaton, 2010).

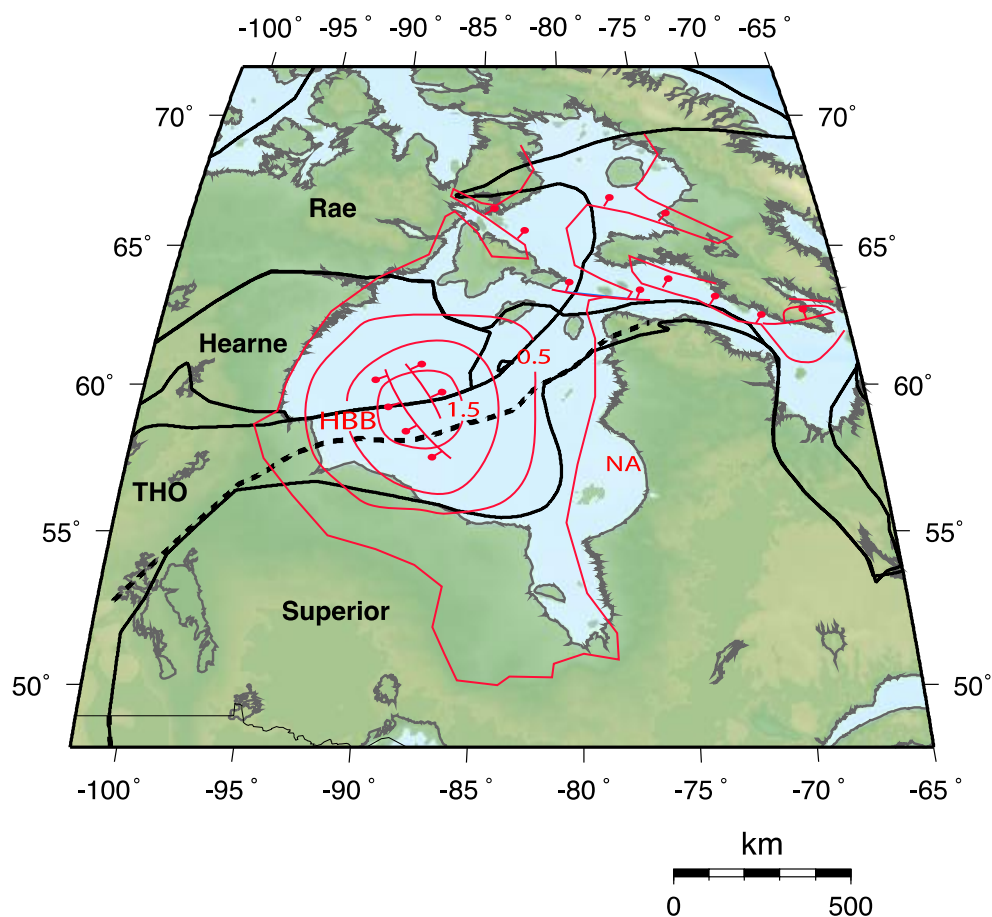


**Figure 4.1 Generalized geology map.**

Tectonic map of Hudson Bay. Solid black lines are approximate locations of tectonic boundaries and the dashed black line represents the suture zone between the Churchill (Rae and Hearne) and Superior Provinces. The red lines outline the location of the Hudson Bay basin, mapped faults and total sediment isopach contours in kilometers. Abbreviations are as follows: THO, Trans-Hudson orogen; HBB, Hudson Bay basin; NA, Nastapoka Arc (After Eaton and Darbyshire, 2010).

## 4.3 Data

### 4.3.1 *HuBLE Network*

Raw ground-motion data for this project were collected from stations located around the periphery of Hudson Bay (Figure 4.2). Most of these stations were operated as part of the HuBLE initiative, a collaborative project between the University of Calgary, Université du Québec à Montréal, University of Manitoba, University of Western Ontario, the Geological Survey of Canada and the University of Bristol in the UK. The aims of the HuBLE project are to better understand the lithospheric structure and evolution beneath Hudson Bay. The stations currently deployed consist of three-component broadband seismometers recording continuous data since ~2006, as well as geodetic and magnetotelluric instruments.

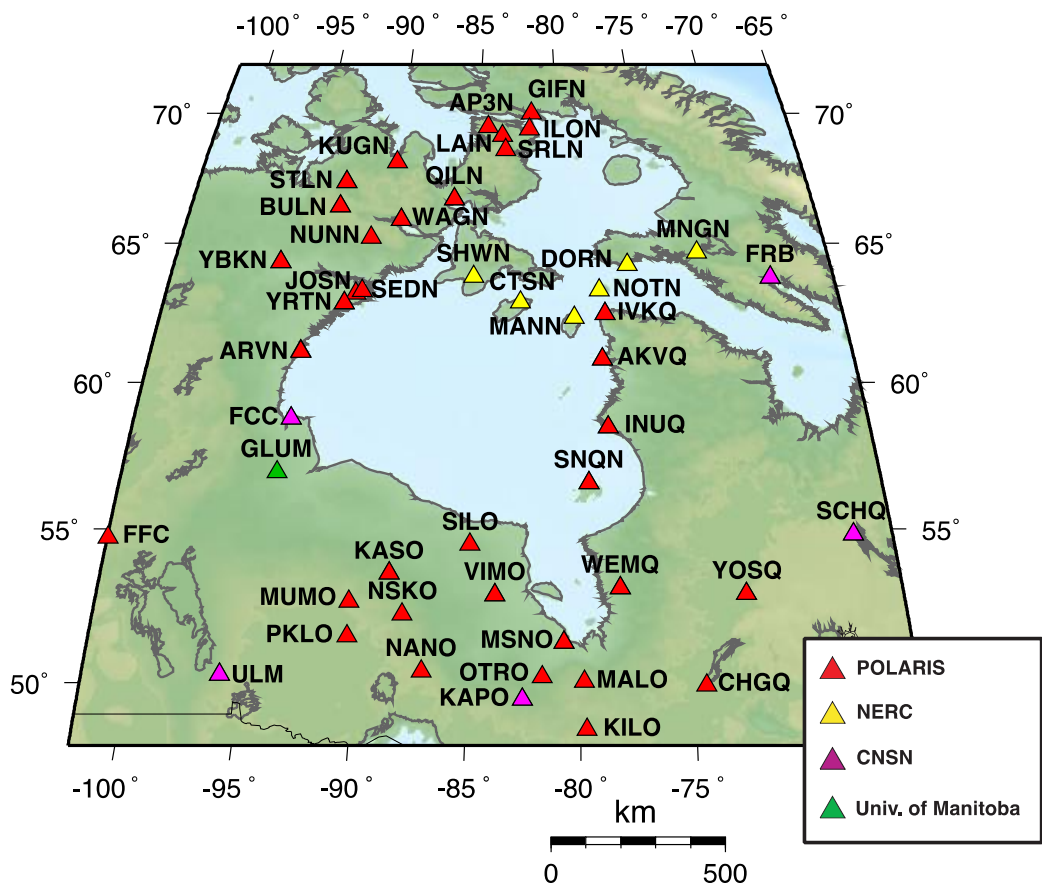


**Figure 4.2 Seismograph station map.**

Map of Hudson Bay showing all seismograph stations used in this study.

#### *4.3.2 Ambient-Noise*

The ambient-noise analysis is based on cross-correlation of continuous vertical component recordings of ground motion from 37 broadband seismograph stations. The processing method used here follows Bensen et al. (2007), as modified by Pawlak et al. (2011). Continuous recordings are cut into individual day-long recordings and resampled to 1 Hz. Next, the daily trends, means and instrument responses are removed and the signals are scaled using a one-bit time normalization procedure to suppress earthquake signals and instrument irregularities that inhibit the ambient-noise inversion procedure. The spectrum of the recordings is then whitened and bandpass filtered between 0.005 Hz and 0.3 Hz. Details of the processing procedures are given by Pawlak et al. (2011).

Once the daily noise signals are pre-processed, cross-correlations between all possible stations pairs are computed and stacked for all available daily records. This yields an estimated Green's Function (EGF) for each inter-station path containing both the causal and acausal signals. A one-sided EGF is obtained by selecting either the causal or acausal half of the EGF with the largest signal-to-noise ratio (SNR) (Pawlak et al., 2011). The selection of the higher SNR signal accounts for the asymmetry in the noise sources. Rayleigh-wave group velocity dispersion curves are then estimated using time-frequency analysis (Bensen et al., 2007). This approach consists of applying a narrow-band filter for a given frequency to the EGF and then calculating the absolute amplitude envelope. The group velocity is obtained by tracking the peak of the amplitude envelope of each period. A fundamental-mode Rayleigh-wave group velocity dispersion curve is obtained for each station pair and represents an average velocity structure between the two stations.

### 4.3.3 Surface Waves

Fundamental-mode Rayleigh wave data used in this study were acquired and processed by Darbyshire et al. (2012). The data were collected from 33 broadband seismograph stations from around the Hudson Bay region, most of which are the same as those used for the ambient-noise study. The basic processing of these data is summarized here for completeness; the reader is referred to Darbyshire et al. (2012) for details.

Teleseismic earthquake data of magnitude 5.5 and greater are collected based on two data selection criteria. First, only events lying within  $\pm 5^\circ$  of the inter-station great-circle path are selected for each station pair. Secondly, data quality is checked for the stations for both the unfiltered seismograms and for traces filtered at different pass-bands to enhance the Rayleigh wave signal. Instrument responses are standardized for each station pair.

The method of Meier et al. (2004) is used to calculate the fundamental-mode Rayleigh wave phase-velocity dispersion curves. Source phase and path effects from the source to the nearest station can be cancelled out by simultaneous analysis of the same surface wave at two stations lying on the same great-circle path. Removing the source effect allows analysis of an average structure between the two stations.

Dispersion curves are estimated by cross-correlating seismograms at two stations for the same event along the same great-circle path. Initial quality control is done using frequency-time-amplitude plots with multiple filter analysis for both the seismograms and the cross-correlation functions. Next, the maximum-amplitude arrival of the cross-correlation function is filtered and windowed using a frequency-dependent Gaussian

bandpass filter and Gaussian window to enhance the SNR and down weight the effects of correlation with scattered energy and higher modes. The cross-correlation function is then transformed to the frequency domain and the complex phase is used to calculate the phase velocity. The solution has a  $2\pi N$  ambiguity term, resulting in an array of possible solutions. Comparing with a global reference enables selection of the correct  $N$  value for the seismogram pair to unwrap the phase spectrum. Averaging of dispersion data for multiple events along the same great-circle path is also done to ensure good quality data. It is also important to have reciprocal paths and a range of epicentral distances, to make sure there is no significant bias.

#### **4.4 Two-Stage Inversion Process**

The inversion for shear wave velocity structure employed herein uses a two-stage method described by Shapiro and Ritzwoller (2002), Yang et al. (2008) and Bensen et al. (2009), where in the first step, period-dependent 2D tomographic group and phase velocity maps are created from two-station dispersion curves. The second step takes 1D dispersion curves extracted at each geographic location, on a predefined tomographic grid (Figure 4.3). These group-velocity and phase velocity 1D curves are then simultaneously inverted for shear-wave velocity structure at each grid point and compiled together using standard interpolation / gridding procedures (GMT, Wessel and Smith, 1995, Matlab) to create a 3D volume.

#### 4.4.1 Tomographic Surface Wave Inversion

Both two-station ambient-noise group-velocity and surface wave phase-velocity dispersion curves (discussed in Section 1.3.2 and 1.3.3) are, first, inverted using a least-squares inversion method used commonly in teleseismic surface wave studies (Deschamps et al., 2008; Darbyshire and Lebedev, 2009; Endrun et al., 2011). This inversion scheme inverts for isotropic and anisotropy heterogeneities. Working at the Earth's surface within a spherical co-ordinate system defined by  $\theta$ ,  $\phi$ , the average group-velocity,  $\delta U_i(\omega)$ , (or  $\delta C_i(\omega)$  for average phase-velocity) can be expressed in terms of the group-velocity model perturbations  $\delta U(\omega, \theta, \phi)$  as

$$\int_0^\pi \int_0^{2\pi} K_i(q, f) dU(\omega, q, f) df dq = dU_i(\omega) \quad , \quad (4.1)$$

where  $\omega$  is angular frequency and  $K_i$  defines a sensitivity function for the  $i$ th station pair. Following Darbyshire and Lebedev (2009), the sensitivity function is defined here by rays along inter-station great-circle paths (finite-width rays can also be easily accommodated within this formalism). The integration used to construct Equation 4.1 is performed using a dense (40 km) integration grid of nodes. To account for the effects of weak Rayleigh-wave anisotropy, the period-dependent group-velocity perturbations  $\delta U(\omega)$ , and similarly the phase-velocity perturbations  $\delta C(\omega)$ , are parameterized using 5 unknowns (Smith and Dahlen, 1973):

$$dU(\omega) = dU_{iso}(\omega) + A_1(\omega)\cos(2Y) + A_2(\omega)\sin(2Y) + A_3(\omega)\cos(4Y) + A_4(\omega)\sin(4Y) \quad , \quad (4.2)$$

where  $\delta U_{iso}$  is the isotropic group-velocity perturbation, or  $\delta C_{iso}$  for phase-velocity perturbations, and  $\Psi$  denotes the wave-propagation azimuth with respect to geographic north. Terms that depend on  $2\Psi$  and  $4\Psi$  in Equation 4.2 account for azimuthal variations of group (or phase) velocity that exhibit a periodicity of  $\pi$  and  $\pi/2$  radians, respectively. The 5 model parameters in Equation 4.2 are computed on a coarse (200 km) triangular model grid (Figure 4.3), where the node locations are determined using the method of Wang and Dahlen (1995). For this study only the isotropic velocity term is used in the analysis, although anisotropy is accounted for by the inversion process.

#### *4.4.2 Monte-Carlo Inversion*

The second part of the procedure further divides into two substeps. The first is a linearized inversion of the dispersion curves for 1D velocity structure similar to the method of Yang and Forsyth (2006). This process does not accommodate the nonuniqueness of the inverse problem, which leads to the second part of the procedure. A Monte-Carlo search is done in the model space that is defined by the results of the linearized inversion. This results in a set of velocity models that fit within acceptable criteria and uncertainties.

The linearized inversion uses a user-defined starting model (defined in section 4.8.1) to forward model and predict dispersion curves based on the input model. The inversion works by perturbing the input model providing misfit information and using an iterative least-squares approach to converge toward a locally best-fitting velocity model. Data misfit is calculated using a reduced chi squared approach, as described by Bensen et al. (2009). For Rayleigh waves chi squared is defined as

$$c^2 = \frac{1}{n} \sum_{i=1}^n \frac{(\tilde{d}_i - d_i)^2}{S_i^2}, \quad (4.3)$$

where  $i$  is the index of the period of the measurement,  $\tilde{d}_i$  and  $d_i$  are the model predicted and measured wave velocities, respectively, and  $S_i$  is the uncertainty of the measured velocity for a given period, wave type and location. Ambient-noise group-velocities are on a 5 s grid from 5 – 40 s and surface waves are on a 5 s grid between 20 – 40 s and on a 10 s grid from 40 – 220 s. The  $n$  value is 8 for group velocities and 22 for phase velocities (Bensen et al., 2009). A chi squared value of 2 or less represents a good fit, however, there still may be error for values between 1.5 to 2 (Bensen et al., 2009).

Using *a priori* information, such as a range of crustal thickness, crustal  $v_s$ ,  $v_p$ , and  $\rho$ , we can quantify the range of acceptable velocity models which are physically reasonable. The *a priori* information is employed in a user-defined starting model (defined in section 4.8.1) to forward model and predict dispersion curves based on the input model. The Monte-Carlo procedure follows a two-step process. First, a set of models are created with uniformly distributed random perturbations, within an allowable range around the starting model. Next, a search is performed wherein the current model is randomly perturbed to find the next model, refining the search for acceptable models. The search then re-initializes in the neighbourhood of each accepted model, until 100 acceptable models are found. The predicted dispersion curve must fit the measured dispersion curve to within an average misfit of less than twice the data uncertainty. The best-fit model is selected as the mean model of the acceptable models.

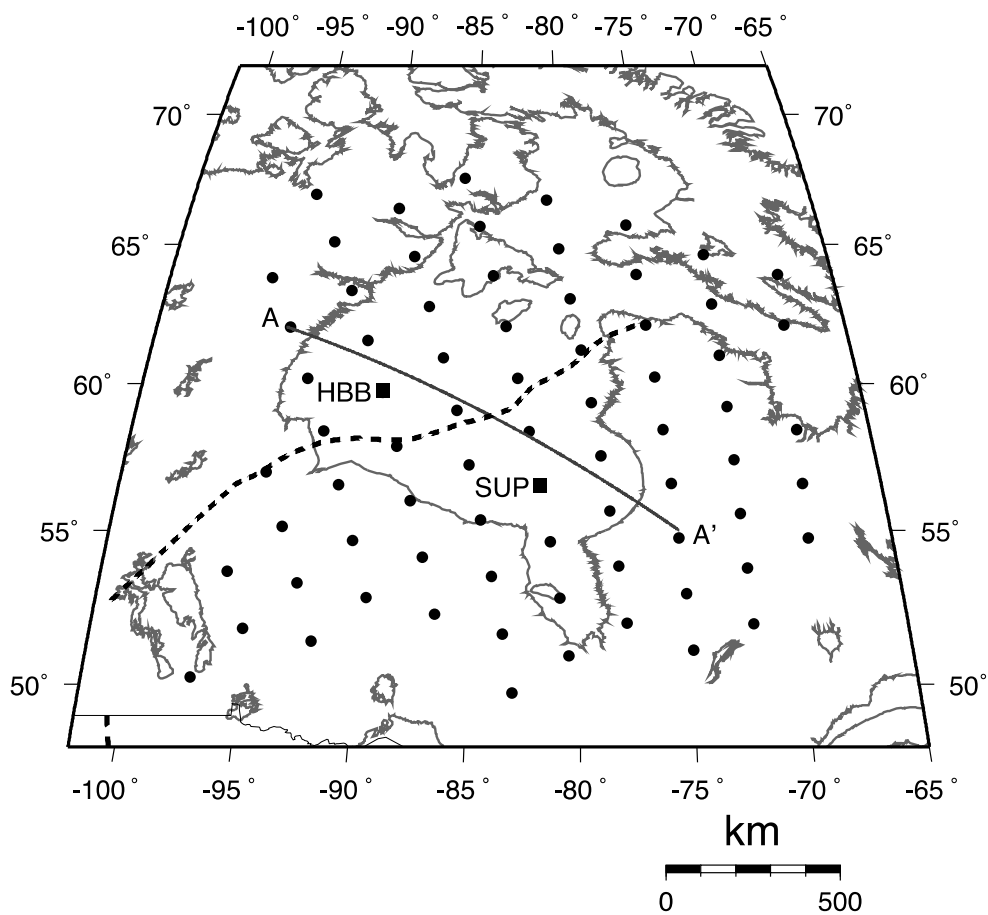


**Figure 4.3 Grid node map.**

Map of grid nodes used for inversion (black circles). The black squares show grid nodes for which 1D depth profiles are shown in Figure 4.10 and 4.11. The black line marks the location of the cross-section (A-A') shown in Figure 4.13. Black dashed line represents the THO suture zone. HUB and SUP represent locations of 1D inversions shown in Figures 4.10 and 4.11.

## 4.5 Sensitivity Kernels

The relationship between the shear-wave velocity structure of the crust and upper mantle and the measured Rayleigh-wave velocities is described by so-called sensitivity kernels. Sensitivity kernels represent partial derivatives of the group velocity,  $U$ , or the phase velocity,  $C$ , with respect to a depth-dependent model parameter,  $m(z)$ , for a specific Earth model. The analysis of sensitivity kernels can provide useful insight for understanding depth sensitivity for the frequency (period) bands investigated as well as inherent differences between group and phase velocity. To calculate sensitivity kernels, first the phase-velocity partial derivatives are computed from the eigenfunctions of a specific Earth model (Takeuchi et al., 1964). The group-velocity partial derivatives are then computed using the phase-velocity kernels, as described below. The choice of Earth model is very important, because the kernels are sensitive to the background velocity model. Here we evaluate sensitivity kernels for both *ak135* and *CANSD* Earth models.

### 4.5.1 Earth Models

The two Earth models we use are standard reference Earth models. The first is *ak135* (Kennett et al., 1995), which is similar to a previous reference Earth model *iasp91* (Kennett and Engdahl, 1991) everywhere except at the boundary of the inner core. This global reference model is derived from empirical traveltimes from for all major seismic phases from the catalogues of the International Seismological Center. The other Earth model considered is the Canadian Shield model, *CANSD* (Brune and Dorman,

1963). CANSND is an average model derived from a compilation of measurements of inter-station phase velocities from across Canada, largely crossing the Canadian Shield.

Figure 4.4 shows both Earth models and their associated phase- and group-velocity dispersion curves, for comparison. The *ak135* model describes a two-layer crustal model with a Moho at 36 km depth. The mantle is nearly uniform, and exhibits only a slight increase in velocity with depth. The CANSND model describes a three-layer crust and a Moho at 36 km depth as well. There is a high-velocity mantle lid in this model extending to 115 km depth. The two models have very different character; for example, the crust is more gradational for CANSND than *ak135*, which has a greater jump in velocity between the layers. Since the CANSND model describes the Canadian Shield, it is considered to be more appropriate to our datasets.

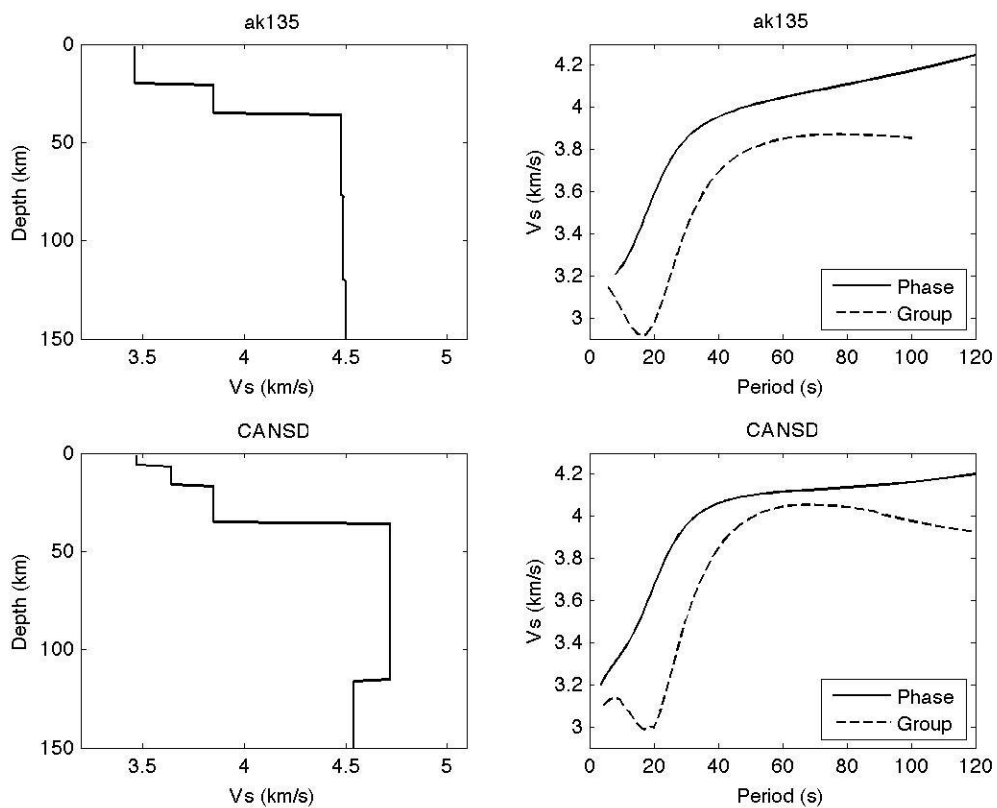


**Figure 4.4 Earth models.**

Summary of Earth models CANS D and *ak135*. On the left are the Earth models for shear-wave velocity and on the right are the corresponding phase and group-velocity dispersion curves.

#### 4.5.2 Partial Derivatives

Analytical expressions for partial derivatives of phase velocity with respect to a model parameter come from energy equations, or equivalently, fundamental equations and boundary conditions in surface wave problems (Takeuchi et al., 1964). However, phase velocity partial derivatives can be computed directly from the eigenfunctions of the phase velocity of a specific Earth model (Takeuchi et al. 1964; 1972; Dalton et al., 2011). We calculate the phase velocity partial derivatives for the two Earth models, CANSD and *ak135*, using *surf96* software by Herrmann and Ammon (2002).

Following the approach by Rodi et al. (1975), group-velocity sensitivity kernels can then be computed from the phase-velocity kernels using

$$\frac{\partial U}{\partial m} = \frac{U}{C} \frac{\partial C}{\partial m} - \frac{U}{C^2} \frac{\partial C}{\partial m} + W \frac{U}{C^2} \frac{\partial C}{\partial m} \frac{\partial C}{\partial m} \quad (4.3)$$

The resultant phase- and group-velocity sensitivity kernels for 20 s and 40 s periods for both *ak135* and CANSD are shown in Figures 4.5 and 4.6, respectively. Note that the phase-velocity results are scaled by a factor of 1.5, for better comparison of kernel shapes. Periods 20 s and 40 s represent the period range where our group and phase velocities overlap. For *ak135*, the phase-velocity kernel is very broad, representative of inversion sensitivity to a greater depth range. We find that the phase velocity at 20s period has a peak sensitivity at about 25 km, while the group velocity has a much shallower peak sensitivity at about 10 km. However, at 40s period both group and phase velocity exhibit similar depth sensitivity. For CANSD, we see that generally for both 20s

and 40s period, group velocity is sensitive to a slightly shallower depth than the phase velocity. As expected, the 40s period kernel is sensitive to a broader depth range than the 20s kernel.

Comparing the two Earth models, it is apparent that CANS<sub>D</sub> has a deeper sensitivity than *ak135* due to its higher model velocities, particularly in the upper mantle. In addition, phase-velocity kernels are generally broad, asymmetric and positive definite, whereas the group-velocity kernels have prominent positive and negative lobes. The negative lobe may introduce “leakage” during the inversion process from the crust into the mantle (or vice versa). Because of this possible negative leakage, phase-velocity inversion of both surface-wave and ambient noise data is preferred, where possible. In cases where it is not possible to obtain satisfactory phase-velocity data for ambient-noise measurements, joint inversion of both phase and group velocities may mitigate some of the undesirable effects of inversion for group velocity alone.

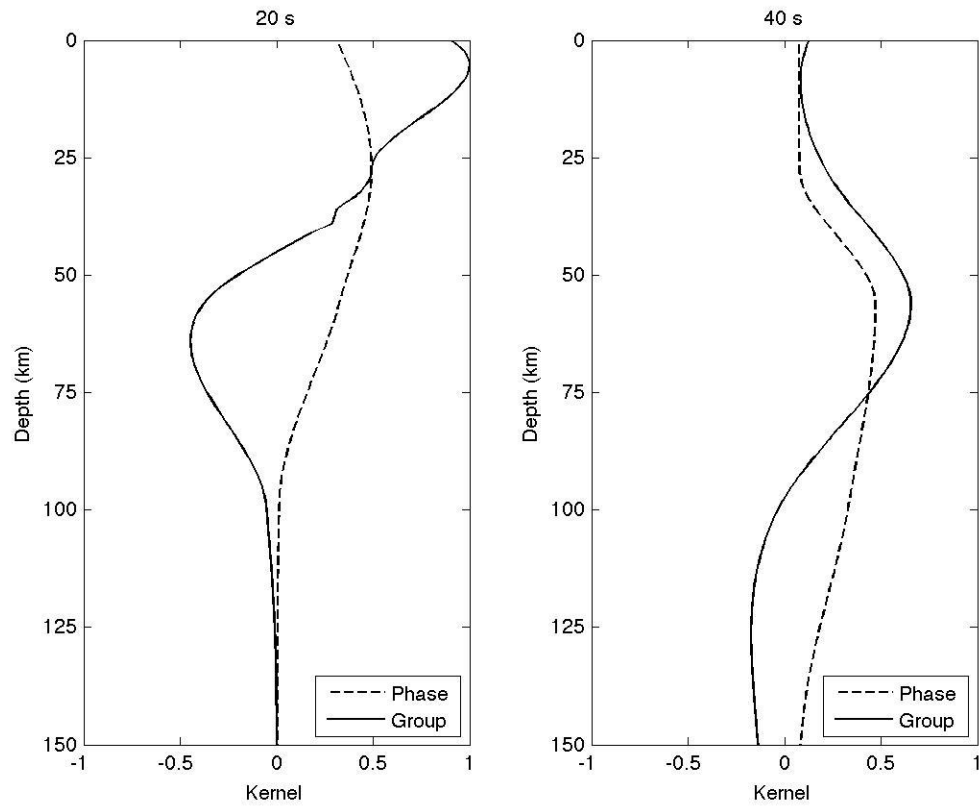


**Figure 4.5** Sensitivity kernel for *ak135*.

Sensitivity kernels for group and phase velocity for 20 s and 40 s period, for reference Earth model *ak135* (Figure 4.4).

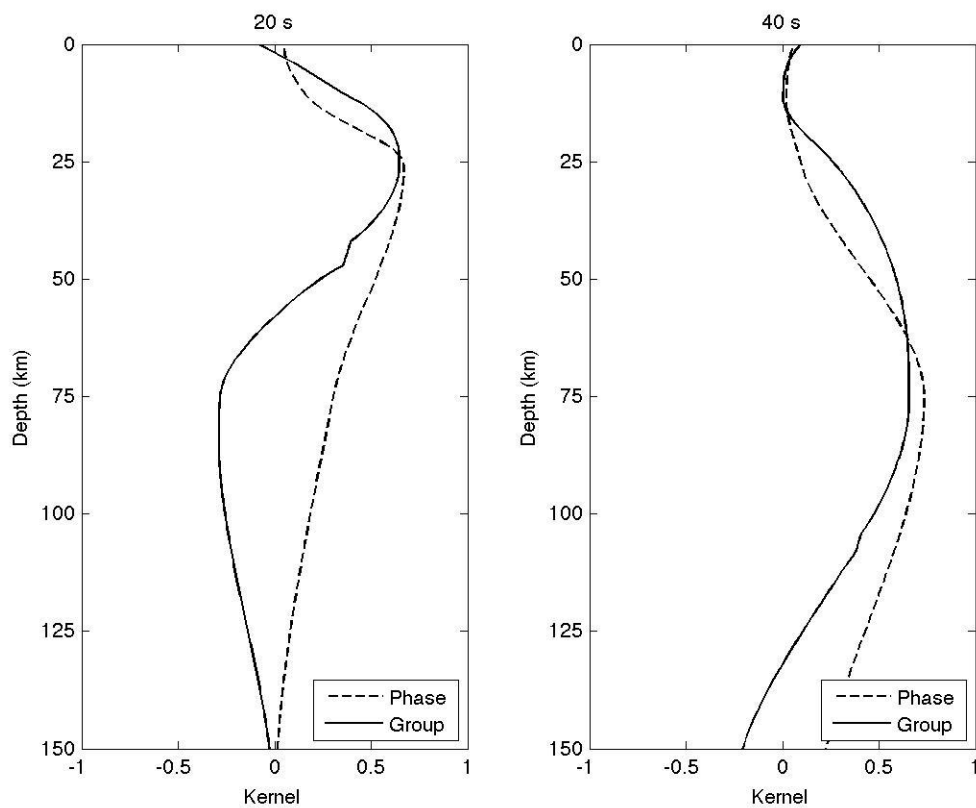


**Figure 4.6 Sensitivity kernel for CANSD.**

Sensitivity kernels for group and phase velocity at 20s and 40s period for Earth model CANSD (Figure 4.4).

#### 4.6 Ambient-Noise Phase Velocity

Generally, the use of phase-velocity dispersion from ambient-noise data is considered to have advantages over group velocity (Lin et al., 2008). Following the method described by Lin et al. (2008), in this section we compute phase-velocity dispersion curves to compare with group-velocity dispersion results that have been obtained previously. The phase function,  $\phi(t, \omega)$ , for a given instantaneous frequency can be written as,

$$f(t, \omega) = kr - \omega t + \frac{\rho}{2} - \frac{\rho}{4} + 2\rho N + l \quad , \quad (4.4)$$

where  $t$  is the traveltime,  $r$  is interstation distance,  $k$  is wavenumber,  $\pi/2$  is the phase shift from the negative time-derivative,  $-\pi/4$  is the phase shift due to the interference of a homogeneous source distribution,  $\lambda$  is the ‘initial phase’ term, and  $N$  is an integer value associated with unwrapping the phase spectrum and is referred to as the intrinsic phase ambiguity (Bensen et al., 2007). Lin et al. (2008) showed that for ambient noise data,  $\lambda \sim 0$  is approximately true; this means that the phase velocity can be written as:

$$C = \frac{\omega}{k} = \frac{r\omega}{[\phi(t_{\max}) + \omega t_{\max} - \frac{\rho}{4} + 2\rho N]} \quad , \quad (4.5)$$

where  $t_{\max}$  is the group velocity traveltime, calculated from the peak of the amplitude envelope and  $\phi$  is the instantaneous phase (Yilmaz, 1987).

The intrinsic phase ambiguity value,  $N$ , contributes to a significant uncertainty in phase-velocity calculations. In Figure 4.7, phase-velocity dispersion curves calculated using this

method are compared with group-velocity dispersion curves calculated using the method described in chapter 2. For reference, phase- and group-velocity dispersion curves are plotted for the CANS D model. The phase velocity curves are determined using frequency-dependent  $N$  values that minimize the misfit with CANS D. In Figure 4.7 the grey lines curves were computed with  $N \pm 1$ . Although this small change in  $N$  significantly modifies the phase-velocity dispersion curves, ambiguity remains in its choice. For example, the group-velocity curves suggest that the observed data have a higher velocity than CANS D for a period of 20s; it is not clear, however, whether it is appropriate to select the phase velocity dispersion curve associated with the  $N+1$  intrinsic phase ambiguity.

Generally, long-period phase velocities ( $\sim 30$ s and greater) are more sensitive to the  $N$  ambiguity term and thus are more strongly affected by the phase unwrapping uncertainties in our data. We can also see in Figure 4.7 that, although some results are very sensitive to the choice of  $N$ , others are only slightly affected. Thus, based on the quality of our dataset and resulting ambiguity in the phase velocities, we prefer the use of group velocities and retain these for the inversion.

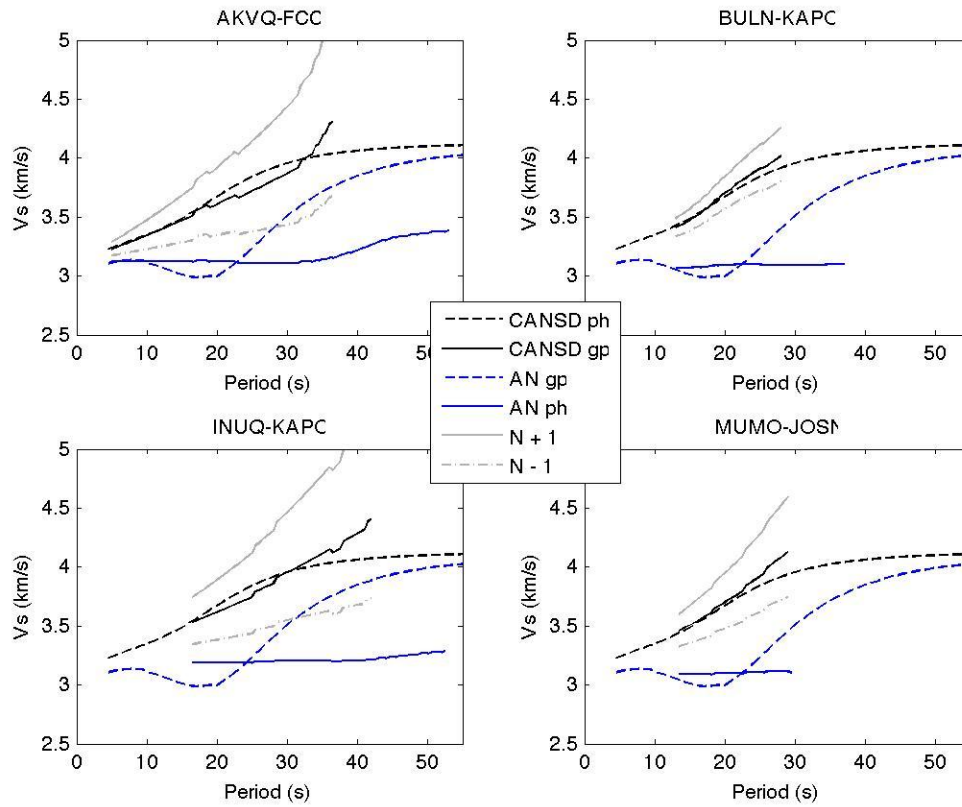


**Figure 4.7 Ambient-noise phase velocity**

Examples of ambient-noise phase velocities compared with ambient-noise group velocities and reference model CANSD. Also shown in grey are ambient-noise phase velocity curves ambiguity for intrinsic phase ambiguity value ( $N$ ) increased or decreased by 1. Group velocities are preferred in this study because of the ambiguity in the unwrapping of phase velocities.

#### 4.7 Compatibility of the datasets

Group velocity is defined as the speed at which a wave packet travels, and phase velocity is the speed at which an individual phase of a single frequency component within the packet travels. For crustal studies using teleseismic surface waves and ambient noise tomography, group and phase velocity for Rayleigh and/or Love waves have been inverted simultaneously (Moschetti et al., 2010; Zhou et al., 2012). Inherent differences in the data uncertainties and depth sensitivity kernels, however, imply differences in the behaviour of the inversion that could affect the compatibility of these two types of data for joint inversion. For example, as illustrated in Figure 4.6, for a given period range, phase velocity tends to have a relatively higher sensitivity to deeper parts of the velocity model than does group velocity (Yang et al., 2008). In addition, phase-velocity measurements tend to have smaller uncertainty than group velocities (Yang et al., 2008), as shown by the error bars on the dispersion curves in Figure 4.8.

In the case of our ambient-noise data from Hudson Bay, the group-velocity dispersion curves are generally relatively flat versus period (Figure 4.7). This characteristic is considered to be representative of a thick crust (Lin et al., 2008), consistent with the thick (by global standards) crust found in the Hudson Bay region (Thompson et al., 2010).

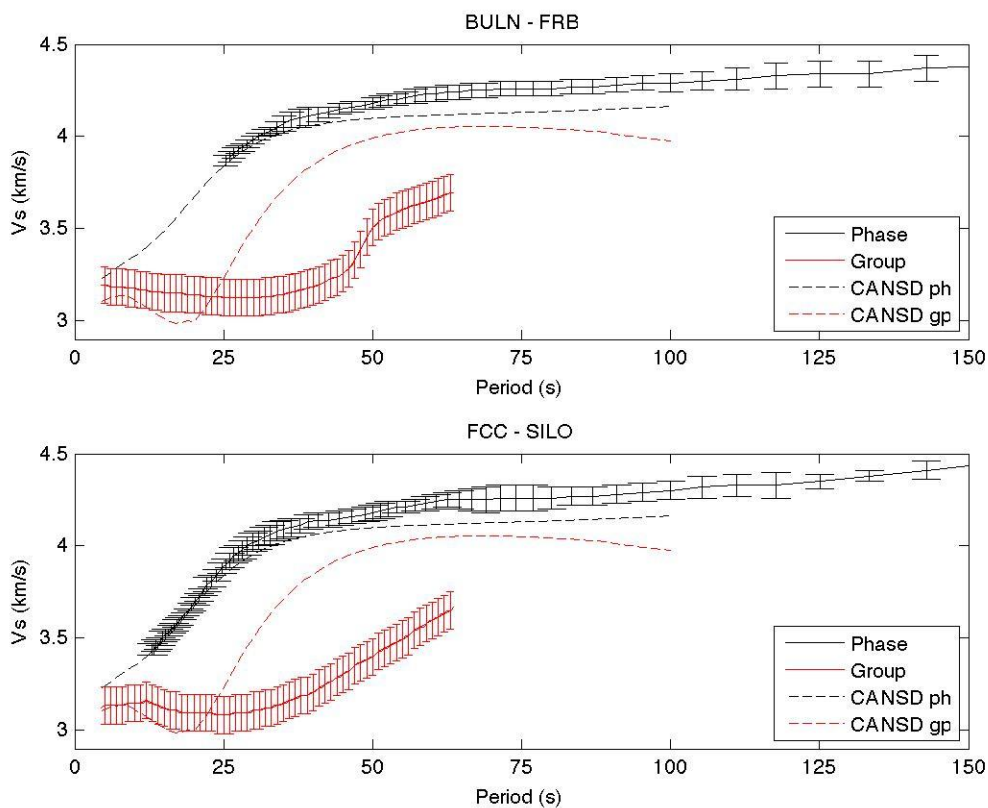


**Figure 4.8 Comparison of group and phase dispersion curves.**

Two-station dispersion curves for ambient-noise group-velocities and surface-wave phase-velocities compared with the CANSD reference model. The group-velocity measurement uncertainty is estimated here to be 0.1 km/s, based on the width of the peak defined by the dispersion ridge associated with the amplitude envelope (see Chapter 2).

Figure 4.8 shows several representative Rayleigh-wave group-velocity dispersion curves from ambient-noise data, together with Rayleigh-wave phase-velocity dispersion curves from surface waves. These are compared with reference velocities from the CANS model. Group velocities for the crust (5s – 20s) beneath Hudson Bay appear to be slightly fast compared with the CANS model. For periods greater than ~ 20s, however, the group velocities are anomalously slow. On the other hand, phase velocities from teleseismic surface-wave analysis are consistent with CANS up to approximately 35s period; above ~35s, phase velocities are faster than the CANS average. This discrepancy in the data, especially around 35s where group velocities are slower and phase velocities are faster than the CANS average, represents an incompatibility in the data for joint inversion. This discrepancy may arise from noise or uncertainties in the ambient-noise measurements. Understanding these possible incompatibilities, we proceed with caution.

The ambient-noise data has a denser path coverage (Figure 4.9a) than the surface-wave dataset (Figure 4.9b), understandably since ambient-noise tomography is not limited by earthquake locations as is the case for surface waves. However, we consider that the path coverage for both datasets for most of the Hudson Bay region is sufficient for the tomographic inversion undertaken here. The common path coverage means that the grid nodes (Figure 4.3) used in the inversion are also common for both datasets.

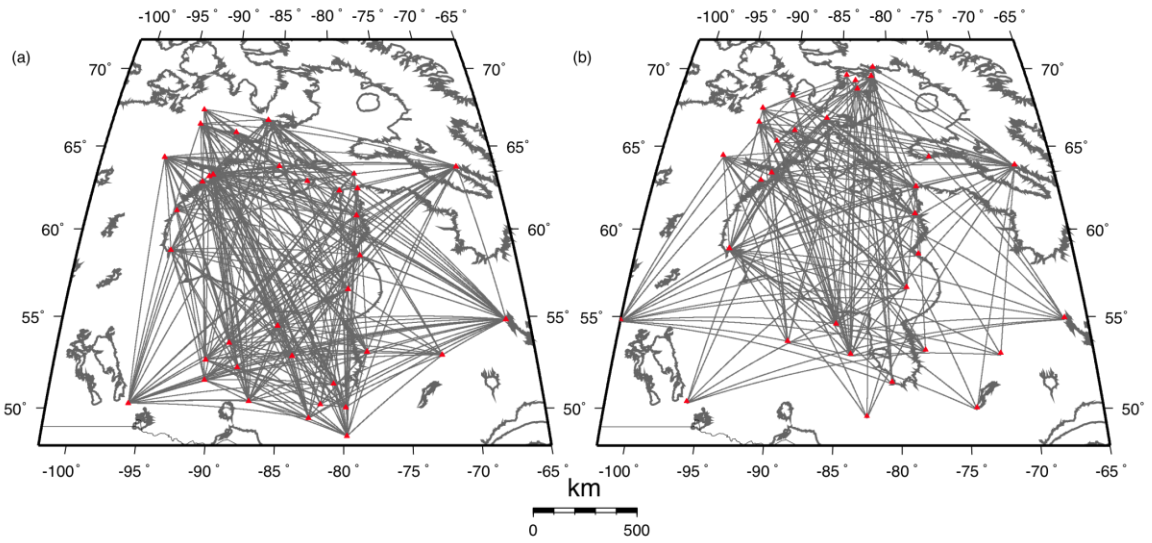


**Figure 4.9. Path density maps.**

Path-density maps for (a) ambient-noise data and (b) surface wave data.

## 4.8 1D models

### 4.8.1 Starting model parameterizations

The Monte-Carlo inversion requires a robust starting model to fit the data accurately. The model parameterization strongly affects the resultant mean model. If the inversion is weakly constrained, then there will be a large region of the model space that will fit the data, with large uncertainty. Tight constraints will reduce the uncertainty, but the model will be subject to systematic errors. With *a priori* knowledge from independent studies (Thompson et al., 2010; Pawlak et al., 2011; Darbyshire and Eaton, 2011), we tested 3 starting models, varying primarily in the crust, to find a good fit to both datasets and to avoid aphysical models.

The Monte-Carlo inversion tends to become unstable when over-parameterized; thus we used simple starting models. Our first starting model, denoted SM1, is defined by a three-layer crust, with fixed layer depths but varying velocities ( $\pm 10\%$ ) (Table 1). A constant  $v_p/v_s$  ratio of 1.73 was used, and the Moho was allowed to vary between 35 km and 50 km depth, consistent with observations from receiver-function analysis in this area (Thompson et al., 2010). The second starting model (denoted SM2) was similar to the first, but crustal layer thicknesses were allowed to vary by  $\pm 3$  km. All other parameters were the same as in SM1. Furthermore, both SM1 and SM2 contain a sharp boundary in the mid-crust, to test for a potential two-layer crust. The third starting model (denoted SM3) has a five-layer crust with fixed interface depths (Table 2). This model allows for the possibility of a more gradational velocity increase through the crust. The Moho was

also set between 35 km depth and 50 km depth. Additional models could have been tested; however, for simplicity and stability of the inversion process these three were chosen as representative for a realistic range of plausible crustal scenarios.

For all starting models, the mantle is parameterized using 5 cubic B-splines. There is no explicit constraint on mantle velocities, however the choice of B-splines implicitly constrains the velocities and imposes a degree of vertical smoothness (Shapiro and Ritzwoller, 2002). In addition to the constraints imposed on depth and velocity variation an error tolerance is imposed on how closely the synthetics must fit the data. An error tolerance of 0.03 km/s is used here.

| SM1/SM2        | Layer thickness | Vp<br>(km/s) | Density<br>(g/cc) | Vs<br>(km/s) | Vs range<br>(km/s) |
|----------------|-----------------|--------------|-------------------|--------------|--------------------|
| <b>Layer 1</b> | 15 km           | 6.03         | 2.70              | 3.48         | 3.132-3.828        |
| <b>Layer 2</b> | 15 km           | 6.27         | 2.78              | 3.62         | 3.258-3.982        |
| <b>Layer 3</b> | 5 – 20 km       | 6.41         | 2.82              | 3.70         | 3.330-4.070        |

**Table 4.1 – Crustal parameterization for SM1 with fixed layer depths. SM2 has the same values, however layer thickness is allowed to vary  $\pm 3$  km.**

| SM3            | Layer thickness | Vp<br>(km/s) | Density<br>(g/cc) | Vs<br>(km/s) | Vs range<br>(km/s) |
|----------------|-----------------|--------------|-------------------|--------------|--------------------|
| <b>Layer 1</b> | 7 km            | 6.03         | 2.70              | 3.48         | 3.132-3.828        |
| <b>Layer 2</b> | 8 km            | 6.15         | 2.74              | 3.55         | 3.195-3.905        |
| <b>Layer 3</b> | 7 km            | 6.27         | 2.78              | 3.62         | 3.258-3.982        |
| <b>Layer 4</b> | 8 km            | 6.34         | 2.80              | 3.66         | 3.294-4.026        |
| <b>Layer 5</b> | 5 – 20 km       | 6.41         | 2.82              | 3.70         | 3.330-4.070        |

**Table 4.2 – Crustal parameterization for SM3 with fixed layer depths.**

#### 4.8.2 1D depth profiles

Inversion results for the three starting models outlined in Table 1 and 2 are shown in Figure 4.10, at locations indicated in Figure 4.3. For each figure, the images on the left are the 1D models and on the right are the corresponding dispersion curves for both surface wave phase velocities and ambient-noise group velocities. The inversion results find the best possible fit between the two datasets. The mantle results are consistent through all starting models, showing that the ambient-noise data has little influence below the uppermost-mantle zone, as expected.

For each of the starting models we obtain a good fit to the group velocity for periods consistent with the upper crust ( $< 20$  s), and a similarly good fit to the phase velocity for periods consistent with the mantle ( $> 40$ s). The period range of overlap of the two datasets (20-40s) exhibits a significant discrepancy, however. The three starting models vary only in the crust to uppermost-mantle, whereas the mid-crust to uppermost-mantle depths are most influenced by the tradeoffs between both datasets. In particular, the inversion could not obtain an acceptable fit to the longer periods (35-40 s) in the ambient-noise group-velocity data, although a good fit was obtained for other periods.

The 5-layer model fits both datasets best visually, suggesting that a large velocity jump in the middle crust is not required to fit our dispersion data. Two nodes on either side of the suture (HBB and SUP Figure 4.3) have been chosen as representative for purposes of comparison to evaluate whether significant differences exist between these domains. North of the suture ('HBB'; Figure 4.3), there appears to be a noticeably higher degree of

layering in the crust as compared with the Superior craton ('SUP'). In addition, the result in 'SUP' exhibits a steeper velocity gradient than 'HBB'. All starting models converge toward solutions that contain a high-velocity mantle lid. The Moho was found, in general, to be at a depth of approximately 40 – 45 km, which is somewhat deeper than expected (~38 km). Resolution at this depth range is broad (Figure 4.6), however, and thus poorly constrained. Models using SM3 fit both phase and group velocity dispersion curves more consistently than the other two starting models, and thus the mean models created by SM3 are preferred and are used to create the 3D volume.

None of the starting models converged to solutions that provided a satisfactory fit to the ambient-noise group-velocity data above 25 s period. As elaborated in the next section, we interpret this misfit as evidence that the ambient-noise observations are unreliable within this period range. This period range of 'bad' data likely affects the inversion process, as it attempts to find models that fit mutually incompatible low group velocities and high phase velocities. To explore the effect of this 'bad' data we removed this period range to create a reduced dataset and inverted using the 5 layer starting model, or SM3. Removing this period range provided a better fit not just to the group velocities but also to the phase velocities and allowed us to use a smaller fit tolerance of 0.03. Results for sample areas 'HBB' and 'SUP' are shown in Figure 4.11, for comparison.

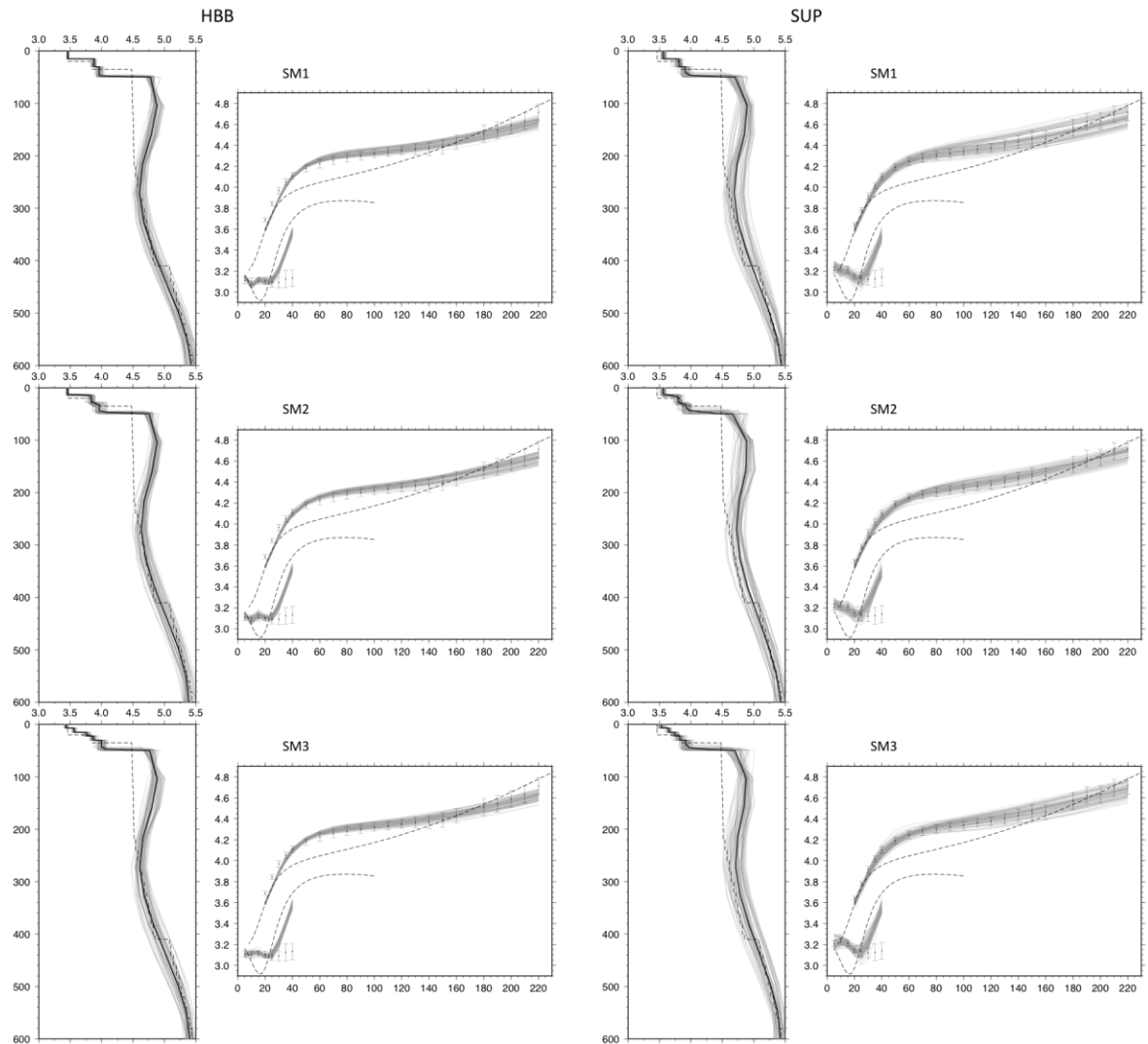


**Figure 4.10** 1D depth profiles.

1D inversion results at nodes shown in Figure 4.3. In the model results on the left, the grey lines represent 100 models that fit within a predefined tolerance against depth in km. The mean model is shown in black and *ak135* is indicated with the dashed line. On the right are corresponding dispersion curves, including the original group-velocity and phase-velocity dispersion curves (shown with error bars) and *ak135* (dashed lines).

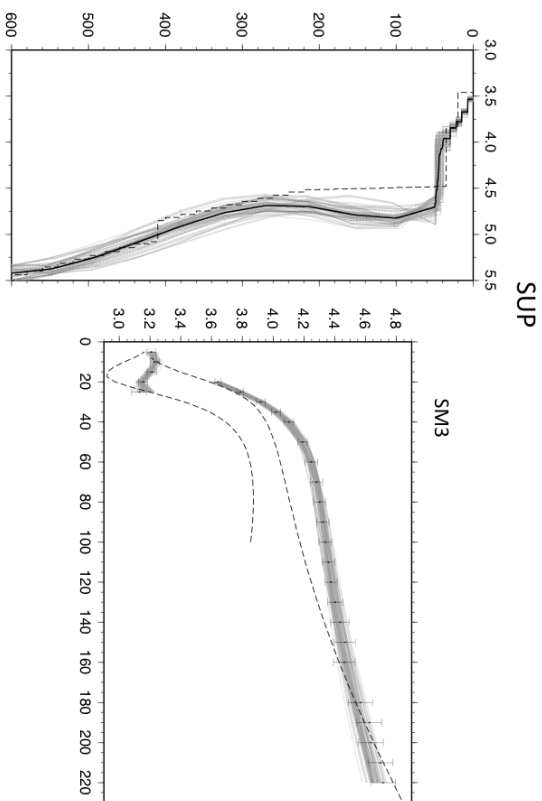
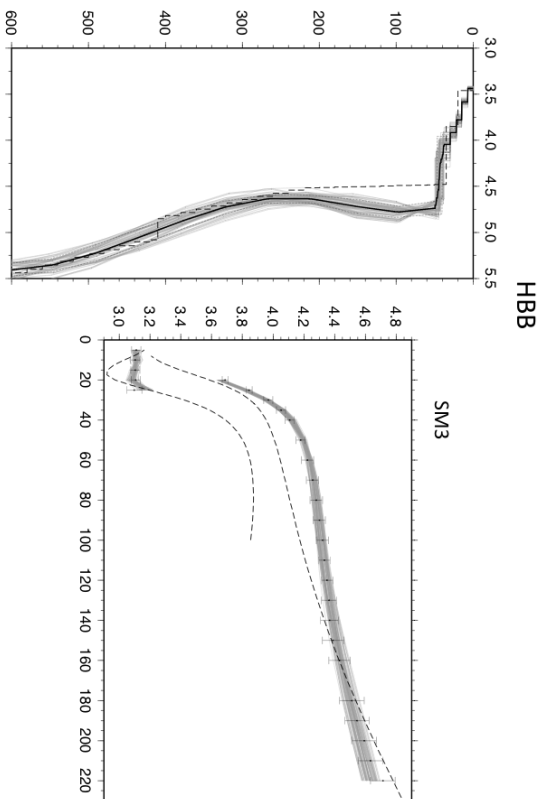


**Figure 4.11 1D depth profiles for reduced dataset.**

1D inversion results at nodes shown in Figure 4.3. Results are the same as Figure 4.6, however, ‘bad’ data in the period range 30 s to 40 s in the group velocity curve has been removed.

---

**4.9 Results**

After 1D depth profiles are inverted at each grid node using the Monte-Carlo procedure described above, the mean model at each point is used to plot depth slices through the crust and mantle (Figure 4.12). The colour scale for these depth slices represents perturbation from the regional average at a given depth (Figure 4.13). Regional averages are calculated as the mean at each node for a given depth slice. Results in the upper crust (~ 5 – 10 km) are generally consistent with results for isotropic velocities found by Pawlak et al. (2011). For example, we see lower velocities (in red) centered in the middle of Hudson Bay, roughly beneath the Hudson Bay basin (Figure 4.1). Higher velocities are found in the south and east, in horseshoe pattern that mimics the double-indentor shape of the Archean Superior craton (Figure 4.1). Moving down into the mid-crust (~15 – 25 km), the low-velocity region becomes smaller and shifts to the southeast. Relatively high-velocity regions occur to the north and south, approximately where the Superior and Churchill cratons occur (Figure 4.1). In the lower crust (~ 30 – 35 km), this low-velocity region becomes elongated in the east-west direction. In the Moho depth range (~ 39 – 45 km) the model becomes discontinuous and it is difficult to discern any specific features.

This depth range is poorly resolved and corresponds to the period band with incompatible data.

In the upper-mantle ( $\sim 50 - 80$  km), we find a low-velocity region that trends in the southwest - northeast direction, similar to the axis of the THO (Figure 4.1). Higher velocities exist to the northwest and to the southeast, again in the general regions of both cratons (Figure 4.1). At approximately 100 km depth, the two high-velocity regions merge, roughly beneath the centre of Hudson Bay.

A cross-section cutting through the centre of the Bay in a northwest – southeast direction (cross-section location shown in Figure 4.3) is shown in Figure 4.14. Figure 4.14b shows the same cross-section using the SM3 starting model, but with the reduced dataset. Here we can see that removing the incompatible ambient-noise velocities does not significantly change our results, however, it requires the upper to mid crust to be mainly constrained by ambient-noise data and the mantle to be constrained predominantly by surface wave data. At 120 km depth, there is a change in the amplitude of the velocity perturbation; this change could be an effect of the negative lobe of the sensitivity kernel. This leakage could occur because the  $\sim 30$  s group velocity sensitivity kernels would have a negative lobe centered around 130 km (compare 20 s and 40 s kernels in Figure 4.6).

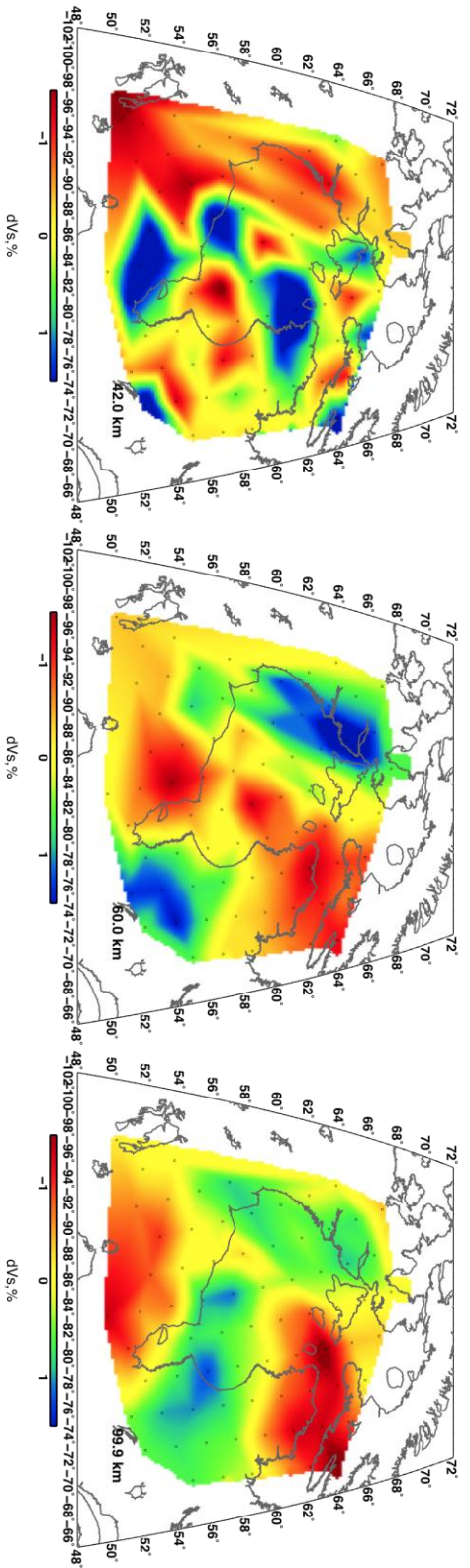
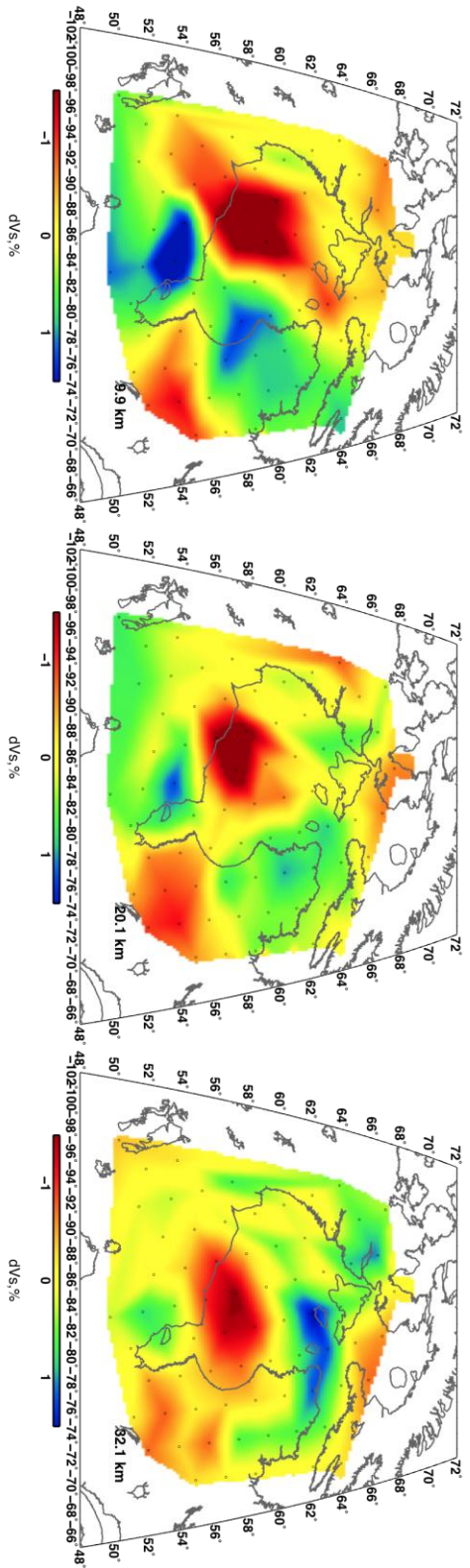


**Figure 4.12 Depth slices.**

Depth slices resulting from 1D depth profile mean models at every grid node (Figure 4.3).

---

**4.10 Discussion**

The motivation to invert the dataset with different starting models is to determine the best possible model fit that is consistent with two different datasets (ambient noise and surface wave). A related goal of the joint inversion is to test for possible layering in the crust and to understand the complicated tectonics in the vicinity of the THO suture zone. In this respect, the 1D depth profiles suggest some differences in crustal structure across the suture, such as evidence for a ~ 2-layer crust on the Churchill side of the suture but not on the Superior side of the suture (Figure 4.1). With the exception of a less-coherent depth region of the model near the Moho, the results of the joint inversion also provide a nearly continuous image from the crust into the mantle. Looking at the cross-section in Figure 4.14, it is evident that, although it manifests as apparent layering in the 1D profiles, this feature is actually a low-velocity zone that dips to the southeast in the crust. This feature appears to become subvertical within the underlying mantle.

As illustrated schematically in Figure 4.15, the low-velocity feature described above is located near the primary suture within the Trans Hudson orogen. Within the available resolution of our data, this suggests that younger (Paleoproterozoic) crust within the THO is characterized by significantly lower velocities than adjacent Archean regions. Viewed

broadly as representative of the suture zone, the geometry of the low-velocity feature provides potential insight into collisional assembly of the THO, and possibly also the formation of the Hudson Bay basin, which is situated more-or-less directly above it (Figure 4.1). In particular, the subvertical mantle suture appears to be offset from the overlying dipping suture zone within the crust. We interpret the mantle suture as a potential zone of weakness in the lithosphere. Such a weak zone may have provided a locus for subsequent initiation of localized lithospheric stretching that resulted in formation of the Hudson Bay basin (Kearey et al., 2009).

We note that it is unlikely that the low-velocity feature is an artefact of “leakage” associated with the group-velocity sensitivity kernels, as such features are expected to have reversed polarity in the mantle relative to the crust. This reverse polarity is due to the existence of paired positive and negative lobes for the group-velocity sensitivity kernels.

Finally, the period band of ‘bad’ data in the ambient-noise observations warrants further comment. This frequency range falls outside the primary and secondary microseismic noise peaks discussed in Chapter 1. Consequently, this period range represents a relative ‘dead’ zone within the source spectrum that generates Rayleigh waves that are used in the inversion. In addition to being of low amplitude, in longer period data there is weaker scattering and so the ambient-noise data is less diffuse (Stehly et al., 2006), violating a major assumption of ambient-noise analysis. For robust longer period data, longer time-series are required (Stehly et al., 2006).

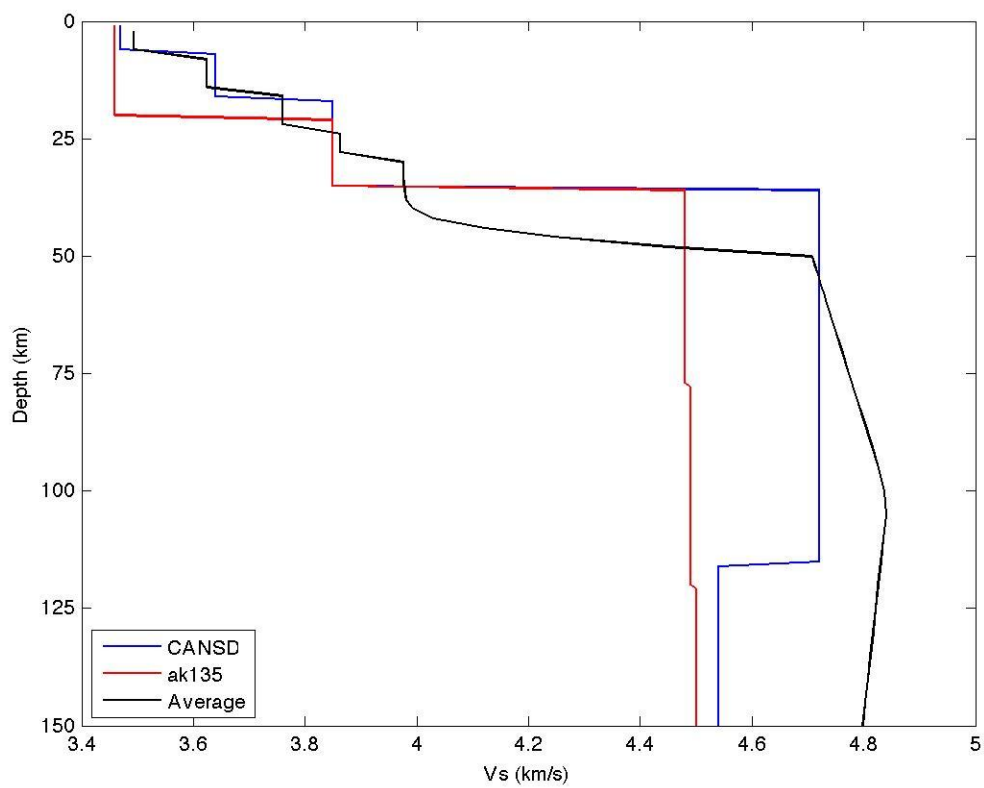


**Figure 4.13. Regional average curve.**

Regional average 1D velocity model obtained for all inversion nodes, compared with *ak135* and CANSD Earth models.

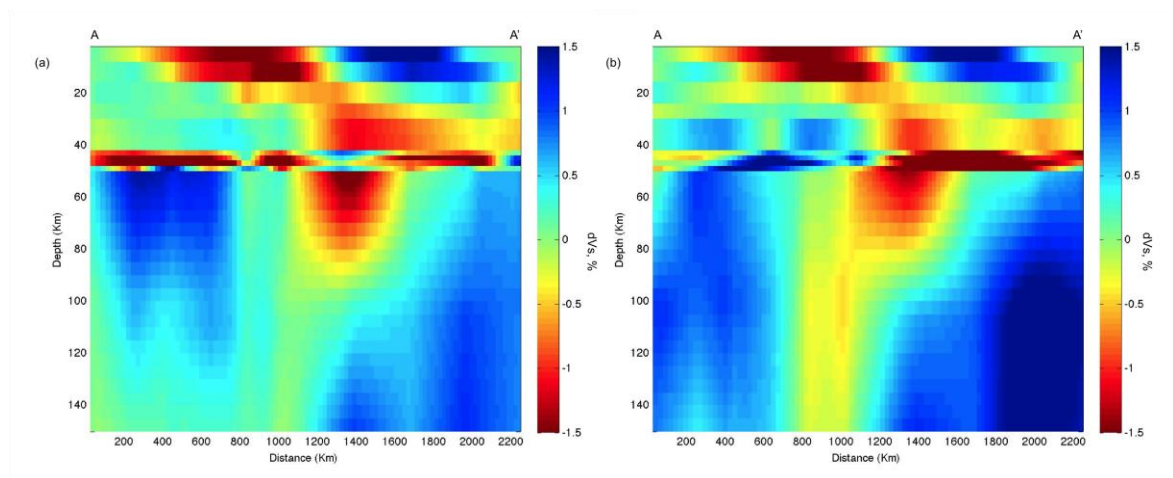


**Figure 4.14. Cross-sections.**

Cross-section at location shown in Figure 4.3, (a) all ambient-noise data included, (b) removed ambient-noise data greater than 30 s period. Color scale is % perturbation from the regional average (Figure 4.13) for a given depth. Results show that removing ‘bad’ points (b) does not significantly change the inversion. The THO suture zone is expressed in this model as a low-velocity zone that dips to the SE within the crust, becoming near vertical in the underlying lithospheric mantle.

## 4.11 Conclusions

In this chapter, Rayleigh-wave group-velocity dispersion measurements from ambient-noise data and phase-velocity dispersion measurements from teleseismic surface-wave analysis are combined and jointly inverted to estimate the shear-wave velocity structure of the crust and upper mantle. Phase velocities computed from the ambient noise data are compared with reference models and previously calculated group-velocity dispersion. Inversion depth sensitivity is explored for model CANSND by considering partial derivatives of Rayleigh phase and group velocity with respect to model parameters. Although group-velocity sensitivity is generally less desirable for inversion due to the existence of positive and negative lobes that could produce “leakage”, we prefer the group velocities due to uncertainty with the inherent ambiguity term associated with phase unwrapping. Comparison of phase-velocity dispersion results from surface-wave analysis with group-velocity dispersion results from ambient-noise tomography suggests that these two types of data may be mutually incompatible for inversion for periods between 30-40s. Since this is a ‘dead’ zone for ambient-noise sources, we have considered inversions that either include or exclude ambient noise data within this frequency band.

Joint inversion of both datasets is carried using a Monte Carlo approach, based on 3 different starting models that span a plausible diversity of crustal models for this region. A 1D depth inversion is then applied to the mean model arising from this methodology. Our results provide evidence for differences in crustal velocity structure on either side of the primary suture within the THO. Depth slices for the full inversion dataset exhibit

regional patterns, including an area of low velocity within the mid-crust beneath Hudson Bay, that are similar to previous results of Pawlak et al. (2010; 2011). A cross-section that spans the suture reveals a dipping low-velocity zone (i.e., relative to high-velocity regions in the adjacent Archean cratons) in the crust that appears to become subvertical in the underlying upper mantle. If this feature within the THO represents a persistent zone of weakness, it may have formed a locus for initiation of lithospheric stretching that may have resulted in formation of the Hudson Bay basin.

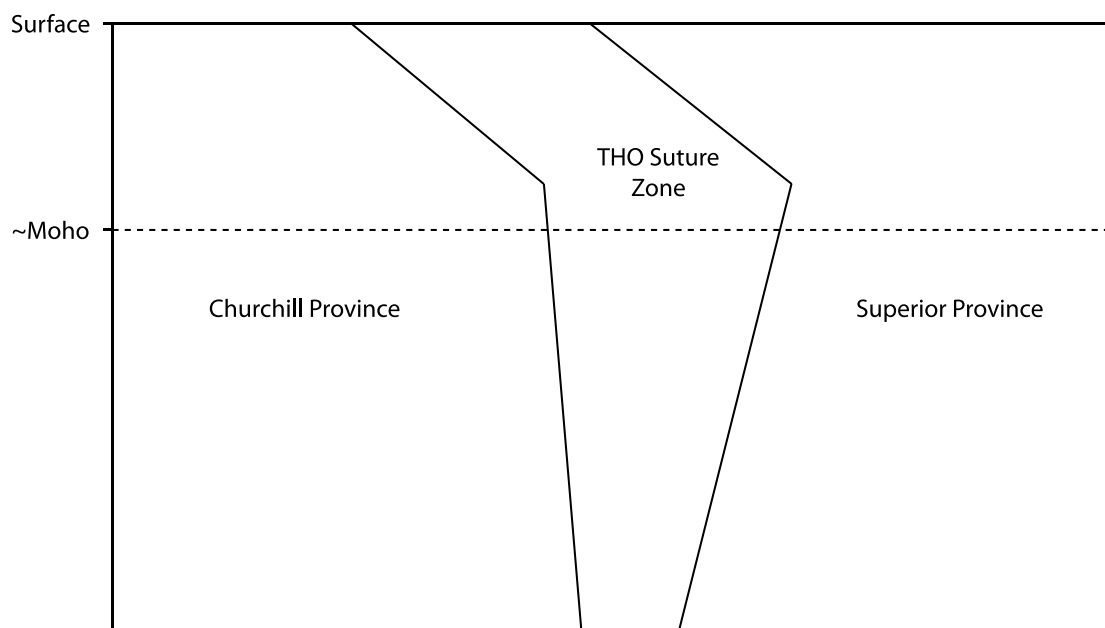


**Figure 4.15. Schematic cross section showing inferred THO suture geometry.**

Interpretive cross-section derived from the velocity model in Figure 4.14.

## Chapter Five: **CONCLUSIONS**

The goals of this study are to apply ambient-noise tomography, a relatively new methodology for imaging the crust to upper-most mantle, to investigate complicated lithospheric structure in the Hudson Bay region. This work is part of large project entitled the Hudson Bay Lithospheric Experiment (HuBLE), which is a multi-disciplinary collaborative project aimed at understanding the subsurface beneath Hudson Bay. Here, we have successfully applied this method and developed improvements to some elements of the processing methodology. Through three different studies, we have also successfully contributed to a more complete understanding of the lithospheric evolution of the Hudson Bay region. In the first study, the use of an isotropic inversion (i.e. an inversion that solves for only isotropic velocities and does not account for azimuthal change in velocity) has improved the resolution of the subsurface and has provided evidence to support a hypothesis for basin formation and to invalidate another hypothesis. In our second study, anisotropic results have further constrained the structure and we can now infer the geologic age of some of the fabrics. In our third study, joint inversion with surface waves has yielded an image that extends deeper than previous studies, from the crust into the upper mantle. Below, we summarize the three approaches we used here to

develop a better understanding of geologic implications and in doing so, enhance the methodology of ambient-noise tomography. Next we discuss the major contribution this thesis has made to the seismological community. Finally, we look at some of the directions that future studies can take that could potentially branch off from this study.

## **5.1 Summary of Thesis Work**

### *5.1.1 Isotropic crustal structure and ambient noise sources*

We have investigated the crustal structure beneath Hudson Bay using 21 months of continuous recordings from 37 broad-band seismograph stations located around the Bay. The raw data consists of three-component measurements of ground motion. To process this data, we windowed the entire continuous recording to create a set of one-day records, and resampled to 1 Hz. Daily trends, mean, and instrument response were removed from the record. A one-bit time normalization procedure was applied to remove earthquake signals and instrument irregularities, followed by spectral normalization to broaden the frequency range. The signal remaining from the processing stage is inferred to contain ambient-noise signals generated by the Earth, more specifically, ocean waves interacting with coastlines.

The signals are then cross-correlated for all possible station pairs and all available daily records are stacked. The cross-correlation process yields an empirical Green's function characterized by causal and acausal lags. Theoretical studies (Shapiro et al., 2005) show that if noise sources were distributed homogeneously in azimuth around the two stations then the causal and acausal signal would be approximately equal. We find, however, a

strong asymmetry in the signals, suggesting that in practice the stacking of causal and acausal lags may not be desirable. Commonly, the two-sides of the correlation are averaged to yield the empirical Green's function (EGF). This averaging is expected to increase SNR by a factor of  $\sqrt{2}$  assuming Gaussian random noise and identical signal components. Given the asymmetry in the correlation signals, we adopted a one-sided empirical Green's function method, taking either the causal or (time-reversed) acausal signal with the higher absolute SNR. Fundamental-mode Rayleigh wave group-velocity dispersion curves are estimated from the EGFs using frequency-time analysis. The dispersion curves are then inverted for shear-wave velocity structure.

We examined noise source locations by plotting signal to noise ratio (SNR) versus azimuth. This analysis also showed us that Hudson Bay is relatively quiet and that dominant noise sources are generated in the Atlantic Ocean and Labrador Sea in the east, the southern Alaska region in the west and a weak source from the Canadian Arctic coast. Furthermore, we examined the seasonality of the eastern and western sources, showing that only slight variation exists between the summer and winter, but that there is a significant dependence on period. The period variation of noise sources is consistent with the interpretation that primary (10–20 s) and secondary (5–10 s) micro-seismic bands reflect acoustic-elastic coupling of ocean swells with the continental shelf.

Results showed that the centre of Hudson Bay has relatively lower isotropic Rayleigh-wave velocity than the surrounding regions. Furthermore, we tested two competing hypotheses for the formation of the Hudson Bay basin, each defined by a different character in the lower crust. We concluded that there was evidence for crustal thinning

beneath the centre of the basin, supporting the hypothesis for lithospheric extension creating subsidence (Hanne et al., 2004) and, in turn, forming the sedimentary basin. An alternative hypothesis that the basin formed from flexural response to lower-crustal eclogite transformation (Eaton and Darbyshire, 2010) predicts crustal thickening that is inconsistent with our results.

### *5.1.2 Anisotropic structure*

Once we completed the isotropic analysis, we took the same dataset and analysed it for azimuthally anisotropic structure. Anisotropic analysis using solely ambient-noise data is uncommon and has only recently been published by other groups (Yao and van der Hilst, 2009; Gallego et al., 2011). Inversion of the group-velocity dispersion curves for isotropic and anisotropic velocities was performed using a methodology used commonly for teleseismic surface wave analysis. For weak anisotropy, the inversion problem for group-velocity perturbation is parameterized with five unknowns, one isotropic term and four anisotropic terms. The four anisotropic terms break down to two terms defining  $2\Psi$  anisotropy and two terms defining  $4\Psi$  anisotropy. Terms that define  $2\Psi$  and  $4\Psi$  anisotropy account for azimuthal variations of group velocity that exhibit a periodicity of  $\pi$  and  $\pi/2$  radians, respectively. Five possible geologic scenarios are considered (Figure 3.5) that could generate some combination of  $2\Psi$  and  $4\Psi$  anisotropy.

Being one of the first studies to invert for azimuthal anisotropy with just ambient-noise data, we performed extensive resolution testing of inversion parameters. Isotropic results revealed a relatively low-velocity region in the centre of the Bay compared with the surrounding regions, consistent with our previous isotropic study. The crust was found to

be weakly anisotropic. Anisotropic patterns in the upper to mid-crust (10-20 s period, or ~10-20 km) mimic large-scale tectonic structures known from regional geologic maps, namely the outline of the Superior craton. The difference in anisotropic pattern on either side of the Trans-Hudson Orogen (THO) suture zone is significant, and suggests that the structural fabrics revealed from our analysis formed prior to collision of the Churchill and Superior cratons. The lower crust (25-35 s period, or ~25-35 km depth) exhibits distinctive anisotropic fabrics manifested by a N-S predominant pattern. We interpret this pattern as potential channel flow that post dates the collision between the Churchill and Superior cratons. The flow propagates through a channel zone in a weak lower crust at a rate driven by temperature, viscosity and horizontal pressure gradient [*Beaumont et al.*, 2001; *Clark et al.*, 2005].

### *5.1.3 Joint Inversion of Ambient Noise and Surface Waves*

To improve the resolution and to gain a better image of the crust and mantle beneath Hudson Bay, we jointly inverted ambient-noise data with surface-wave data from teleseismic earthquakes. Due to the frequency content (20 - 160 s period, or 0.00625 - 0.05 Hz), surface-wave data is generally more sensitive to velocity structure of the lower crust to mid-mantle. This region of sensitivity overlaps with ambient-noise tomography in the lower crust. Thus, the joint inversion of these two datasets allows us to obtain a more coherent image of the subsurface. 1D phase-velocity dispersion curves are extracted from surface wave data and 1D group velocity dispersion curves are extracted from the ambient-noise data. Sensitivity kernels show group and phase velocities sample similar

depth ranges, although the phase-velocity sensitivity kernels exhibit a less complex depth distribution that is more desirable for inversion.

For this reason, inversion of phase velocity data is preferred. For our ambient-noise data, the phase velocities had significant uncertainty with the  $N$  ambiguity which made the group velocities more robust in this case. To invert phase-velocity dispersion (earthquakes) and group-velocity dispersion (ambient-noise) simultaneously, we use a Monte Carlo procedure. Results show that the THO suture zone is manifested in the mantle as a near-vertical low velocity band. This gives us further insight into the formation of the Hudson Bay basin, which is situated directly above this low-velocity region. We interpret the suture as a zone of weakness that extends through the lithosphere, potentially providing a locus for initiation of localized lithospheric stretching.

## **5.2 General Contributions**

Perhaps the most significant contribution of this study has been the increased resolution and new insights into the subsurface beneath Hudson Bay. We have been able to choose between competing models for basin formation and have found evidence for crustal thinning by lithospheric stretching. With the joint inversion with surface waves, we have further increased the resolution of the crust and mantle, delineating a low-velocity band that could represent a zone of weakness beneath the basin, further supporting possible lithospheric stretching.

This work is also one of the first studies to analyse azimuthal anisotropy with just ambient-noise data for input into the inversion. Since this is not a well established approach, we have undertaken extensive resolution and parameter testing to understand the robustness of the results. We test smoothing and damping parameters for both isotropic and  $2\Psi$  anisotropy model parameters to evaluate the significance of leakage between parameters. We provide new evidence for a divide in anisotropic fabrics that are juxtaposed across the THO suture zone. This relationship allows us to date the crustal fabrics to infer that formation of these fabrics predates the creation of the suture during terminal collision.

Additionally, we have found a strong asymmetry in our empirical Green's functions computed using our dataset. This has allowed us to infer the location of coastal point sources of noise that strongly vary with period. This is the first study to identify coastal sources of Rayleigh waves in northern North America. This also has motivated us to improve the ambient-noise tomography processing method to accommodate asymmetric correlation signals, which are commonly reported by other researchers (Stehly et al., 2006).

### **5.3 Future Work**

As with most studies, new discoveries are accompanied by new questions. An obvious next step emerging from this study could involve joint inversion with surface waves, similar to the approach described in Chapter Four but including the effects of azimuthal anisotropy. Similar to the results in Chapter Four, doing so, would allow us to add more

constraints on the anisotropic fabrics especially with respect to the lower crust. Additionally, our dataset alone was not able to resolve any meaningful  $4\Psi$  crustal anisotropy, however, adding more data may be useful to explore any potential  $4\Psi$  features, since the presence of  $4\Psi$  anisotropy is predicted by various geologic scenarios (Figure 3.5).

This study made use of only the vertical component recordings of ground motion. To further understand the subsurface beneath Hudson Bay it would be beneficial to examine the transverse and radial components of the data. Doing this would introduce Love waves and radial anisotropy. Love waves are guided modes resulting from horizontally polarized shear waves whereas Rayleigh waves result from the combination of P waves and vertically polarized shear waves. Since the sensitivity of Love waves is shallower than Rayleigh waves, adding these two wave components into the equation would be expected to provide additional constraint that should improve the structural imaging. Furthermore, radially anisotropic velocity structure is a proxy for strain in the crust and mantle and is measured as the ratio of horizontally to vertically polarized shear velocity.

Finally, adding ocean bottom seismometers (OBS) would greatly increase the resolving potential of ambient-noise tomography. Adding seismometers in the centre of the Bay would increase area coverage, eliminating some uncertainty in our results. However, logistically this is a challenge as the Bay is frozen half the year. Additionally, carrying out a controlled source seismic survey would be complimentary to this passive source study. Using a controlled source, similar to Lithoprobe, we would have the potential to carry out seismic reflection and refraction surveys. A reflection survey would help with

the understanding of subsurface structure, namely outline the Moho better, and a refraction survey would help constrain velocities. Both would add more detail into the imaging potential and would provide useful additional constrains for interpretation.

## References

- Audoine, E. L., M. K. Savage, and K. R. Gledhill, 2004. Anisotropic structure under a back-arc spreading region, the Taupo Volcanic Zone, New Zealand, *J. Geophys. Res.* 109, B11305, doi:10.1029/2003JB002932.
- Barmin, M.P., Ritzwoller, M.H. and Levshin, A.L., 2001. A fast and reliable method for surface wave tomography, *Pure Appl. Geophys.*, 158, 1351 – 1375.
- Barruol, G., and D., Mainprice, 1993. 3-D seismic velocities calculated from lattice-preferred orientation and reflectivity of a lower crustal section: examples of the Val Sesia section (Ivrea zone, northern Italy), *Geophys. J. Int.*, 115, 1169-1188.
- Bastow, I.D., D. Thompson, J. Wookey, J.M. Kendall, G. Helffrich, D. Snyder, D.W. Eaton, and F.A. Darbyshire, 2011. Precambrian plate tectonics: Seismic evidence from northern Hudson Bay, Canada, *Geology*, 39, 91-94, doi:10.1130/G31396.1.
- Beaumont, C., R.A. Jamieson, M.H. Nguyen, and B. Lee, 2001. Himalayan tectonics explained by extrusion of a low-viscosity crustal channel coupled to focused surface denudation, *Nature*, 414, 738-742.
- Beck, A.E., 1991. *Physical properties of Exploration Methods*, Second Edition. Wuerz Publishing Ltd.
- Bensen, G.D., M.H. Ritzwoller, M.P. Barmin, A.L. Levshin, F.C. Lin, M.P. Moschetti, N.M. Shapiro, and Y. Yang, 2007. Processing seismic ambient noise data to

obtain reliable broad-band surface wave dispersion measurements, *Geophys. J. Int.*, 169, 1351-1375, doi:10.1111/j.1365-246X.2007.03374.x.

Bensen, G.D., R.H. Ritzwoller, and Y. Yang, 2009. A 3D shear velocity model of the crust and uppermost mantle beneath the United States from ambient seismic noise, *Geophys. J. Int.*, 177, 1177–1196, doi:10.1111/j.1365-246X.2009.04125.x.

Berman, R.G., M. Sanborn-Barrie, R.A. Stern, and C.J. Carson, 2005. Tectonometamorphism at ca. 2.35 and 1.85 Ga in the Rae domain, Western Churchill Province, Nunavut, Canada, insights from structural, metamorphic and in situ geochronological analysis of the southwestern Committee Bay belt, *The Canadian Mineralogist*, 43, 409-442.

Bickford, M.E., K.D. Collerson, J.F. Lewry, W.R. Van Schmus, and J.R. Chiarenzelli, 1990. Proterozoic collisional tectonism in the Trans-Hudson Orogen, Saskatchewan, *Geology* 18, 14–18.

Bjornerud, M.G., H. Austreheim, and M.G. Lund, 2002. Processes leading to eclogitization (densification) of subducted and tectonically buried crust, *J. Geophys. Res.*, 107(B10), 2252, doi:10.1029/2001JB000527.

Bokelmann, G.H.R., and A. Wüstefeld, 2009. Comparing crustal and mantle fabric from the North American craton using magnetics and seismic anisotropy, *Earth Planet. Sci. Lett.*, 277 (3-4), 355-364, doi:10.1016/j.epsl.2008.10.032.

- Bott, M.H.P., 1999. Modeling local crustal isostasy caused by ductile flow in the lower crust, *J. Geophys. Res.*, 104, 20349-20359.
- Brocher, T.M., and N.I. Christensen, 1990. Seismic anisotropy due to preferred mineral orientation observed in shallow crustal rocks in southern Alaska, *Geology*, 18, 737-740.
- Brune, J., and J. Dorman, 1963. Seismic waves and Earth structure in the Canadian Shield, *Bull. Seism. Soc. Am.*, 53, 167-210.
- Burden, E.T., and A.B. Langille, 1990. Stratigraphy and sedimentology of Cretaceous and Paleocene strata in half-grabens on the southeast coast of Baffin Island, *Bull. Can. Pet. Geol.*, 38, 185-196.
- Campillo, M., and A. Paul, 2003. Long-range correlations in the diffuse seismic coda, *Science*, 299, 547, doi:10.1126/science.1078551.
- Capon, J., 1973. Analysis of microseismic noise at LASA, NORSAR and ALPA. *Geophys. J. R. astr. Soc.*, 35, 39-54.
- Chernick, M. R., 1999. *Bootstrap methods: A practitioner's guide*. Wiley, New York. 264 pp.
- Christensen, N.I., and W.D. Mooney, 1995. Seismic velocity structure and composition of the continental crust: A global view, *J. Geophys. Res.*, 100, 9761-9788.

Clark, M.K., and L.H. Royden, 2000. Topographic ooze: Building the eastern margin of Tibet by lower crustal flow, *Geology*, 28, 703-706, doi:10.1130/0091-7613(2000)28<703:TOBTEM>2.0.CO;2.

Clark, M.K., J.W.M. Bush, and L.H. Royden, 2005. Dynamic topography produced by lower crustal flow against rheological strength heterogeneities bordering the Tibetan Plateau, *Geophys. J. Int.*, 162, 575-590, doi:10.1111/j.1365-246X.2005.02580.x.

Clark, P.U., A.S. Dyke, J.D. Shakun, A.E. Carlson, J. Clark, B. Wohlfarth, J.X. Mitrovica, S.W. Hostetler, and A.M. McCabe, 2009. The Last Glacial Maximum, *Science*, 325, 710-714.

Clowes, R., Cook, F., Green, A.G., Keen, C.E., Ludden, J.N., Percival, J.A., Quinlan, G.M., West, G.F., 1992. Lithoprobe; new perspective on crustal evolution. *Canadian Journal of Earth Sciences*, 29, 1813-1864.

Cornett, A. and Zhang, J., 2008. Nearshore Wave Energy Resources, Western Vancouver Island, B.C., Technical Report CHC-TR-51.

Corrigan, D., Z. Hajnal, B. Németh, and S.B. Lucas, 2005. Tectonic framework of a Paleoproterozoic arc-continent to continent-continent collisional zone, Trans-Hudson Orogen, from geological and seismic reflection studies, *Can. J. Earth Sci.*, 42, 421-434.

- Corrigan, D., S. Pehrsson, N. Wodicka, and E. de Kemp, 2010. The Palaeoproterozoic Trans-Hudson Orogen: a prototype of modern accretionary processes, Geological Society, London, Special Publications, 327, 457-479.
- Crampin, S., 1981. A review of wave motion in anisotropic and cracked elastic-media, *Wave Motion* 3, 343-391.
- Crampin, S., E.M., Chesnokov, and R.G., Hipkin, 1984. Seismic anisotropy – the state of the art: II, *Geophys. J. R. astr. Soc.*, 76, 1-16.
- Crampin, S., 1987. Geological and industrial implications of extensive-dilatancy anisotropy, *Nature*, 328, 491-496.
- Crampin, S., 1994. The fracture criticality of crustal rocks, *Geophys. J. Int.*, 118, 428-438.
- Curtis, A., P. Gerstoft, H. Sato, R. Snieder, and K. Wapenaar, 2006. Seismic interferometry – turning noise into signal, *The Leading Edge*, 1082-1092.
- Dalton, C.A., J.B. Gaherty, and A.M. Courtier, 2011. Crustal Vs structure in northeastern Canada: Imaging the Cordillera-craton transition with ambient noise tomography, *J. Geophys. Res.*, 116, doi:10.1029/2011JB008499.
- Darbyshire, F.A., Eaton, D.W., Frederiksen A.W. and Ertolahti, L., 2007. New insights into the lithosphere beneath the Superior Province from Rayleigh wave dispersion and receiver function analysis, *Geophys. J. Int.*, 169, 1043-1068.

- Darbyshire, F.A., and S. Lebedev, 2009. Rayleigh wave phase-velocity heterogeneity and multilayered azimuthal anisotropy of the Superior Craton, Ontario, *Geophys. J. Int.*, 176, 215-234, doi:10.1111/j.1365-246X.2008.03982.x.
- Darbyshire, F.A., and D.W. Eaton, 2010. The lithospheric root beneath Hudson Bay, Canada from Rayleigh-wave dispersion: No clear seismological distinction between Archean and Proterozoic mantle, *Lithos*, doi:10.1016/j.lithos.2010.04.010.
- Darbyshire, F.A., D.W. Eaton, and I.D. Bastow, 2012. 3D lithospheric structure and azimuthal anisotropy beneath Hudson Bay from Rayleigh wave tomography, *Earth Planet. Sci. Lett.*, submitted.
- Davis, W.J., 1997. U-Pb zircon and rutile ages from granulite xenoliths in the Slave province: Evidence for mafic magmatism in the lower crust coincident with Proterozoic dike swarms, *Geology*, 25, 343-346, doi: 10.1130/0091-7613(1997)025.
- Deschamps, F., S. Lebedev, T. Meier, and J. Trampert, 2008. Azimuthal anisotropy of Rayleigh-wave phase velocities in the east-central United States, *Geophys. J. Int.*, 173, 827-843, doi:10.1111/j.1365-246X.2008.03751.x.
- Drulea, M., I.R. Peter, and S. Nedevschi, 2010. Optical flow A combined local-global approach using L1 norm, *Intelligent Computer Communication and Processing*, doi:10.1109/ICCP.2010.5606437.

- Duvall, T.L., S.M. Jefferies, J.W. Harvey, and M.A. Pomerantz, 1993. Time-distance helioseismology, *Nature*, 362, 430-432.
- Dyke, A.S., 2003. An outline of North American Deglaciation with emphasis on central and northern Canada, In: Ehlers, J. (Ed.), *Extent and Chronology of Quaternary Glaciation*. Elsevier.
- Eaton, D.W., F.A. Darbyshire, R.L. Evans, H. Grutter, A.G. Jones, and X. Yuan, 2009. The elusive lithosphere-asthenosphere boundary (LAB) beneath cratons, *Lithos.*, 109, 1-22.
- Eaton, D.W., and F.A. Darbyshire, 2010. Lithospheric architecture and tectonic evolution of the Hudson Bay region, *Tectonophysics*, 480, 1-22, doi:10.1016/j.tecto.2009.09.006.
- Endrun, B., S. Lebedev, T. Meier, C. Tirel, and W. Friederich, 2011. Complex layered deformation within the Aegean crust and mantle revealed by seismic anisotropy, *Nature Geosci*, 4, 203-207, doi:10.1038/ngeo1065.
- Fowler, C.M.R. and E.G. Nisbet, 1985. The subsidence of the Williston Basin, *Can. J. Earth Sci.*, 22, 408 – 415.
- Frederiksen, A.W., S.-K. Miong, F.A. Darbyshire, D.W. Eaton, S. Rondenay, and S. Sol, 2007. Lithospheric variations across the Superior Province, Ontario, Canada: Evidence from tomography and shear wave splitting, *J. Geophys. Res.*, 112, doi:10.1029/2006JB004861.

- Fry, B., F. Deschamps, E. Kissling, L. Stehly, and D. Giardini, 2010. Layered azimuthal anisotropy of Rayleigh wave phase velocities in the European Alpine lithosphere inferred from ambient noise, *Earth Planet. Sci. Lett.*, 297, 95-102, doi:10.1016/j.epsl.2010.06.008.
- Gaherty, J.B., 2004. A surface wave analysis of seismic anisotropy beneath eastern North America, *Geophys. J. Int.*, doi:10.1111/j.1365-246X.2004.02371.x.
- Gallego, A., M.P. Panning, R.M. Russo, V.I. Mocanu, R.E. Murdie, and J.C. Vandecar, 2011. Azimuthal anisotropy in the Chile Ridge subduction region retrieved from ambient noise, *Lithos*, 3, 393-400, doi: 10.1130/L139.1.
- Gay, S.P., 1973. Pervasive orthogonal fracturing in the Earth's continental crust, American Stereo Map Co, Salt Lake City, UT.
- Gibb, R.A., 1983. Model for suturing of Superior and Churchill plates: an example of double-indentation tectonics, *Geology*, 11, 413-417.
- Gilles, P.M., T.L. Duvall, P.H. Scherrer, and R.S. Bogart, 1997. Subsurface flow of material from the Sun equator's to its poles, *Nature*, 390, 63-64.
- GSC, 2010. Canadian Aeromagnetic Data Base, Airborne Geophysics Section, GSC - Central Canada Division, Geological Survey of Canada, Earth Sciences Sector, Natural Resources Canada Contact:  
[http://gdcinfo.agg.nrcan.gc.ca/contact\\_e.html#DataCentre](http://gdcinfo.agg.nrcan.gc.ca/contact_e.html#DataCentre).

- Hajnal, Z., J.F. Lewry, D.J. White, K. Ashton, R.M. Clowes, M. Stauffer, I. Gyorfi, and E. Takacs, 2005. The Sask Craton and Hearne Province margin: seismic reflection studies in the western Trans-Hudson Orogen, *Can. J. Earth Sci.*, 42,403-419, doi:10.1139/E05-026.
- Hamdani, Y., J.-C. Mareschal, and J. Arkani-Hamed, 1991. Phase changes and thermal subsidence in intracratonic sedimentary basins, *Geophys. J. Int.*, 106, 657-665.
- Hanmer, S., H.A Sandeman, W.J. Davis, L.B. Aspler, R.H. Rainbird, J.J. Ryan, C. Relf, and T.D. Peterson, 2004. Geology and Neoproterozoic tectonic setting of the Central Hearne supracrustal belt, Western Churchill Province, Nunavut, Canada, *Precambrian Research* 134, 63-83.
- Hanne, D., N., White, A., Butler and S., Jones, 2004. Phanerozoic vertical motions of Hudson Bay, *Can. J. Earth Sci.*, 41, 1181-1200.
- Heidbach, O., M. Tingay, A. Barth, J. Reinecker, D. KerfeB and B. Muller, 2008. The World Stress Map database release 2008, doi:10.1594/GFZWSSM.Rel2008.
- Hennino, R., N. Tregoures, N.M Shapiro, L. Margerin, M. Campillo, B.A. van Tiggelen, and R.L. Weaver, 2001. Observation of equipartition of seismic waves, *Phys. Res. Lett.*, 86, 3447-3450.
- Herrman, R.B., and C.J. Ammon, 2002. Computer programs in Seismology: Surface Waves, Receiver Functions and Crustal Structure, Vol.3.20., St. Louis University.

- Hobson, G.D., 1967. Hudson Bay crustal seismic experiment: time and distance data. *Canadian Journal of Earth Sciences*, 4, 879-899.
- Hoffman, P.F., 1988. United plates of America, the birth of a craton: Early Proterozoic assembly and growth of Laurentia, *Ann. Rev. Earth. Planet. Sci.*, 16, 543-603.
- Hoffman, P.F., 1990. Subdivision of the Churchill Province and extent of the Trans-Hudson Orogen, in, eds., *The Early Proterozoic Trans-Hudson Orogen of North America*, Special Paper 37, edited by Lewry, J.F. and M.R. Stauffer, pp. 15-39, Geol. Assoc. Can.
- Innes, M.J.S., Goodacre, A.K., Weston, A.A., and Weber, J.R., 1968. Gravity and isostasy. In; Beals, C.S. (Ed.), *Science, History and Hudson Bay*, Volumes 1 & 2. Department of Energy Mines and Resources, Ottawa, pp.703-729.
- James, T.S., 1992. The Hudson Bay free-air gravity anomaly and glacial rebound, *Geophysical Research Letters*, 19(9), 861-864.
- Kaneshima, S., M. Ando, and S. Kimura, 1988. Evidence from shear-wave splitting for restriction of seismic anisotropy to the upper crust, *Nature*, 335, 627-629.
- Kearey, P., K.A. Klepeis, and F.J. Vine, 2009. *Global tectonics*, Wiley-Blackwell.
- Kempton, P.D., H. Downes, L.A. Neymark, J.A. Wartho, R.E. Zartman, and E.V. Sharkov, 2001. Garnet granulite xenoliths from northern Baltic Shield – the underplated lower crust of a palaeoproterozoic large igneous province?, *J. Petrol.*, 42, 731-763.

- Kennett, B.L.N., and E.R. Engdahl, 1991. Traveltimes for global earthquake location and phase identification, *Geophys. J. Int.*, 105, 429-465.
- Kennett, B.L.N., E.R. Engdahl, and R. Buland, 1995. Constraints on seismic velocities in the Earth from traveltimes, *Geophys. J. In.*, 122, 108-124.
- Lebedev, S., and R.D. van der Hilst, 2008. Global upper-mantle tomography with the automated multimode inversion of surface and S wave forms, *Geophys. J. Int.*, 173, 505-518, doi:10.1111/j.1365-246X.2008.03721.x.
- Lebedev, A., J. Boonen, and J. Trampert, 2009. Seismic structure of Precambrian lithosphere: New constraints from broad-band surface-wave dispersion, *Lithos*, 109, 96-111.
- Lee, H.A., 1968. Quaternary geology, in *Science, History and Hudson Bay*, vol 1 & 2., edited by C.S. Beals, pp. 503-543, Department of Energy Mines and Resources, Ottawa, Ont.
- Lee, H., C.K. Shum, Y. Yi, A. Braun, and C-Y. Kuo, 2008. Laurentia crustal motion observed using TOPEX/POSEIDON radar altimetry over land, *J. Geodynamics*, 46, 182-193.
- Lin, F.C., M.H. Ritzwoller, J. Townend, M. Savage, and S. Bannister, 2007. Ambient noise Rayleigh wave tomography of New Zealand, *Geophys. J. Int.*, 170, 649–666, doi:10.1111/j.1365-246X.2007.03414.x.

- Lin, F., M.P. Moschetti, and M.H. Ritzwoller, 2008. Surface wave tomography of the western United States from ambient seismic noise: Rayleigh and Love wave phase velocity maps, *Geophys. J. Int.*, doi:10.1111/j1365-246X.2008.03720.x.
- Lin, F.C., M.H. Ritzwoller, Y. Yang, M.P. Moschetti, and M.J. Fouch, 2011. Complex and variable crustal and uppermost mantle seismic anisotropy in the western United States, *Nature Geosci.*, 4, doi:10.1038/NGE01036.
- Liu, Y., S. Gao, H. Yuan, L. Zhou, X. Liu, X. Wang, Z. Hu, and L. Wang, 2004. U-Pb zircon ages and Nd, Sr, and Pb isotopes of lower crustal xenoliths from North China Craton: insights on evolution of lower continental crust, *Chemical geology*, 211, 87-109, doi:10.1016/j.chemgeo.2004.06.023.
- Lobkis, O.L., and R.L. Weaver, 2001. On the emergence of the Green's function in the correlations of a diffuse field, *J. Acoust. Soc. Am.*, 110, doi:10.1121/1.1417528.
- Longuet-Higgins, M., 1950. A theory of the origin of microseisms, *Philos. Trans. R. Soc. London*, 243, 137-171.
- Longuet-Higgins, M., and R. Stewart, 1964. Radiation stresses in water waves: A physical discussion with application, *Deep Sea Res.*, 11, 529-562.
- Lozaro, I and V. Swail, 2002. The link between wave height variability in the North Atlantic and the storm track activity in the last four decades, *Atmosphere-Ocean*, 40, 377-388.

- Mahan, K. (2006), Retrograde mica in deep crustal granulites: Implications for crustal seismic anisotropy, *Geophys. Res. Lett.*, 33, doi:10.1029/2006GL028130.
- Mandeville, C.W., 2010. Sulfur: A ubiquitous and useful tracer in Earth and planetary sciences, *Elements*, 6, 75-80.
- McKenzie, D., 1978. Some remarks on the development of sedimentary basins, *Earth Planet. Sci. Lett.*, 40, 25-32.
- McNamara, D.E., and R.P. Buland, 2003. Ambient Noise Levels in the Continental United States, *Bull. Seis. Soc. Am.*, 94 (4), 1517-1527.
- Meier, T., Dietrich, K., Stockhert, B., and Harjes, H.-P., 2004. One-dimensional models of shear wave velocity for the eastern Mediterranean obtained from the inversion of Rayleigh wave phase velocities and tectonic implications. *Geophysical Journal International* 156, 45–58 doi:10.1111/j.1365-246X.2004.02121.x.
- Meltzer, A., and N. Christensen, 2001. Nanga Parbat crustal anisotropy: Implications for interpretation of crustal velocity structure and shear-wave splitting, *Geophys. Res. Lett.*, 28, 2129-2132.
- Moorkamp, M., A.G. Jones, and D.W. Eaton, 2007. Joint inversion of teleseismic receiver functions and magnetotelluric data using a genetic algorithm: Are seismic velocities and electrical conductivities compatible?, *Geophys. Res. Lett.*, 34, doi:10.1029/2007GL030519.

- Moschetti, M.P., M.H. Ritzwoller, and N.M. Shapiro, 2007. Surface wave tomography of the western United States from ambient seismic noise: Rayleigh wave group velocity maps, *Geochem., Geophys., Geosys.*, 8, doi:10.1029/2007GC001655.
- Moschetti, M.P., M.H. Ritzwoller, and F.C. Lin, 2010. Seismic evidence for widespread crustal deformation caused by extension in the western USA, *Nature*, 464, 885-889.
- Moser, D.E., and L.M. Heaman, 1997. Proterozoic zircon growth in Archean lower crustal xenoliths, southern Superior craton – a consequence of Matachewan ocean opening, *Contrib Mineral Petrol*, 128, 164-175.
- Paige, C.C., and M.A. Saunders, 1982. LSQR: an algorithm for sparse linear equations and sparse least squares, *Assoc. Comput. Mach. Trans. Math. Software*, 8, 43-71.
- Paulssen, H., 2004. Crustal anisotropy in southern California from local earthquake data, *Geophys. Res. Lett.*, 31, doi:10.1029/2003GL018654.
- Pawlak, A.P., D.W. Eaton, I.D. Bastow, J.M. Kendall, G. Helffrich, J. Wookey, and D. Snyder, 2011. Crustal structure beneath Hudson Bay from ambient-noise tomography: Implications for basin formation, *Geophys. J. Int.*, 184, 65-82, doi:10.1111/j.1365-246X.2010.04828.x
- Pawlak, A.P., D.W. Eaton, F.A. Darbyshire, S. Lebedev, and I.D. Bastow, 2012. Crustal anisotropy beneath Hudson Bay from ambient-noise tomography: evidence for post-orogenic lower-crustal flow?, *J. Geophys. Res.*, In review.

- Peltier, W.R., A.M. Forte, J.X. Mitrovica, and A.M. Dziewonski, 1992. Earth's gravitational field: seismic tomography resolves the enigma of the Laurentian anomaly, *Geophys. Res. Lett.*, 19(15), 1555-1558.
- Petersen, J., 1993. Observations and modeling of seismic background noise, Open-File Report, 93-322, US Geological Survey, Albuquerque, NM.
- Rhie, J. and B. Romanowicz, 2004. Excitation of Earth's continuous free oscillations by atmosphere-ocean-seafloor coupling, *Nature*, 431, 552-556.
- Rodi, W.L., P. Glover, T.M.C. Li, and S.S. Alexander, 1975. A fast, accurate method for computing group-velocity partial derivatives for Rayleigh and Love modes, *Bull. seism. Soc. Am.*, 65, 1105-1114.
- Roksandic, M.M., 1987. The tectonics and evolution of the Hudson Bay region, in *Sedimentary Basins and Basin-forming Mechanisms*, pp. 507-518, eds. Beaumont, C. and Tankard, A.J., Canadian Society of Petroleum Geologists Memoir 12.
- Rolandone, F., J.C. Mareschal, C. Jaupart, C. Gosselin, G. Bienfait, and R. Lapointe, 2003. Heat flow in the western Superior Province of the Canadian shield, *Geophys. Res. Lett.*, 30, doi:10.1029/2003GL017386.
- Romanowicz, B., 2003. Global mantle tomography: Progress status in the past 10 years, *Annu. Rev. Earth Planet. Sci.*, 31, 303-328, doi:10.1146/annurev.earth.31.091602.113555.

- Roux, P., and W.A. Kuperman, 2003. Extracting coherent wavefronts from acoustic ambient noise in the ocean, *J. Acoust. Soc. Am*, 116, 1995-2003.
- Roux, P., K. G. Sabra, P. Gerstoft, W. A. Kuperman, and M. C. Fehler, 2005. P-waves from cross- correlation of seismic noise, *Geophys. Res. Lett.*, 32, L19303, doi:10.1029/2005GL023803.
- Royden, L.H., B.C. Burchfiel, R.W. King, E. Wang, Z. Chen, F. Shen, and Y. Liu, 1997. Surface deformation and lower crustal flow in eastern Tibet, *Science*, 276, 788-790, doi:10.1126/science.276.5313.788.
- Ruffman, A. and M.J. Keen, 1967. A time-term analysis of the first arrival data from the seismic experiment in Hudson Bay, 1965. *Canadian Journal of Earth Sciences*, 4, 901–928.
- Sabra, K.G., P. Gerstoft, P. Roux, W.A. Kuperman, and M.C. Fehler, 2005. Extracting time-domain Green's function estimates from ambient seismic noise, *Geophys. Res. Lett.*, 32, L03310, doi:10.1029/2004GL021862.
- Sanford, B.V., 1987. Paleozoic geology of the Hudson Platform, *Canadian Society of Petroleum Geologists Memoir*, 12, 507-518.
- Sanford, B.V., 1990. Paleozoic geology of the Hudson platform. in *Sedimentary Basins and Basin-forming Mechanisms*, pp. 483-505, eds. Beaumont, C. & Tankard, A.J., *Canadian Society of Petroleum Geologists Memoir 12 and AGS Special Publication 5*.

- Saygin, E., and B.L.N. Kennett, 2010. Ambient seismic noise tomography of Australian continent, *Tectonophysics*, 481, 116-125, doi:10.1016/j.tecto.2008.11.013.
- Schwarzbach, C., R.U. Börner, and K. Spitzer, 2005. Two-dimensional inversion of direct current resistivity data using a parallel, multi-objective genetic algorithm, *Geophys. J. Int.*, 162, 685-695, doi:10.1111/j.1365-246X.2005.02702.x .
- Shapiro, N., and M.H. Ritzwoller, 2002. Monte-Carlo inversion for a global shear-velocity model of the crust and upper mantle. *Geophys. J. Int.*, 151, 88–105.
- Shapiro, N.M., and M. Campillo, 2004. Emergence of broadband Rayleigh waves from correlations of ambient seismic noise, *Geophys. Res. Lett.*, 31, doi:10.1029/2004GL019491.
- Shapiro, N.M., M.H. Ritzwoller, P. Molar, and V. Levin, 2004. Thinning and flow of Tibetan crust constrained by seismic anisotropy, *Science*, 305, 233-236.
- Shapiro, N.M., M. Campillo, L. Stehly, and M.H. Ritzwoller, 2005. High resolution surface wave tomography from ambient seismic noise, *Science*, 307, 1615-1618.
- Sheriff, R.E., and L.P. Geldart, 1995. *Exploration Seismology*, Cambridge University Press.
- Silver, P.G., and W.W. Chan, 1988. Implications for crustal structure and evolution from seismic anisotropy, *Nature*, 335, 34-39.

- Silver, P. G., 1996. Seismic anisotropy beneath the continents: Probing the depths of geology, *Annual Rev. Earth Planet. Sci.*, 24, 385-432, doi:10.1146/annurev.earth.24.1.385
- Smith, M.L., and F.A. Dahlen, 1973. The azimuthal dependence of Love and Rayleigh wave propagation in a slightly anisotropic medium, *J. Geophys. Res.*, 78, 3321-3333.
- Smith, D.B., M.H. Ritzwoller, and N.M. Shapiro, 2004. Stratification of anisotropy in the Pacific upper mantle, *J. Geophys. Res.*, 109, B11309, doi:10.1029/2004JB003200.
- Snieder R., 2004. Extracting the Green's function from the correlation of coda waves: A derivation based on stationary phase, *Physical Review*, 69, 046610, doi:10.1103/PhysRevE.69.046610.
- Steffen, R., D.W. Eaton, and P. Wu, 2012. Moment tensors, state of stress and their relation to postglacial rebound in northeastern Canada, *Geophys. J. Int.*, in press.
- Stehly, L., M. Campillo, and N.M. Shapiro, 2006. A study of the seismic noise from its long-range correlation properties, *J. Geophys. Res.*, 111, doi:10.1029/2005JB004237.
- Stein, S., and M. Wysession, 2003. An introduction to seismology, earthquakes, and Earth structure, Blackwell Publishing.

- St-Onge, M.R., M.P. Searle, and N. Wodicka, 2006. Trans-Hudson Orogen of North America and Himalaya-Karakoram-Tibetan Orogen of Asia: Structural and thermal characteristics of the lower and upper plates, *Tectonics*, 25, doi:10.1029/2005TC001907.
- St-Onge, M.R., J.A.M. Van Gool, A.A. Garde, and D.J. Scott, 2009. Correlation of Archaean and Palaeoproterozoic units between northeastern Canada and western Greenland: constraining the pre-collisional upper plate accretionary history of the Trans-Hudson Orogen, in *Earth Accretionary Systems in Space and Time*, pp. 193-235, eds, Cawood, P.A. and Kroner, A., The Geological Society, London, Special Publications, doi:10.1144/SP3187.
- Snyder, D.B., R.G. Berman, R G, and J.M. Kendall, 2012. Seismic anisotropy and mantle structure of the Rae Craton, Central Canada, from joint interpretation of SKS splitting and receiver functions, Sanborn-Barrie, M. Precambrian Research (in revision).
- Symons, D.T.A., and M.J. Harris, 2005. Accretion history of the Trans-Hudson Orogen in Manitoba and Saskatchewan from paleomagnetism, *Can. J. Earth Sci.*, 42, 723-740, doi:10.1139/E04-090.
- Takeuchi, H., J. Dorman, and M. Saito, 1964. Partial derivatives of surface wave phase velocity with respect to physical parameter changes within the Earth, *J. Geophys. Res.*, 69, 3429- 3441.

- Tarasov, L., and W.R. Reltier, 2004. A geophysically constrained large ensemble analysis of the deglacial history of the North American ice-sheet complex, *Quaternary Science Reviews*, 23, 359-388, doi:10.1016/j.quascirev.2003.08.004
- Thompson, D.A., I.D. Bastow, G. Helffrich, J.M. Kendall, J. Wookey, D.Snyder, and D.W. Eaton, 2010. Precambrian crustal evolution of the Canadian Shield: Constraints from receiver function analysis, *Earth Planet. Sci. Lett.*, 297, 655-666, doi:10.1016/j.epsl.2010.07.021.
- Thompson, D.A., G. Helffrich, I.D. Bastow, J. Wookey, J-M. Kendall, D. Eaton, and D. Snyder, 2011. Implications of a simple mantle transition zone beneath cratonic North America, *Earth Planet. Sci. Letts.*, 312, 28-36, doi:10.1016/j.epsl.2011.09.037.
- Villasenor, A., Y. Yang, M.H. Ritzwoller, and J. Gallart, 2007. Ambient noise surface wave tomography of the Iberian Peninsula: Implications for shallow seismic structure, *Geophys. Res. Lett.*, 34, L11304, doi:10.1029/2007GL030164.
- Wang, Z., and F.A. Dahlen, 1995. Spherical-spline parameterization of 3-dimensional earth models, *Geophys. Res. Lett.*, 22, 3099-3102.
- Weaver, R.L., and O.I. Lobkis, 2001. Ultrasonics without a source: Thermal fluctuation correlations at MHz Frequencies, *Phys. Rev. Lett.*, 87, doi:10.1103/PhysRevLett.87.134301.

- Wessel, P, and W.H.F. Smith, 1995. New Version of the Generic Mapping Tools Released, EOS Trans. AGU, 76, 329.
- White, R.E., 1991. Properties of instantaneous seismic attributes, The Leading Edge 10, 26, doi:10.1190/1.1436827.
- Winterstein, D.F., 1990. Velocity anisotropy terminology for geophysicists, Geophysics, 55, 1070-1088.
- Winterstein, D., 1992. How shear-wave properties relate to rock fractures: Simple cases, The Leading Edge, 11, 9, 21-28.
- Wu, P., 1996. Changes in orientation of near-surface stress field as constraints to mantle viscosity and horizontal stress differences in Eastern Canada, Geophys. Res. Lett., 23, 2263-2266.
- Wu, P., 1997. Effect of viscosity structure on fault potential and stress orientations in eastern Canada, Geophys. J. Int., 130, 365-382.
- Wu, P., 2002. Effects of Mantle Flow Law Stress Exponent on Postglacial Induced Surface Motion and Gravity in Laurentia, Geophys. J. Int., 148, 676-686.
- Wu, P., 2005. Effects of lateral variations in lithospheric thickness and mantle viscosity on glacially induced surface motion in Laurentia, Earth Planet. Sci. Lett., 235, 549-563.

- Wüstefeld, A., G. Bokelmann, and G. Barruol, 2010. Evidence for ancient lithospheric deformation in the East European Craton based on mantle seismic anisotropy and crustal magnetics, *Tectonophysics*, 481, 16-28, doi:10.1016/j.tecto.2009.01.010.
- Yang, Y., and D.W. Forsyth, 2006. Rayleigh wave phase velocities, small-scale convection, and azimuthal anisotropy beneath Southern California, *J. Geophys. Res.*, 111, B07306, doi:10.1029/2005JB004180.
- Yang, Y., M.H. Ritzwoller, A.L. Levshin, and N.M. Shapiro, 2007. Ambient noise Rayleigh wave tomography across Europe, *Geophys. J. Int.*, 168, 259-274, doi:10.1111/j.1365-246X.2006.03203.x.
- Yang, Y., A. Li, and M.H. Ritzwoller, 2008. Crustal and uppermost mantle structure in southern Africa revealed from ambient noise and teleseismic tomography. *Geophysical Journal International* 174, 235–248, doi:10.1111/j.1365-246X.2008.03779.x.
- Yang, Y. and M.H. Ritzwoller, 2008. Characteristics of ambient seismic noise as a source for surface wave tomography, *Geochem. Geophys. Geosyst.*, 9, doi:10.1029/2007GC001814.
- Yang, Y., W. Shen, and M H. Ritzwoller, 2011. Surface wave tomography on a large-scale seismic array combining ambient noise and teleseismic earthquake data, *Earthq. Sci.*, 24, 55-64, doi:10.1007/s11589-011-0769-3.

- Yao, H., R.D. van der Hilst, and M.V. de Hoop, 2006. Surface-wave tomography in SE Tibet from ambient seismic noise and two-station analysis: I.- Phase velocity maps, *Geophys. J. Int.*, 166, 732-744, doi: 10.1111/j.1365-246X.2006.03028.x.
- Yao, H.J., and R.D. van der Hilst, 2009. Analysis of ambient noise energy distribution and phase velocity bias in ambient noise tomography, with application to SE Tibet, *Geophys. J. Int.*, 179, 1113-1132, doi:10.1111/j.1365-246X.2009.04329.x.
- Yilmaz, O., 1987. *Seismic data processing*. Society of Exploration Geophysicists, Tulsa.
- Zhang, S., and S-I. Karato, 1995. Lattice preferred orientation of olivine aggregates deformed in simple shear, *Nature*, 375, 774-777, doi:10.1038/375774a0.
- Zheng, S., X. Sun, X. Song, Y. Yang, and M.H. Ritzwoller, 2008, Surface wave tomography of China from ambient seismic noise correlation, *Geochem. Geophys. Geosyst.*, 9, Q0502, doi:10.1029/2008GC001981.
- Zhou, L., J. Xie, W. Shen, Y. Zheng, Y. Yang, H. Shi, and M.H. Ritzwoller 2012. The structure of the crust and uppermost mantle beneath South China from ambient noise and earthquake tomography, *Geophys. J. Int.*, submitted.

## Appendix A: CHOICE OF REGULARIZATION PARAMETERS

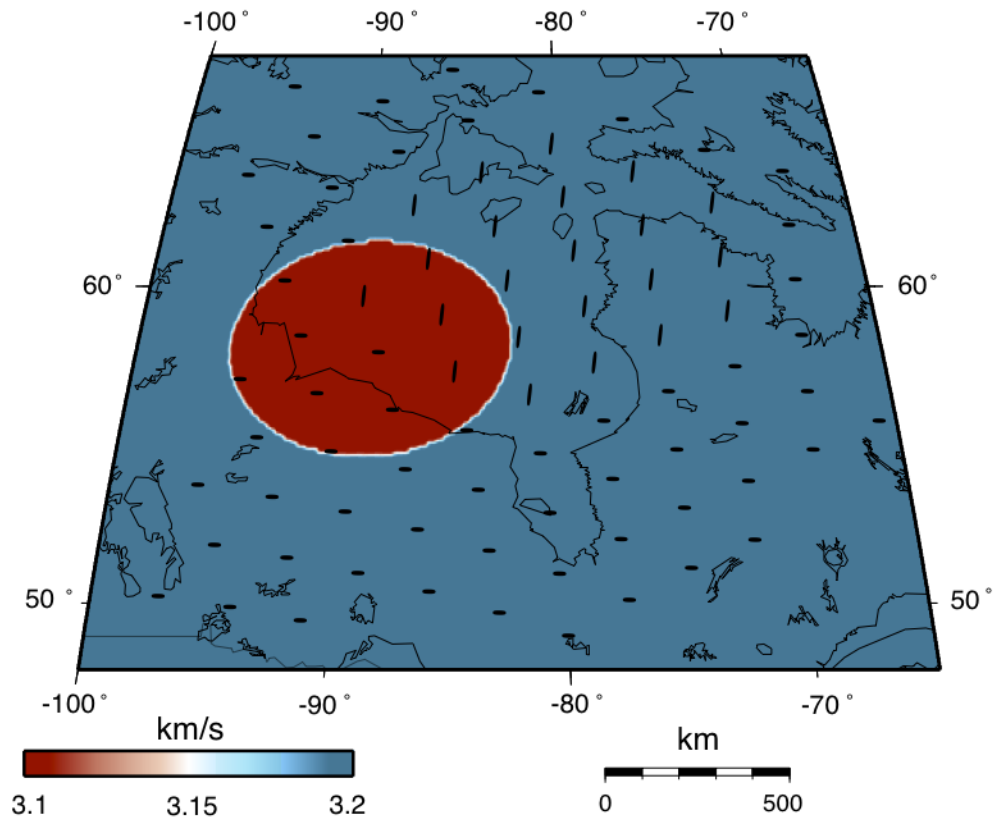
In this section we test smoothing and gradient damping for both isotropic and  $2\Psi$  anisotropic model parameters. The aim of these tests is to evaluate the significance of parameter coupling (“leakage”) in which isotropic heterogeneity and anisotropy may trade off with each other in the solution. To this end, our first test model (Figure A1) contains partly overlapping isotropic and anisotropic anomalous regions. The isotropic component has a background velocity of 3.2 km/s with a low-velocity region (3.1 km/s) in the southwest corner. The anisotropic component is confined to  $2\Psi$  anisotropy, with a background east-west fast direction and an anomalous, strongly anisotropic region with a N-S fast axis, located in the northeast part of the model.

We begin by examining the effects of smoothing and damping parameters to explore their influence on the inversion results. These parameters are analyzed by examining the trade-off between model variance and roughness (Figure A2). The model roughness is the square root of the sum of the squared differences between anomalies at each grid knot and averages over the anomalies at all of its nearest-neighbor knots. The absolute value of the roughness has no physical meaning, but relative changes of the roughness between

different tomographic solutions are meaningful. The variance is defined as the data-synthetic variance after the inversion divided by the initial variance. Figure 3.8 shows trade-offs, one for the isotropic velocity and one for the  $2\Psi$  anisotropy, for 20s period. Each of the blue points represents a specific combination of 4 parameters, smoothing and damping of the isotropic term and smoothing and damping of the  $2\Psi$  term. These results are similar for other periods. The black line represents the case in which all parameters are equal and serves solely as a guide for the trend in the curve.

The overall shape of the curve provides an indication of the behavior of the parameters and furnishes a range of parameter choices. It is clearly desirable to minimize both variance and model roughness simultaneously, since minimizing the variance results in a better fit to the data while minimizing the roughness will reduce artifacts in the result (Schwarzbach et al., 2005). Generally the ‘knee’, or the bend that minimizes both the variance and the roughness of the trade-off curve, is thought to indicate the best range of parameters and produce the best results for the data (e.g. Moorkamp et al., 2007).

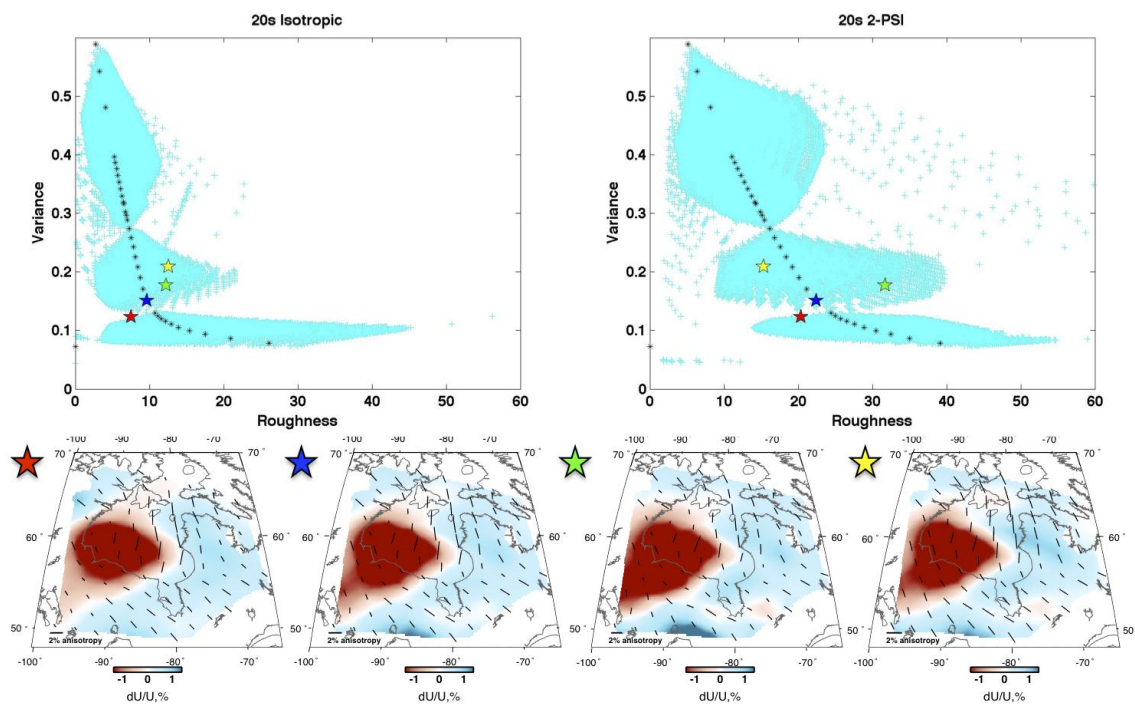
The solutions for a selection of parameters, chosen arbitrarily such that they fall in the ‘knee’ zone on both trade-off curves, are shown as stars in Figure A1. The corresponding inversion results are shown below the graphs. The actual values of each of the parameters as well as resulting roughness and variance values are given in Table 1. Each result appears to be consistent with the input model, making it difficult to pick any one as the ‘best’ parameter. Using the forward model to pick parameters allows us to choose a good range of parameters, but ultimately the parameter selection is highly dependent on the data, so that parameter selection needs to be done using the data as well.



**Figure A1 Anisotropic model for parameter testing.**

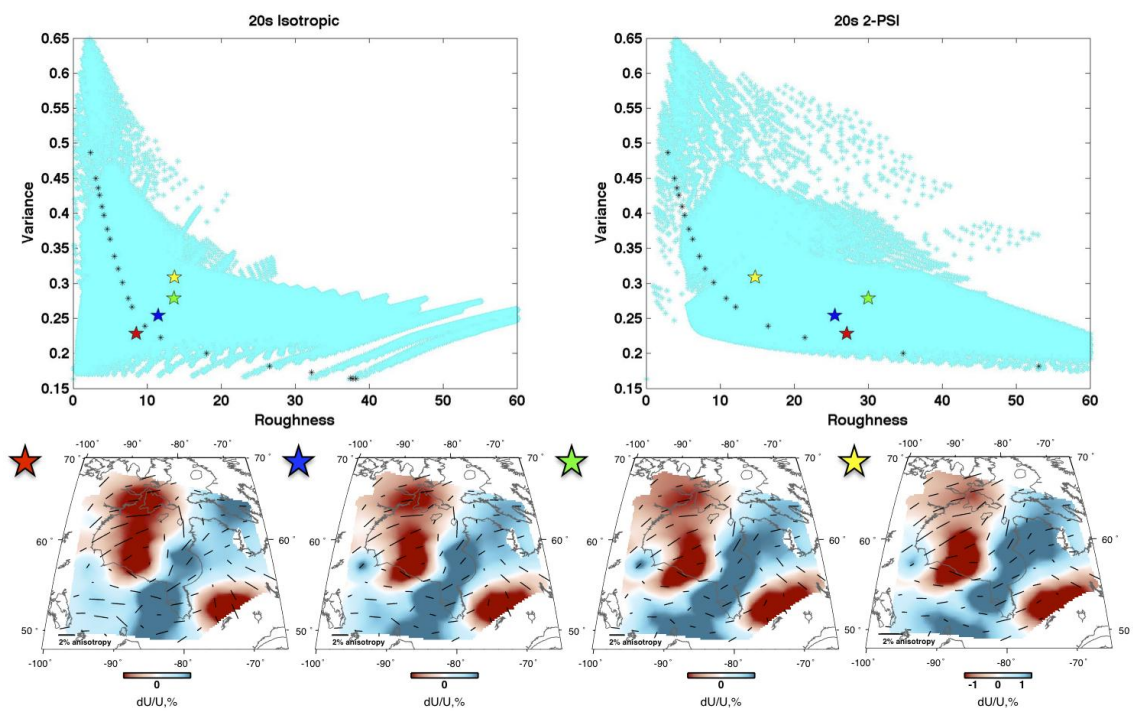
Model used for parameter testing, containing an overlapping isotropic anomaly in the SW and an anomalous anisotropic region in the NE part of the study area. Only  $2\Psi$  anisotropy is considered.

Figure A3 is the same as Figure A2, but it uses the Hudson Bay dataset. The stars represent the same parameter choice as in Figure A2. Using the given dataset, the parameter values considered in the previous example still fall near the ‘knee’ zone on both trade-off curves. The isotropic velocity patterns are consistent through all four parameter choices, and are consistent with results found by Pawlak et al. (2011). Anisotropic results generally show the same pattern in all four images. We observe that the red, blue and green star models contain anisotropy directions that form a vortex pattern south of the Bay. This is most likely an artefact arising from the parameter choice, resulting in higher anisotropic roughness. This artefact does not appear in the yellow star model and thus we choose this set of regularization parameters (Table A1) for analysis in this study.



**Figure A2 Trade-off curves for synthetic data.**

Trade-off curves of synthetic data for isotropic and anisotropic variations for various parameter choices. Modeled results are shown for parameter choices indicated with the colored stars.



**Figure A3 Trade-off curves for real data.**

Trade-off curves of real data for isotropic and anisotropic variations for various parameter choices. Data results are shown for parameter choices indicated with the colored stars.

| Chosen Parameters |         |           |         | Resulting Values for Figure A2 |         |          |   |
|-------------------|---------|-----------|---------|--------------------------------|---------|----------|---|
| Smoothness        |         | Damping   |         | Roughness                      |         | Variance |   |
| Isotropic         | $2\Psi$ | Isotropic | $2\Psi$ | Isotropic                      | $2\Psi$ |          |   |
| 0.22              | 0.13    | 0.07      | 0.06    | 7.53                           | 20.36   | 0.12     |    |
| 0.15              | 0.15    | 0.15      | 0.15    | 9.66                           | 22.42   | 0.15     |    |
| 0.10              | 0.10    | 0.25      | 0.30    | 12.19                          | 31.71   | 0.17     |    |
| 0.20              | 0.35    | 0.20      | 0.40    | 12.52                          | 15.29   | 0.21     |    |
| Chosen Parameters |         |           |         | Resulting Values for Figure A3 |         |          |   |
| Smoothness        |         | Damping   |         | Roughness                      |         | Variance |   |
| Isotropic         | $2\Psi$ | Isotropic | $2\Psi$ | Isotropic                      | $2\Psi$ |          |   |
| 0.22              | 0.13    | 0.07      | 0.06    | 8.56                           | 27.14   | 0.22     |  |
| 0.15              | 0.15    | 0.15      | 0.15    | 11.50                          | 25.51   | 0.25     |  |
| 0.10              | 0.10    | 0.25      | 0.30    | 13.64                          | 30.01   | 0.27     |  |
| 0.20              | 0.35    | 0.20      | 0.40    | 13.70                          | 14.73   | 0.30     |  |

**Table A1 Parameter values.**

Parameter input and output values corresponding with stars in Figure A2 and A3. A full range of parameters were tested, the above is a subset of what was tested.

## Appendix B: **BOOTSTRAP ERROR ANALYSIS**

To quantify and examine uncertainties associated with anisotropic fast directions and amplitudes, we have performed a bootstrap resampling error analysis (Chernick, 1999). The bootstrap method has the advantage that it makes no assumptions about the properties of the statistical distribution. The error analysis is evaluated by randomly selecting paths (with substitution) from the complete set of observed paths used in the original inversion. A total of 100 random sets of paths are then each inverted, and the distribution of inversion results is analyzed to assess uncertainties in the data and process.

Representative uncertainty results are illustrated using histogram plots for two representative regions, HUB and SUP (Figure B1) for 20 s period. Each region contains four knot points. The percent amplitude and azimuth variation are shown for each of the knot points within the HUB region (Figure B2) and SUP region (Figure B3), which sample distinct areas of Hudson Bay. As expected, the derived parameters exhibit an approximately normal distribution. Anisotropic percent amplitude is generally larger at HUB than at SUP. The anisotropic fast azimuths are fairly stable and consistent through the four knot points at HUB; however, at SUP there is more scatter in azimuth.

A resolution plot showing the 95% confidence intervals (i.e. 2 standard deviations from the bootstrap analysis) for 20 s period is shown in Figure B4. This plot also shows an average azimuth and amplitude at each grid knot resulting from the bootstrap analysis. These results show that, within our area of interest near the center of Hudson Bay, anisotropy directions have uncertainties within  $\pm 30^\circ$ . Average fast directions and amplitudes are consistent with results for 20 s period (Figure 3.10).

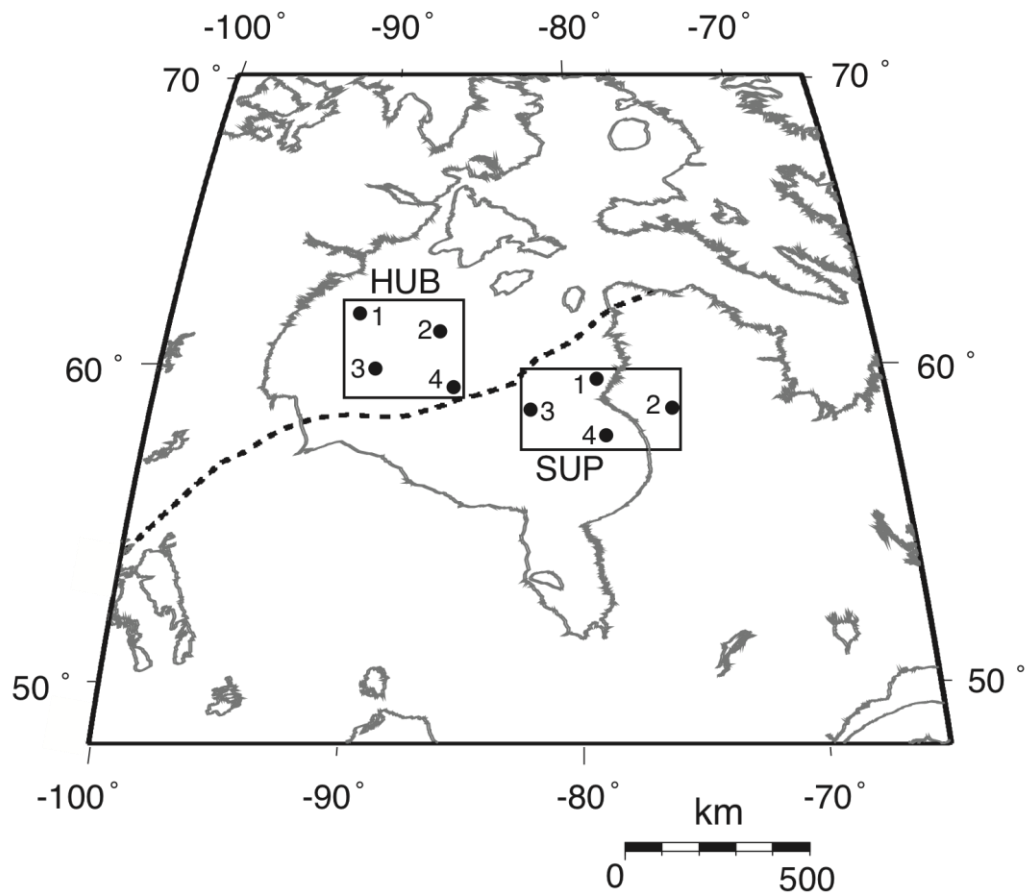


**Figure B1 Knot point and suture location map.**

Black boxes show locations of HUB and SUP and corresponding knot points within these regions used for bootstrap error analysis. Black dashed line shows the location of the THO suture zone.

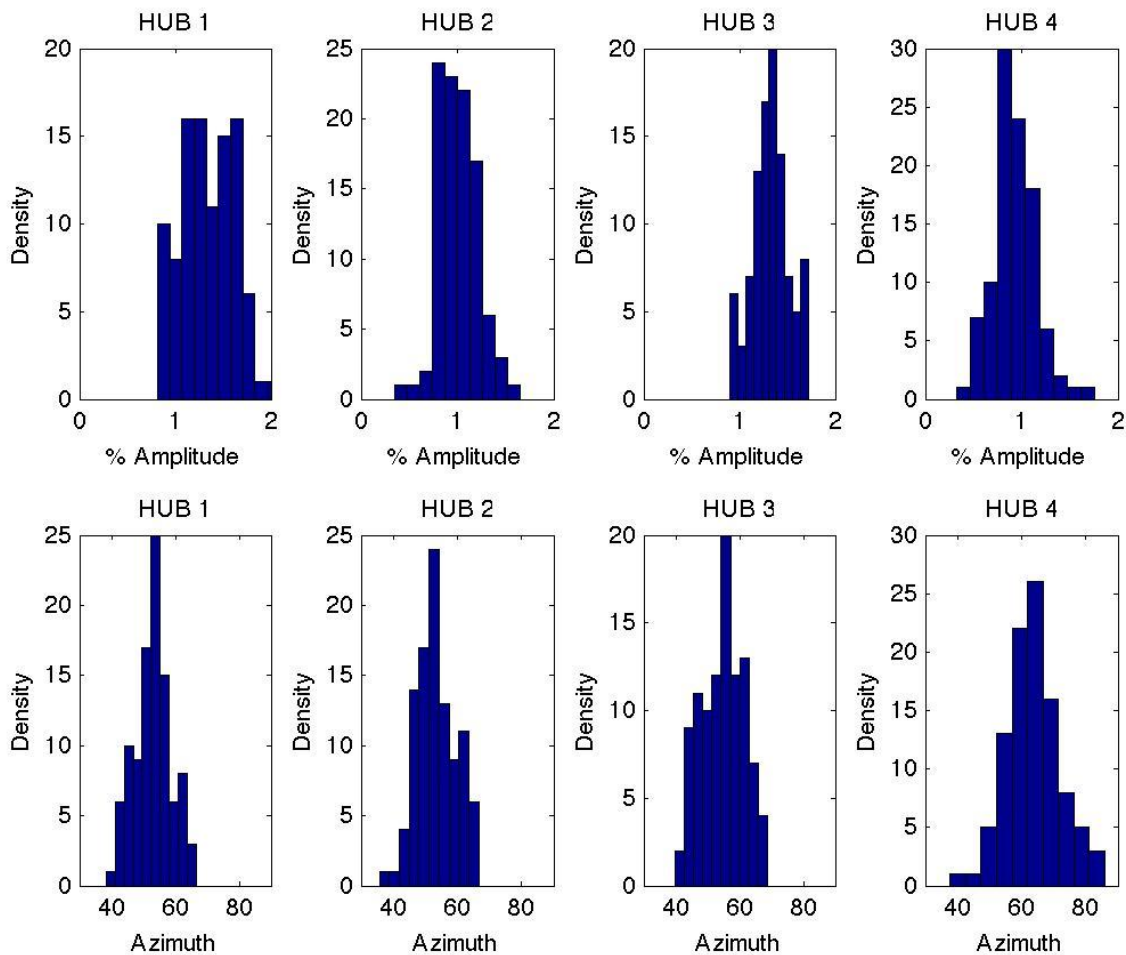


**Figure B2 HUB region amplitude and azimuth histograms.**

Histograms of amplitude (top row) and azimuth (bottom row) distribution for bootstrap error analysis for the four knot points in the HUB region (Figure B1).

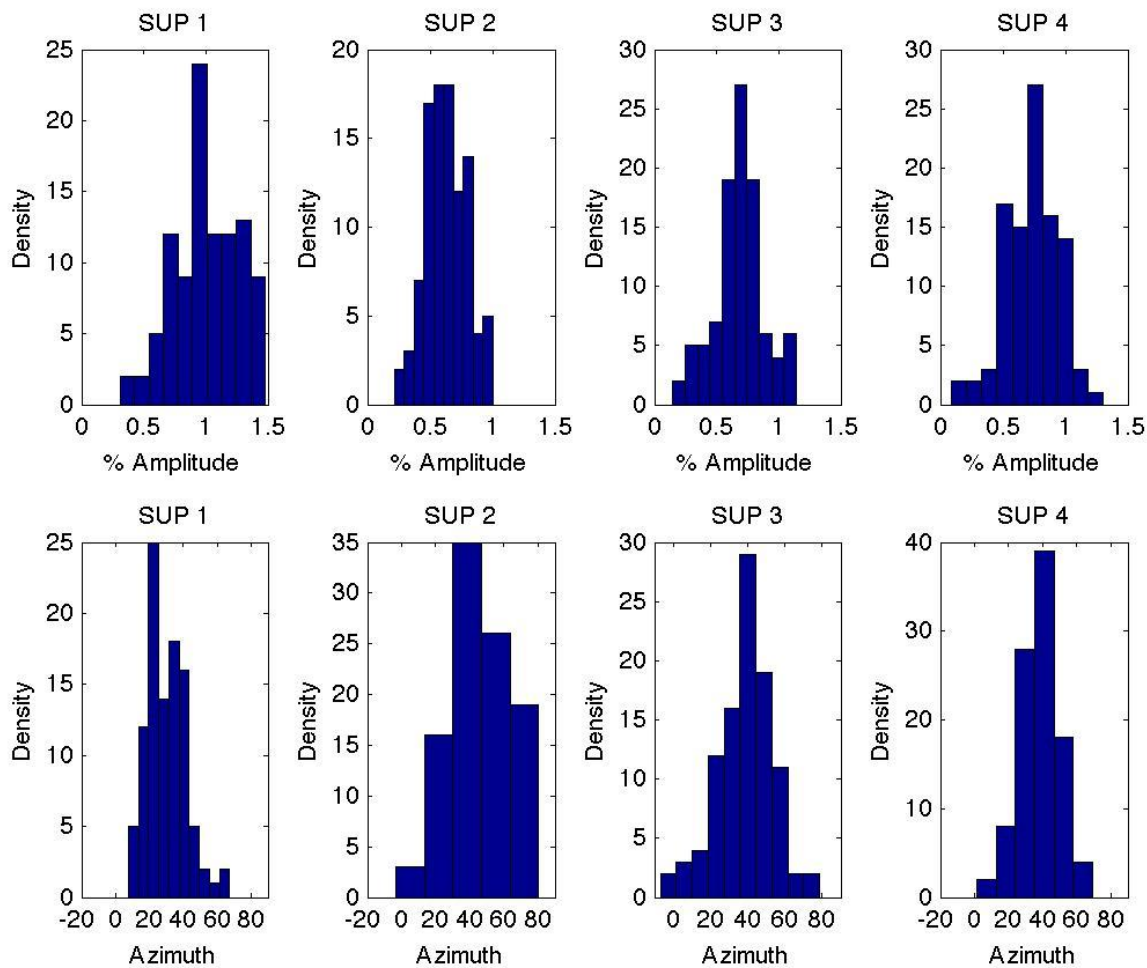


**Figure B3 SUP region amplitude and azimuth histograms.**

Histograms of amplitude (top row) and azimuth (bottom row) distribution for bootstrap error analysis for the four knot points in the SUP region (Figure B1).

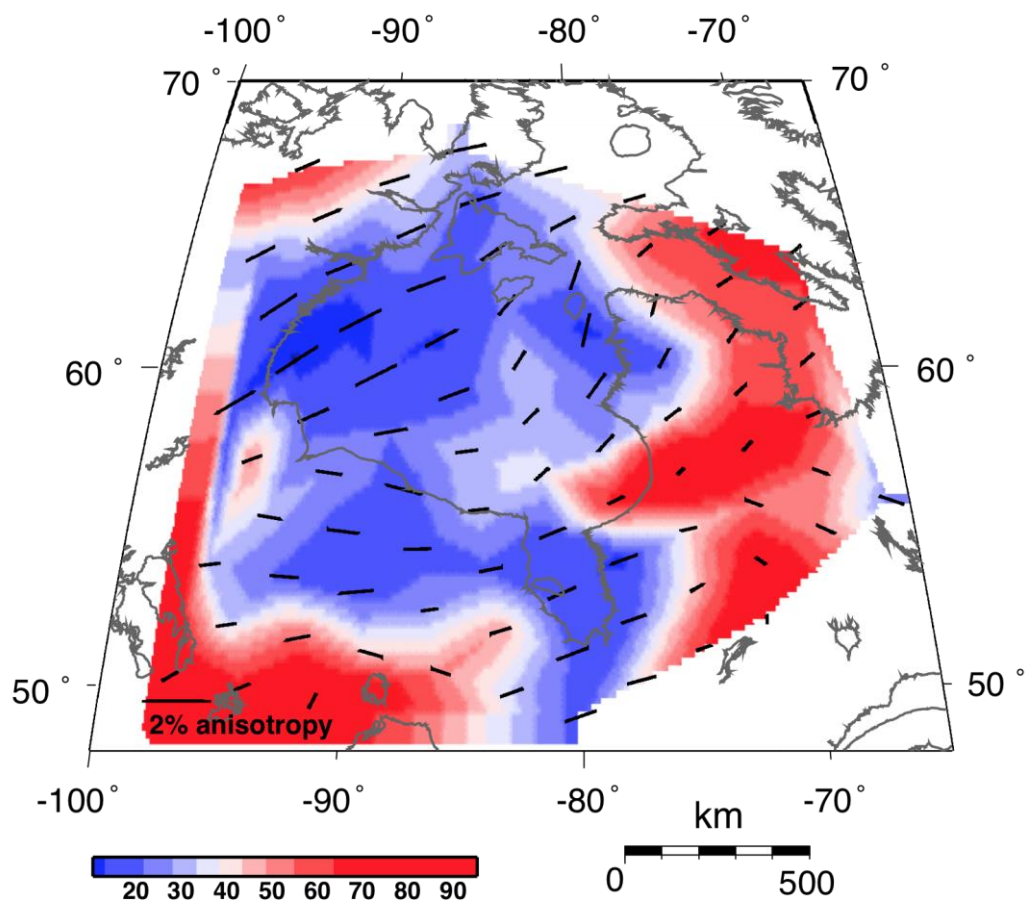


**Figure B4 Error distribution map.**

Error distribution map from the bootstrap error analysis at 20 s period. Color scale shows azimuth degrees of 95% confidence interval. Black lines show average azimuth and amplitude from bootstrap error analysis.

## Appendix C: **SAMPLE CODE**

All code is implemented in Matlab.

### **C.1. Pre-processing**

The function `preproc` does the pre-processing using data for which mean and trend has been removed and has been resampled to 1 Hz. The function calls on `tnorm` and `whiten` (also shown below) as well as `filtf` and `aec`, which are part of the CREWES toolbox. All other functions are built-in Matlab functions.

```
%%%%%%%%%%%%%%%%%%%%%%%%%%%%%%%%%%%%%%%%%%%%%%%%%%%%%%%%%%%%%%%%%%%%%%%%%
```

```
% Required input parameters:
```

```
% data = input data
```

```
% procdata = processed data
```

```
% type = type of normalization: 0 - one-bit normalization, 1 - aec
```

```
% m = median filter factor: default =71
```

```
% fmin = min frequency (2 values)
```

```
% fmax = max frequency (2 values)
```

```
%%%%%%%%%%%%%%%%%%%%%%%%%%%%%%%%%%%%%%%%%%%%%%%%%%%%%%%%%%%%%%%%%%%%%%%%%
```

```
% Do all pre-processing
```

```
function procdata = preproc(data)
```

```
outdata = tnorm(data); % temporal normalization
```

```
[whitew,whitet] = whiten(outdata); % spectral whitening
```

```
if nargin < 4
```

```
    fmin = [0.005, 0.0025];
```

```
    fmax = [.3, 0.1];
```

```
end
```

```
t = [0:(length(data)-1)];
```

```
procdata = filtf(whitet,t,fmin,fmax); % filter data
```

```
%%%%%%%%%%%%%%%%%%%%%%%%%%%%%%%%%%%%%%%%%%%%%%%%%%%%%%%%%%%%%%%%%%%%%%%%%
```

```
% Temporal Normalization
```

```
function outdata = tnorm(data, type)
```

```
if nargin < 2
```

```
    type = 0;
```

```
end
```

```
if type == 0
```

```
    outdata(data>0) = 1;
```

```
    outdata(data<0) = -1;
```

```
else
```

```

    outdata = aec(data, 1,1000);

end

%%%%%%%%%%%%%%%%%%%%%%%%%%%%%%%%%%%%%%%%%%%%%%%%%%%%%%%%%%%%%%%%%%%%%%%%

% Function to spectrally whiten the data
function [whitef,whitet] = whiten(data,m)

if nargin < 2
    m = 71;
end

spec = fft(data); % Fourier transform to frequency domain
smoothspec = medfilt1(spec, m); % Smooth spectrum
smoothamp = abs(smoothspec); % Smoothed amplitude spectrum

testspec = spec./smoothamp; % Whitening
if isnan(mean(testspec)) % Deal with NaNs
    for j = 1 : 82000
        if spec(j) == 0 && smoothamp(j) ==0
            whitef(j) = 0;
        else
            whitef(j) = spec(j)./smoothamp(j);
        end
    end
end

else

```

```

    whitet = testspec;

end

whitet = ifft(whitet);

%%%%%%%%%%%%%%%%%%%%%%%%%%%%%%%%%%%%%%%%%%%%%%%%%%%%%%%%%%%%%%%%%%%%%%%%

```

## C.2. Cross-correlation and Stacking

The cross-correlation calculation requires a database of the data. This database includes a table of all common days between stations pairs, station names, start dates, etc. The first code organizes the data and the function `crosscor1` does the cross-correlations and stacking.

```

%%%%%%%%%%%%%%%%%%%%%%%%%%%%%%%%%%%%%%%%%%%%%%%%%%%%%%%%%%%%%%%%%%%%%%%%

```

```

% Required input parameters:

```

```

% database.mat - database created by stat_db.m which contains :

```

```

    % statdb – database of common days of data for all stations

```

```

    % statname – Station names

```

```

    % daysperyear – Number of days in the year

```

```

    % nyear – Number of years of data

```

```

    % nstat – Number of stations

```

```

    % startyear – Start year of data

```

```

    % startjulday – Start Julian day of data

```

```

% stat1 – first station in crosscorrelation (ie. AKVQ = 5)

```

```

% stat2 – Second station in crosscorrelation (ie. INUQ = 11)

```

```

% maxlag – Calculate correlation over range of lags, -maxlag to maxlag

```

```

% statlist – LISt of all stations

% k – Number of days correlated

% year.txt – Year list

% month.txt – Month list

% dirlist.txt – Daily directory list

%%%%%%%%%%%%%%%%%%%%%%%%%%%%%%%%%%%%%%%%%%%%%%%%%%%%%%%%%%%%%%%%%%%%%%%%

load database.mat % Load the database

maxlag = 1500; % Maximum lag in time samples

n = 0; % Counter

totpairs = (nstat*(nstat-1))/2;

for stat1 = 1 : nstat

    for stat2 = 1 : stat1

        if stat1 ~= stat2

            n = n + 1;

            [dist,corrfun,k] = crosscor1(stat1, stat2, maxlag, statname, statdb, startyear, ...

startjulday, daysperyear);

            ij(n,:) = [stat1,stat2,dist,k];

            if any(abs(corrfun)>0)

                corr(stat1,stat2) = 1;

                allcorr(:,n) = corrfun;

            end

        end

    end

end

```

```

end

end

%%%%%%%%%%%%%%%%%%%%%%%%%%%%%%%%%%%%%%%%%%%%%%%%%%%%%%%%%%%%%%%%%%%%%%%%

function [dist,corrfun,k] = crosscor1(stat1, stat2, maxlag, statname, statdb, startyear,
startjulday,daysperyear);

both = statdb(stat1,:) .* statdb(stat2,:); % test which days both stations have data

dist = 0;

cwd = pwd;

k = 0;

yid = fopen('year.txt','r');

year = fgetl(yid);

if any(both>0)

while ischar(year) % loop through each year

    cd (year)

    mid = fopen('month.txt','r');

    month = fgetl(mid);

    ywd = pwd;

    while ischar(month) % loop through each month

        cd (month)

        fid = fopen('dirlist.txt','r');

        dirname = fgetl(fid);

        mwd = pwd;

```

```

while ischar(dirname) % loop through each day
    cd (dirname)
    load procdata;
    yr = header(1).nzyear;
    jday = header(1).nzjday;
    yrsincestart = yr - startyear;
    day = jday - startjulday + 1;
    for i = 1:yrsincestart;
        day = day + daysperyear(i);
    end
    if both(day) == 1 % if both stations have data on this day then do
cross-correlation
        for j = 1: length(gcarc)
            if stat(j,:) == statname(stat1,:)
                j1 = j;
            end
            if stat(j,:) == statname(stat2,:)
                j2 = j;
            end
        end
    end
    if dist == 0
        lat1 = header(j1).stla;
        lon1 = header(j1).stlo;

```

```

        lat2 = header(j2).stla;

        lon2 = header(j2).stlo;

        delta = get_delta(lat1,lon1,lat2,lon2);

        dist = delta * 111;

    end

    k = k + 1;

    sprintf('correlating stations %s and %s for day %d',statname(stat1,:),
statname(stat2,:),day)

    dayxcorr = xcorr(allprocddata(:,j1),allprocddata(:,j2), maxlag, 'coeff');

    if k ==1

        corrfun = dayxcorr;

    else

        corrfun = corrfun + dayxcorr; % Stack results

    end

end

cd (mwd);

dirname = fgetl(fid);

end

fclose(fid);

cd (ywd)

month = fgetl(mid);

end

fclose(mid);

```

```

    cd (cwd)

    year = fgetl(yid);

end

fclose(yid);

end

if exist('corrfun')

    corrfun = corrfun/k; % fix average

else

    corrfun = 0;

end

%%%%%%%%%%%%%%%%%%%%%%%%%%%%%%%%%%%%%%%%%%%%%%%%%%%%%%%%%%%%%%%%%%%%%%%%

```

### C.3. Frequency-Time Analysis for Group-Velocity Dispersion Calculation

```

%%%%%%%%%%%%%%%%%%%%%%%%%%%%%%%%%%%%%%%%%%%%%%%%%%%%%%%%%%%%%%%%%%%%%%%%

% Required input parameters:

% oscorr – One sided correlation or EGF

% list – List of station pairs and great-circle distance between stations

%%%%%%%%%%%%%%%%%%%%%%%%%%%%%%%%%%%%%%%%%%%%%%%%%%%%%%%%%%%%%%%%%%%%%%%%

for n = 1:591; % loop through all station pairs

    T = [4 : .5 : 100]; % Period range

    f = 1./T'; % Frequency

    t2 = [1 : 1024]; % Time

```

```

trace = osccorr(:, n); % cross-correlation of nth station pair

ctrace = trace(1:1024); % Clip trace to 512 samples (power of 2)

fmax = [2*f,f*.5]; % Max frequency bands

fmin = [f-0.3*f,f*0.3]; % Min frequency bands

for i = 1:length(fmin);

    trace = filtf(ctrace,t2,fmin(i,:),fmax(i,:)); % Filter trace into small
frequency bands

    A(:,i) = trace(:);

end

for i = 1:length(fmin);

    trace = A(:, i);

    b(:,i) = hilb(trace); % Hilbert transform

    B(:,i) = abs(b(:,i)); % Amplitude envelope

    B(:,i) = B(:,i)/max(B(:,i)); % Normalized amplitude envelope

end

vg = list(n, 3)./t2; % Calculate group velocity (velocity = distance/time)

figure; pcolor(T,vg,B); shading flat

axis([4,100,2.5,5]);

xlabel('Period (s)');

ylabel('Group velocity (km/s)');

titlstring = [stat(list(n,1),:),' - ',stat(list(n,2),:)];

title(titlstring);

```

```
% User interactive data range selection:

disp('Pick maximum plausible group velocity using the left mouse button');

[tdummy,vmax] = ginput(1);

iflag = 0;

for i = length(vg):-1:1;

    if iflag == 0 & vg(i) > vmax;

        iflag = 1;

        jmax = i;

    end

end

disp(' Pick minimum plausible group velocity using the left mouse button');

[dummy, vmin] = ginput(1);

kflag = 0;

for k = 1:length(vg)

    if kflag == 0 & vg(k) < vmin

        kflag = 1;

        kmin = k;

    end

end

for i = 1:length(f);

    [amax,imax] = max(B(jmax:kmin,i));

    v(i) = vg(imax+jmax-1);

end
```

```

vggroup(:,n) = v(:);

hold on;

plot(T,v,'w');

plot(T,v,'w','LineWidth',2);

disp('Click on period range that you trust');

[tpick,vdummy] = ginput(2);

for i = 1:length(f);

    if T(i) < tpick(1)

        vgggroup(i,n) = NaN;

    end

    if T(i) > tpick(2);

        vgggroup(i,n) = NaN;

    end

end

end

%%%%%%%%%%%%%%%%%%%%%%%%%%%%%%%%%%%%%%%%%%%%%%%%%%%%%%%%%%%%%%%%%%%%%%%%

```

#### C.4. Forward Modeling

This program forward models to calculate dispersion data for a predefined velocity model.

```

%%%%%%%%%%%%%%%%%%%%%%%%%%%%%%%%%%%%%%%%%%%%%%%%%%%%%%%%%%%%%%%%%%%%%%%%

```

```

% Required input parameters:

```

```

% model.mat – velocity model

```

```

% 'data',per,'path.txt' – File with inter-station paths

%%%%%%%%%%%%%%%%%%%%%%%%%%%%%%%%%%%%%%%%%%%%%%%%%%%%%%%%%%%%%%%%%%%%%%%%

load model.mat

period = [5 : 5 : 40];

len = length(period);

for j = 1:len;

    cd /Volumes/Data/paths

    per = int2str(period(j))

    datafile = strcat('data',per,'path.txt');

    dat = load(datafile);

    cd /Volumes/Data/ANISOTROPY/resolution/forwardmodel

    load velmodel.mat

    [mm,nn] = size(dat);

    file = strcat('data',per,'s.txt');

    gid = fopen(file, 'wt'); % Write data to file

    kk = 0; % Counter

%%%%%%%%%%%%%%%%%%%%%%%%%%%%%%%%%%%%%%%%%%%%%%%%%%%%%%%%%%%%%%%%%%%%%%%%

    dl = 0.01;

    lonl = [min(lon) : dl : max(lon)];

    latl = [min(lat) : dl : max(lat)];

    for i = 1:mm; % Loop through all inter-station paths

```

```
pathlon(i,1) = dat(i,3); % Longitude of station 1
pathlon(i,2) = dat(i,5); % Longitude of station 2
pathlat(i,1) = dat(i,2); % Latitude of station 1
pathlat(i,2) = dat(i,4); % Latitude of station 2
```

```
a = 6371; % radius of the Earth
lat1 = 90 - pathlat(i,1); % colatitude
lat2 = 90 - pathlat(i,2); % colatitude
lon1 = 0 + pathlon(i,1);
lon2 = 0 + pathlon(i,2);
```

```
% convert to rectangular coordinates
```

```
x1 = a*sind(lat1)*cosd(lon1);
y1 = a*sind(lat1)*sind(lon1);
z1 = a*cosd(lat1);
x2 = a*sind(lat2)*cosd(lon2);
y2 = a*sind(lat2)*sind(lon2);
z2 = a*cosd(lat2);
```

```
% end points
```

```
p1 = [x1 y1 z1];
p2 = [x2 y2 z2];
```

```

k = 0;
for t = 0 : dl : 1;
    k = k+1;
    r(k,:) = p1 + t*(p2-p1); %% any point r on the line joining p1 and
p2 vector form.
    g = a./sqrt((r(k,1)^2)+(r(k,2)^2)+(r(k,3)^2)); %% a number g such
that g*r=a.
    pt(k,:) = g * r(k,:); %% points with equal radius, a, along the line

end

x = pt(:,1);
y = pt(:,2);
z = pt(:,3);

% Convert back to spherical coordinates
rho = (x.^2)+(y.^2)+(z.^2);
phi = atand(sqrt((x.^2)+(y.^2))./z);
theta = atan2(y,x);
theta = theta*180/pi; % longitude
phi = 90-phi; % latitude

for j = 1:length(phi)-1;

```

```

        dd(j) = get_delta(phi(j),theta(j),phi(j+1),theta(j+1));
    end

    vpath = griddata(lon,lat,v,theta, phi); % Grid data along path
    az = get_az(phi(length(phi)),theta(length(theta)),phi(1),theta(1));

    vapath = vpath + apath*cosd(2*az) + bpath*sind(2*az);
    vapath = 0.5*(vapath(2:length(vapath))+vapath(1:length(vapath)-1));
    dd = dd*111.3188;
    pathx = cumsum(dd);
    int = trapz(pathx,1./vapath);
    c = max(pathx)/int;

    fprintf(gid, '%d %f %f %f %f %f 1 1 \n', kk, dat(i,2), dat(i,3), dat(i,4), dat(i,5), c);
    kk = kk +1;
    end
    fclose(gid);
end

%%%%%%%%%%

```